THE SEARCH FOR WIMP DARK MATTER CONTINUUM GAMMA-RAY EMISSION FROM DARK MATTER SATELLITES IN THE MILKY WAY USING THE *FERMI* LAT

A DISSERTATION

SUBMITTED TO THE DEPARTMENT OF PHYSICS

AND THE COMMITTEE ON GRADUATE STUDIES

OF STANFORD UNIVERSITY

IN PARTIAL FULFILLMENT OF THE REQUIREMENTS

FOR THE DEGREE OF

DOCTOR OF PHILOSOPHY

Ping Wang

March 2011

This dissertation is online at: http://purl.stanford.edu/tq634bj1551

I certify that I have read this dissertation and that, in my opinion, it is fully adequate in scope and quality as a dissertation for the degree of Doctor of Philosophy.

Elliott Bloom, Primary Adviser

I certify that I have read this dissertation and that, in my opinion, it is fully adequate in scope and quality as a dissertation for the degree of Doctor of Philosophy.

Stefan Funk

I certify that I have read this dissertation and that, in my opinion, it is fully adequate in scope and quality as a dissertation for the degree of Doctor of Philosophy.

Risa Wechsler

Approved for the Stanford University Committee on Graduate Studies.

Patricia J. Gumport, Vice Provost Graduate Education

This signature page was generated electronically upon submission of this dissertation in electronic format. An original signed hard copy of the signature page is on file in University Archives.

ABSTRACT

This thesis focuses on the search for dark matter (DM) satellites in the Milky Way using the *Fermi* Large Area Space Telescope (LAT). The *Fermi* Gamma-ray Space Telescope (*Fermi*) is a next generation space observatory, which was successfully launched on June 11th, 2008. The LAT is the principal scientific instrument onboard. Its unprecedented angular resolution and sensitivity in the 100 MeV to > 300 GeV energy range makes it an excellent instrument for probing the sky for DM satellites. Current N-body simulations based on the ΛCDM cosmology model predict a large number of as yet unobserved DM satellites in our galaxy; some satellites are predicted to be extended sources (> 1^{o} extension) as seen by the LAT. Our work assumes that a significant component of DM is a Weakly Interacting Massive Particle (WIMP) in the 100 GeV mass range. The annihilation of WIMPs results in many high energy γ rays that can be well measured by the LAT. The WIMP produced γ-ray spectrum from the putative DM satellites is considerably harder than most astrophysical sources. Also, DM satellites have no astronomical counterparts in the X-ray and radio bands, and the emission has no time variability. My thesis will focus on a blind analysis in the search for unknown DM satellites using one year of LAT data, and setting constraints on some WIMP models based on the results of our analysis in which we find no candidates.

ACKNOWLEDGMENTS

Looking back, I am surprised and at the same time very grateful for all I have received throughout these years as a PhD student at Stanford University. This dissertation as a product of my research work is certainly high on the list. I owe my gratitude to all the people who have made this dissertation possible and because of whom my graduate experience has been one that I will cherish forever.

My deepest gratitude is to my advisor, Professor Elliott Bloom, for his guidance, patience and, the most important, faith in me. During my graduate career, his caring and support helped me overcome many crisis situations and finish this dissertation.

My research would simply not be without the LAT Collaboration. I would like to thank all the members in Dark Matter and New Physics group in particular. Their extensive knowledge and remarkable insight helped my research in shape. I am also grateful to many persons who shared their advice, expertise and time, especially Seth Digel, Jim Chiang, David Paneque, Markus Ackermann, Simona Murgia, Louie Strigari, Rouven Essig, Neelima Sehgal, Stefan Funk, Anders Borgland.

My thanks also go to all my former and current student-colleagues at KIPAC for the camaraderie and support over my years here. I am particularly thankful to my friends Yvonne Edmonds, Alex Drlica-Wagner, Daniel Chavez Clemente, Josh Lande, Keith Bechtol, Aurelien Bouvier, Herman Lee, Hao-Yi Wu, Bijan Berenji.

Finally, I thank my family for supporting me all these years. My parents have been a constant source of love, concern, support and strength. My husband has always been there cheering me up and standing by me through the good times and bad. My son is the sunshine of my life and learning to be a mom makes me a better person.

DEDICATION

To
my parents Fuguo Wang and Qingju Zeng
for their endless love and encouragement

and to
my husband Xie Fang
for his understanding and support

and to
my son Ian Fang
for his sunshine smile always

TABLE OF CONTENTS

LIST OF TABLES

LIST OF FIGURES

INTRODUCTION

The *Fermi* Gamma-ray Space Telescope (*Fermi*), formerly the Gamma-ray Large Area Space Telescope (GLAST), was launched by NASA from Cape Canaveral on June 11th, 2008. The Large Area Telescope (LAT), the principal scientific instrument onboard, is an imaging high-energy γ-ray telescope covering the energy range from about 20 MeV to more than 300 GeV. The LAT's field of view (FoV) covers about 20% of the sky at any time, and it scans continuously, covering the whole sky every three hours. With an expected five to ten years time of operation, the mission aims at a deeper understanding of astrophysical objects producing high-energy γ-rays such as active galactic nucleus (AGNs), pulsars, supernova remnants (SNRs) and gamma-ray bursts (GRBs), and searches for signals of dark matter (DM) and new physics.

This thesis focuses on the search for dark matter from the substructures (satellites) in the Milky Way using one year of LAT data. This search is on the assumption that a significant component of DM is Weakly Interacting Massive Particles (WIMPs) in the 100 GeV mass range. The annihilation of WIMPs results in many high-energy γ-rays that can be well measured by the LAT.

The first chapter presents an introduction to dark matter and dark matter satellites, including the particle candidates for DM, the γ-ray yields from WIMP annihilation, the spatial density profile for DM and the properties of the DM satellites in the Via Lactea II (VL2) simulation [15].

Chapter 2 briefly reviews the major components of the *Fermi* LAT and the pre-launch and the post-launch response and performance of the LAT.

In Chapter 3, we estimate the LAT sensitivity to the DM satellites in the VL2 simulation based on the LAT performance for one year of observation for five interesting WIMP models.

Chapter 4 summarizes Chernoff's theorem [66] that can be used to determine which hypothesis is preferred based on the test statistic (TS) of two hypotheses. The TS is defined as -2 times the natural logarithm of the likelihood ratio. In this chapter, we also show the limitation of Chernoff's theorem in our cases of source extension test and source detection test using Monte Carlo simulation.

A detailed description of the analysis method for the search for DM satellites is given in Chapter 5. Since Chernoff's theorem does not apply to our cases, we developed a method, called embedded Monte Carlo simulation, to find the TS distribution of two hypotheses, and based on the derived TS distribution we could select a preferred hypothesis. In this chapter, we also present the analysis result that no DM satellite candidates are found using one year of LAT data and discuss the possible contamination for our search – unidentified high-latitude pulsars.

Finally, Chapter 6 calculates the efficiency of our analysis method and then the predicted numbers of observed VL2 satellites for the five WIMP models by using our analysis method. Comparing with the search result that no DM satellites are found, we set constraints on the five WIMP models and also derive the 95% upper limit of the annihilation cross section for a 100 GeV WIMP annihilating into the $b\bar{b}$ channel.

CHAPTER 1
DARK MATTER

1.1 History and Evidence of Dark Matter (DM)

In the 1930s, Swiss astrophysicist Fritz Zwicky [1][2] measured the relative velocities of the galaxies in the Coma cluster of galaxies and used the virial theorem to infer the mass of this cluster. He found that the mass-to-light ratio (in solar units) for galaxies in the Coma cluster was 500, which was much higher than that for stars in the local solar neighborhood. One of the possible explanations he proposed was the Coma cluster contained lots of non-visible extra mass – dark matter (DM). This is known as the "missing mass problem". Zwicky is the first person to speculate the existence of DM.

In the 1970s, Vera Rubin and Kent Ford [3] measured the rotation curve of the Andromeda Galaxy (M31). If the mass of the galaxy was concentrated in the region where the stars were visible, from Kepler's law the rotation velocities should fall off as $r^{-1/2}$ outside this region. However, Rubin and Ford discovered that the rotation velocities of sixty-seven HII regions remained approximately constant over a distance of 24 *kpc* from the galaxy center, even though the visible stars became rare outside 3 *kpc*. This implied that the mass of M31 increased with galactocentric distance well beyond the stellar radius. The derived mass-to-light ratio for M31 within 24 *kpc* was 13. From then on, many other astronomers began to systematically measure the rotation curves for many galaxies and it soon became well-established that most galaxies were in fact dominated by DM. The typical mass-to-light ratio was 1 – 12 for spiral galaxies and 5 – 20 for elliptical galaxies [53].

From the 1980s, astrophysicists became interested in dwarf spheroidal galaxies (dSphs). dSphs are low luminosity and low surface brightness galaxies with a lack of gas or dust or recent star formation in the Local Group. The first two dSph, the Large Magellanic Cloud (LMC) and Small Magellanic Cloud (SMC), was discovered about 600 years ago. Until 2005, there were 11 classical dSphs recognized as the Milky Way's satellite galaxies: LMC (1519), SMC (1519), Sculptor (1937), Fornax (1938), Leo II (1950), Leo I (1950), Ursa Minor (1954), Draco (1954), Carina (1977), Sextons (1990), Sagittarius (1994). After 2005, 14 more ultra-faint dSphs were discovered by the Sloan Digital Sky Survey (SDSS): Ursa Major I (2005), Willman 1 (2005), Ursa Major II (2006), Bootes I (2006), Canes Venatici I (2006), Canes Venatici II (2006), Coma Berencies (2006), Segue 1 (2006), Leo IV (2006), Hercules (2006), Leo T (2007), Bootes II (2007), Leo V (2008), Segue 2 (2009). In general, the mass-to-light ratios of those dSphs were found very high, > 100, indicating that DM made up large fractions of their masses [4, 5].

In 2006, studies of the Bullet cluster (1E 0657-56), a unique cluster merger, provided the best direct and unequivocal evidence to date for the existence of DM [6]. The gravitational lensing maps of the Bullet cluster showed the separation of the center of the total mass from the center of the baryonic mass and thus proved that the majority of the matter in the cluster was DM, as shown in Figure 1.1. There have been observations of other colliding galaxy clusters since the Bullet cluster that reinforce the Bullet results. [43 – 45]

In the 2000s, the Wilkinson Microwave Anisotropy Probe (WMAP) provided the most detailed measurements of anisotropies in the Cosmic Microwave Background (CMB) [7, 8, 9]. WMAP's measurements confirmed the standard flat Λ Cold Dark Matter (ΛCDM) model, with 4.6% baryonic matter, 23% CDM and 72% dark energy in the universe.

Figure 1.1 A composite image of the Bullet cluster. The cluster's individual galaxies are seen in the optical image data. The cluster's two clouds of hot x-ray emitting gas are shown in red. The blue hues show the total matter in the cluster by observations of gravitational lensing of background galaxies. The clear separation of total matter and gas clouds is considered direct evidence of the existence of DM. (Sources: HubbleSite, Chandra)

1.2 Particle Candidates of DM

As the ΛCDM cosmology model has been well established, our main interest is to look for CDM candidates. The most popular non-baryonic CDM candidates are axions and weakly interacting massive particles (WIMPs). In this thesis, we focus on the WIMP DM.

1.2.1 Axions

Axion is a hypothetical elementary particle postulated by the Peccei-Quinn theory [18] in 1977 to resolve the strong CP problem in quantum chromodynamics (QCD). This original axion was completely excluded by the Crystal Ball experiment [46]. This led quickly to the postulation of the "invisible axion" by [47]. Since that time, laboratory searches, stellar cooling and the dynamics of supernova 1987A constrain

axions to be very light ($\lesssim 0.01$ eV). Furthermore, they are expected to be extremely weakly interacting with ordinary particles, which implies that they were not in thermal equilibrium in the early universe.

The calculation of the axion relic density is uncertain, and depends on the assumptions made regarding the production mechanism. Nevertheless, it is possible to find an acceptable range where axions satisfy all present-day constraints and represent a possible DM candidate [19].

Axions are predicted to couple with photons in the presence of magnetic fields. The axions populated in the Milky Way halo can potentially be detected via resonant conversion to photons in a magnetic field. The Axion Dark Matter Experiment (ADMX) is an ongoing experimental search for axions in our halo [20] and it has excluded optimistic axion models in the 1.9 μeV to 3.53 μeV range [21]. In addition, the axions existed in the intergalactic medium and active galactic nucleus (AGNs) may lead to a significant change in the observed spectra of AGNs. This signature may be observationally detectable with current γ-ray instruments such as *Fermi* LAT and IACTs [22].

1.2.2 WIMPs

WIMP is a hypothetical neutral heavy elementary particle that is stable for the lifetime of the universe. Predictions of the WIMP mass are typically in the GeV to TeV range. WIMPs have interactions with ordinary matter through the weak force and gravity.

1.2.2.1 Relic Density

- **Thermal WIMPs**

Although it is stable, the WIMP can be produced in pairs (perhaps with its antiparticle), and it could be produced thermally at an early time when the temperature of the universe was very high. WIMPs also annihilate in pairs. These processes establish a thermal equilibrium in the early universe, when the temperature of the universe T exceeds the WIMP mass M_χ. As the universe expands and cools to a temperature below M_χ, the equilibrium abundance drops exponentially $\propto \exp\left(-\frac{M_\chi}{T}\right)$, until the annihilation rate falls below the expansion rate, at which point the interactions maintain thermal equilibrium and the relic cosmological density freezes out. The relic density of WIMPs is derived by detailed evolution of the Boltzmann equation [23], and an order-of-magnitude estimate [24] is:

$$\Omega_\chi h^2 \approx \frac{3\times10^{-27} cm^3 s^{-1}}{<\sigma v>} \tag{1.1}$$

where h is the Hubble constant in units of $100km\ s^{-1}Mpc^{-1}$, and $<\sigma v>$ is the thermally averaged velocity times cross section for two WIMPs to annihilate into ordinary particles. This result is independent of the WIMP mass. The remarkable fact is that for the electroweak scale interactions, it can give the WMAP required relic density $\Omega_\chi h^2 \sim 0.1$ without much fine tuning. This sometimes termed the "thermal WIMP miracle". WIMPs now move non-relativistically with typical velocities $v/c \sim 10^{-3}$ which have redshifted considerably since the time of thermal decoupling.

- **Non-thermal WIMPs**

WIMPs can be created non-thermally in the early universe. For example, in string theories with moduli stabilization, prior to Big Bang Nucleosynthesis (BBN), decays

of moduli can be a significant source of DM production. There exists a "non-thermal WIMP miracle" under very general conditions [41, 42]. The relic density is

$$\Omega_\chi h^2 \approx 0.1 \times \left(\frac{M_\chi}{100\ GeV}\right)\left(\frac{10.75}{g_*}\right)^{\frac{1}{4}}\left(\frac{\sigma_0}{<\sigma v>}\right)\left(\frac{100\ TeV}{m_\phi}\right)^{3/2} \quad (1.2)$$

where M_χ is the WIMP mass, m_ϕ is the moduli mass, $\sigma_0 = 3 \times 10^{-24} cm^3 s^{-1}$, g_* is the effective number of the massless degrees of freedom. This non-thermal DM setup suggests larger annihilation cross-sections than the thermal WIMP case considering the correct relic density, and this is primarily due to these models addressing the ATIC, PAMELA and *Fermi* e^+e^- results [48 – 50].

1.2.2.2 WIMP Models

There are many different WIMP candidates proposed by different theories. A comprehensive review of DM models has been given by Bertone, Hooper and Silk [30]. Here we only briefly list some popular models and candidates.

- **Supersymmetry (SUSY)**

In the Standard Model of particle physics there is a fundamental distinction between bosons and fermions: while bosons are the mediators of interactions, fermions are the constituents of matter. Supersymmetry is a hypothetical theory which relates bosons and fermions, thus providing a sort of "unified" picture of matter and interactions. In supersymmetric models, every standard particle has a super partner called a sparticle.

We consider the Minimal Supersymmetric extension of the Standard Model (MSSM). The conservation of R-parity makes the Lightest Supersymmetric Particle (LSP) an excellent WIMP candidate, because it is stable and can only be destroyed via pair annihilation. MSSM contains a huge number of free parameters. Different choices

of parameters, referred to as scenarios, will give different LSP or different WIMP candidates. For these Majorana fermion WIMP candidates in the supersymmetric models, the S-wave annihilation rate into the light fermion species is suppressed by the factor m_f^2/M_χ^2, where m_f is the mass of the fermion in the final state.

- ***Neutralinos***

The super partners of the *B*, W_3 gauge bosons (or the photon and *Z*, equivalently) and the neutral Higgs bosons, $H_1{}^0$ and $H_2{}^0$, are called binos ($\tilde{B}$), winos ($\widetilde{W_3}$), and higgsinos ($\widetilde{H_1^0}$ and $\widetilde{H_2^0}$), respectively. These states mix into four Majorana fermionic mass eigenstates, called neutralinos. The lightest of the four neutralinos is the LSP. Neutralinos are by far the most widely studied WIMP DM candidates.

- ***Gravitinos***

Gravitinos are the super partners of the graviton. In some SUSY scenarios, gauge mediated supersymmetry for example, gravitinos can be the LSP. As gravitions only interact gravitationally, the annihilation cross section of gravitinos is much smaller than given in Eq (1.1) [51]. However, in some models gravitinos decay, and this would give a visible signature for indirect detection searches [52, 53]. It is currently not possible to produce gravitinos in accelerator experiments or detect them via direct detection experiments due to the very small interaction cross section of gravitinos interacting with regular matter or their super partners.

- ***Universal Extra Dimensions (UED)***

In many extra-dimensional models, the (3+1)-dimensional space time we experience is a structure called a brane, which is embedded in a (3+δ+1) space time

called the bulk. A general feature of extra-dimensional theories is that upon compactification of the extra dimensions, all of the fields propagating in the bulk have their momentum quantized in units of $p^2 \sim 1/R^2$, where R is the size of the extra dimensions. The result is that for each bulk field, a set of Fourier expanded modes, called Kaluza-Klein (KK) states, appears. From our point of view in the four-dimensional world, these KK states appear as a series (called a tower) of states with masses $m_n = n/R$, where n labels the mode number. Each of these new states contains the same quantum numbers, such as charge, color, etc.

In the UED scenario, the KK-parity makes the Lightest Kaluza-Klein Particle (LKP) an excellent WIMP candidate. The LKP is likely to be associated with the first KK excitation of the photon, or more precisely the first KK excitation of the hypercharge gauge boson [31], referred to as B_1. A calculation of the B_1 relic density [32] shows that if the LKP is to account for the observed quantity of DM, its mass should lie in the range of 400 – 1200 GeV. Unlike in the case of supersymmetry, the bosonic nature of the LKP means that there will be no chirality suppression in its annihilations, and thus can annihilate efficiently to fermion-antifermion pairs. In particular, since the annihilation cross section is proportional to hypercharge of the final state, a large fraction of LKP annihilations produce charged lepton pairs.

- ***Little Higgs Models***

As an alternative mechanism (to supersymmetry) to stabilize the weak scale, the so-called "little Higgs" models have been proposed and developed [33 – 36]. At least two varieties of little Higgs models have been shown to contain possible DM candidates. One of these classes of models, called "theory space" little Higgs models, provide a possibly stable, scalar particle which can provide the measured density of dark matter [37]. Another variety of little Higgs model, introducing T-parity, result in a stable WIMP candidate with ~ TeV mass – the lightest T-odd particle (LTP) [38].

1.3 γ-ray Yield from WIMP Annihilation

WIMPs can annihilate into pairs of quarks, leptons, Higgs and weak gauge bosons, while they can also directly annihilate into γ-rays. Those annihilations yield two different γ-ray spectral components: continuum and spectral lines. These γ-rays can be detected by the *Fermi* Gamma-ray Space Telescope (*Fermi*) Large Area Space Telescope (LAT). This thesis focuses on the continuum γ-rays.

1.3.1 Continuum γ-rays

At tree level, among the kinematically allowed final states, the leading channels are often $b\bar{b}$, $t\bar{t}$, W^+W^-, Z^0Z^0, $\tau^+\tau^-$ [24, 25]. This is the case for neutralinos and, more generically, for any Majorana fermion WIMP, since the annihilation rate into the light fermion species is suppressed. The fragmentation and /or the decay of the tree-level annihilation states give rise to secondary photons. The dominant intermediate step is the generation of neutral pions and their decay into 2γ, as Figure 1.2 shows. The simulation of the γ-ray yield is standard and can be performed with the Lund Monte Carlo program `Pythia`. Figure 1.3 shows the differential γ-ray yield per annihilation for a few channels and a fixed WIMP mass 200 GeV. The spectra have a rather soft cutoff at the WIMP mass, almost indistinguishable for the various possible annihilation channels except τ-lepton final state.

At first order electromagnetic radiative corrections to the tree-level diagrams, another contribution has to be included whenever WIMPs annihilate into a pair of charged particle final states, internal bremsstrahlung (IB) [26, 27]. This is particularly the case for the KK particle, since a large fraction of annihilations in this case produce charged lepton pairs (eg. e^+e^-, $\mu^+\mu^-$). Figure 1.4 shows three types of diagrams of IB. The leading contributions to diagrams (a) and (b) are universal, referred to as final state radiation (FSR), with photons directly radiated from the external legs. IB from

virtual particles (or virtual internal bremsstrahlung, VIB) is as in diagram (c). VIB is strongly dependent on details of the short-distance physics such as helicity properties of the initial state and masses of intermediate particles. However, as pointed out in [26], the γ-ray yield from the FSR is quite robust which only depends slightly on the final state particle spin, approximating to a power-law with the spectral index -1 with a sharp cutoff at the WIMP mass, as shown in Figure 1.5.

In this thesis, we will only discuss the γ-ray spectra from secondary photons and from FSR, because those γ-ray yields are almost independent of the new particle physics. Thus, we develop a general and universal method to search for those spectral features.

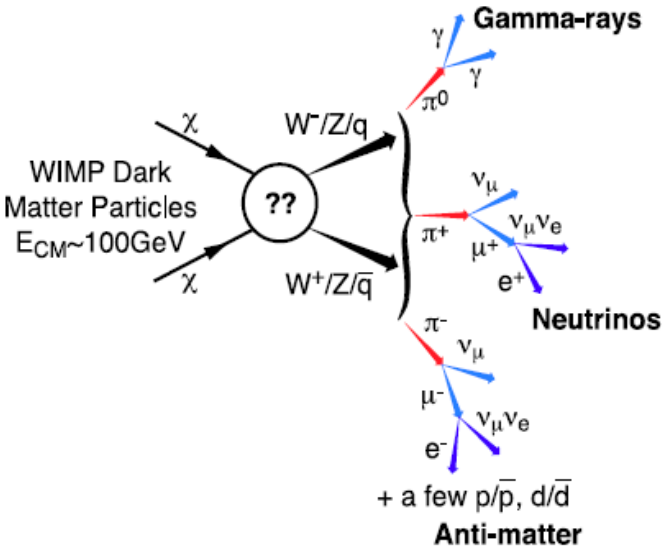

Figure 1.2 A diagram of how secondary photons are produced by WIMP annihilation at tree level. The double question mark indicates high uncertainty in the models of the new particle theories. (from [24])

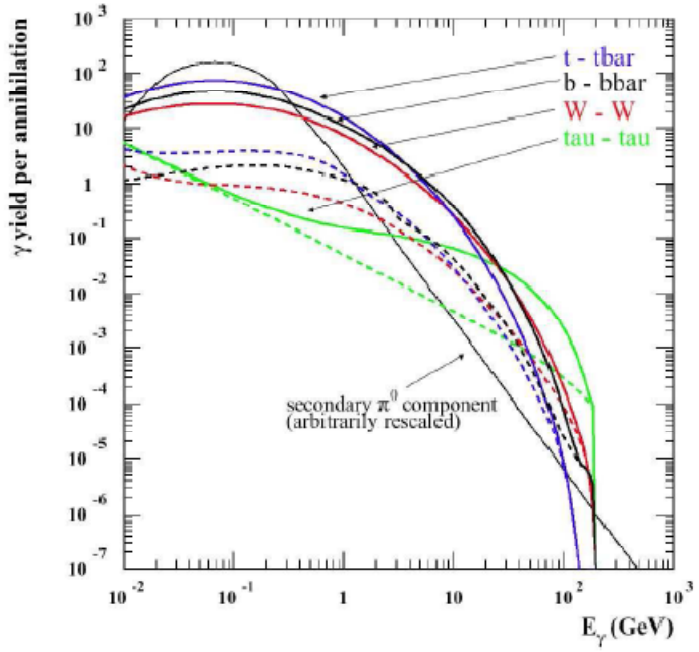

Figure 1.3 Differential γ-ray yield per annihilation for a few sample annihilation channels and a fixed WIMP mass 200 GeV. The solid lines are the total yields, while the dashed lines are components not due to π^0 decays. For comparison we also show the cosmic ray induced gas emissivity, with an arbitrarily rescaled normalization, from the interaction of primaries with the interstellar medium. This photon spectrum from cosmic ray secondary π^0 has a very different spectral shape than the WIMP annihilation spectra. (from [25])

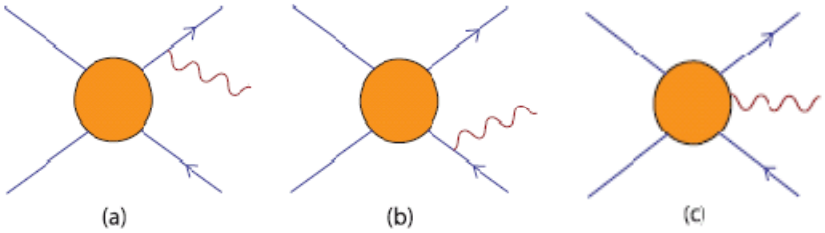

Figure 1.4 Types of diagrams that contribute to the first order corrections to WIMP annihilations into a pair of charged particle final states. Diagrams (a) and (b) are referred to as final state radiation (FSR), and diagram (c) is internal bremsstrahlung from virtual particles (or virtual internal bremsstrahlung, VIB). (from [27])

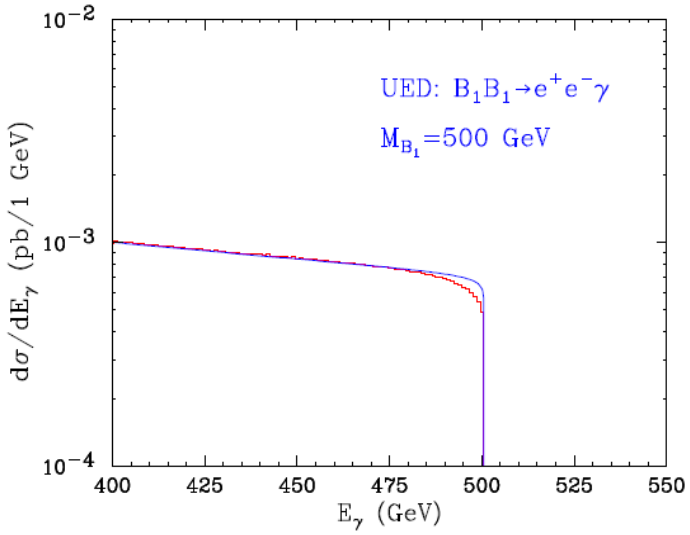

Figure 1.5 Comparison of the photon spectrum obtained by a direct calculation in the UED model with the radius of the extra dimension $R = (499.07GeV)^{-1}$ using the CompHEP package (red histogram) and the spectrum predicted by QED (blue line) for the case of $B_1B_1 \to e^+e^-\gamma$ annihilation at $\sqrt{s} = 1001GeV$. The mass of the lightest KK particle (the first excited mode B_1 of the hypercharge gauge boson) is 500 GeV. (from [26])

1.3.2 γ-ray Lines

At loop level, WIMPs can directly annihilate into photons through different channels, eg. $\gamma\gamma$, γZ^0 and γH^0, as shown in Figure 1.6, which results in monochromatic γ-ray lines. WIMPs annihilating into γX produce monochromatic γ-rays of energy $E_\gamma = M_\chi(1 - \frac{m_X^2}{4M_\chi^2})$, where m_X is the mass of X. The search for the γ-ray lines has been done using the EGRET data in the energy range 1 – 10 GeV [28] and using the *Fermi* LAT data in the energy range 20 – 300 GeV [29]. As pointed out in [29], there is no significant line detection using the 11-month LAT data sample.

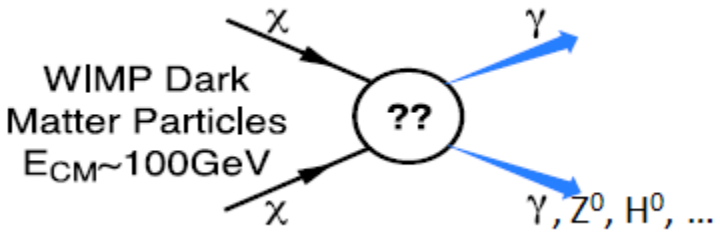

Figure 1.6 A diagram of how spectral lines are produced by WIMP annihilation at loop level. The double question mark indicates high uncertainty in the models of the new particle theories. (from [24])

1.4 Spatial Distribution of DM

Over the past two decades, cosmological N-body simulations of structure formation on the basis of the CDM scenarios have been used to model the astrophysical distribution of DM to increasingly small scales [10 – 16]. The simulations show that DM is extremely dense in the center of the halo and decreasingly dense for increasing halo radius over a large distance. In the CDM paradigm, structure forms hierarchically, so the DM halo is not smooth but contains large numbers of bound substructures (satellites).

The simulations indicate the existence of a universal DM density profile over a large range of masses [10]. The usual parameterization for a DM halo density is

$$\rho(r) = \frac{\rho_s}{(\frac{r}{r_s})^{\gamma}(1+(\frac{r}{r_s})^{\alpha})^{(\beta-\gamma)/\alpha}} \tag{1.3}$$

This function behaves approximately as a broken power-law that scales as $r^{-\gamma}$ close to the center of the halo, $r^{-(\beta-\gamma)/\alpha}$ at intermediate distance r_s, and $r^{-\beta}$ in the outskirts of the halo. Various groups have ended up with different results for the density profile. Three of the most widely used profile models are the NFW profile [10] with $(\alpha, \beta, \gamma) = (1, 3, 1)$, the Moore profile [11] with $(\alpha, \beta, \gamma) = (1.5, 3, 1.5)$, and the isothermal profile [39] with $(\alpha, \beta, \gamma) = (2, 2, 0)$. ρ_s and r_s are determined by the detailed properties of the individual halo or satellite.

One of the highest-resolution N-body simulations, Via Lactea II (VL2) [15], has simulated the DM halo of a Milky Way sized galaxy in a ΛCDM universe with cosmological parameters taken from WMAP [8]. VL2 was able to resolve satellites down to masses as small as $\sim 10^5\ M_\odot$. This simulation reported a remarkable self-similar pattern of clustering properties: the inner profiles of the main halo and satellites were consistent with $\gamma \cong 1.2$, a steeper density profile in the inner part of the profile than the NFW profile.

Another high-resolution N-body simulation, Aquarius Project [16], also simulated a Milky Way sized DM halo in a ΛCDM universe with cosmological parameters consistent, within the errors, with those that best fit the WMAP 1-year and 5-year data analysis. Its resolution of satellite mass was $\sim 10^{4.5}\ M_\odot$. The inner regions of the main halo and satellites could be well fitted by the Einasto profile which was a shallower density profile in the center than the NFW profile:

$$\rho(r) = \rho_s \exp\left(-\frac{2}{\alpha}\left(\left(\frac{r}{r_s}\right)^{\alpha} - 1\right)\right) \tag{1.4}$$

where $\alpha \sim 0.17$.

Figure 1.7 [52] shows the shape of DM density for the Milky Way by assuming a Moore profile, an NFW profile, an Einasto profile and an isothermal profile respectively, as a function of the galactocentric radius. In all cases, the density is normalized to $\rho(r_\odot) = 0.3\ GeV/cm^3$.

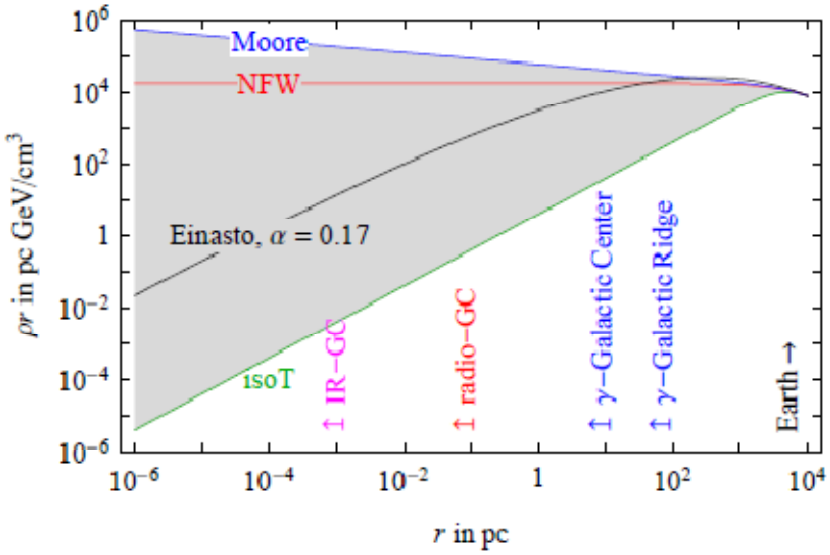

Figure 1.7 Shape of DM density for the Milky Way by assuming a Moore profile, an NFW profile, an Einasto profile and an isothermal profile respectively, as a function of the galactocentric radius, r. In all cases, the density is normalized to $\rho(r_\odot) = 0.3\ GeV/cm^3$. (from [52])

1.5 DM Satellites in the Milky Way

1.5.1 Missing Satellites Problem

The N-body simulations of Milky Way sized DM halos based on the ΛCDM model predict a satellite count that greatly outnumbers the currently observed satellites of the Milky Way. This is known as the "missing satellites problem" [4, 17]. Since 2005, SDSS has discovered 14 more ultra-faint dSphs. Considering that SDSS only covers 25% of the sky, the estimate number of dSphs in the whole sky within the SDSS observation depth is 56. One possible reason for the deficiency of observed satellites in the Milky Way is there are too few stars associated with the unobserved DM satellites to be observed using optical telescopes. Another possible reason is that some satellites have not had sufficiently large mass during a period of their evolution to allow them to overcome the star formation suppression processes so they have no

stars at all. There are many other possible reasons, e.g., the ΛCDM model is incorrect on the small scales probed by the satellites. A comprehensive discussion on this problem can be found in [92].

1.5.2 Low-mass Satellites

Depending on the parameters of the DM particle physics model, a wide variety of kinetic-decoupling temperatures is possible, ranging from several MeV to a few GeV. These decoupling temperatures imply a range of masses for the smallest DM satellites ranging from 10^{-4} $M_\odot$ to 10^{-12} $M_\odot$ [40]. On the other hand, the satellite mass functions of different N-body simulations show that our local region is dominated in number by the low-mass satellites. Therefore, these low-mass satellites are very promising targets for indirect detection of DM annihilation because they are numerous, relatively nearby, and devoid of astrophysical background. However, the luminosity of a given satellite is also strongly dependent on its mass and concentration. Thus, it is unclear whether these low-mass satellites will be a substantial source of γ-rays. The resolution limit of current N-body simulations makes it a long term problem to investigate this question.

Before the VL2 and Aquarius simulations, the satellite mass resolutions of N-body simulations were $\sim 5 \times 10^7\ M_\odot$. Taylor and Babul [12 – 14] developed a semi-analytic method based on merger trees to study satellites with masses as small as $\sim 2.5 \times 10^6\ M_\odot$.

Another way to study the low-mass satellites below the mass resolution of N-body simulations is to extrapolate the mass function from the population of higher-mass satellites. This analytic method is not limited by computer cost, so it can go to as low mass as we want. For this thesis, we extrapolate the satellite mass function of VL2 down to 1 $M_\odot$. The details how we did the extrapolation are shown in Appendix A.

In this thesis, we choose the VL2 simulation as a representative of the Milky Way DM halo. It is one of the highest-resolution simulations to date. However, it still has many limitations. It assumes the ΛCDM cosmology model that is consistent with the WMAP observation, and all of the matter in the universe is modeled as dark matter (without ordinary baryons). Its resolution limits the complicated galaxy formation processes on small scales. It only simulates one halo, which might not be a typical Milky Way sized halo due to statistical fluctuation. The Aquarius Project which simulated six halos shows no large differences between halos.

1.5.3 14 Realizations of the VL2 DM Satellites

In this thesis, we create 14 realizations of the VL2 satellites corresponding to 14 viewpoints on the 8.5 *kpc* solar sphere with the 14 viewpoints maximally separated. The Earth position in each realization is listed in Table 1.1.

Since the 14 realizations are not independent simulations, the same satellites may appear in more than one realization. By pre-cutting on the mass and distance of satellites as described in §A.3, there are 9758 satellites in total for the 14 realizations (697 satellites per realization on average) among which 6690 satellites are with $|b| > 20^o$ (478 high-latitude satellites per realization on average). The J value is defined as the integral along the line of sight (l.o.s) of the assumed density squared, $\rho(l)^2$, of DM, which is proportional to the γ-ray flux emitted from DM annihilation:

$$J = \int d\Omega \int_{l.o.s} \rho(l)^2 dl \tag{1.5}$$

Here we calculate J values by assuming the NFW profile for DM satellites. Figure 1.8 shows the distribution of J value as a function of the satellite mass and the distance from the Earth for the 6690 satellites with $|b| > 20^o$. From Figure 1.8, the dominant contributors to large J values are the original VL2 satellites.

Some DM satellites are obviously not point sources. The discussion about the satellite extension is in §5.3.1.

Table 1.1 Earth locations on the solar sphere relative to the galactic center for the 14 realizations of the VL2 simulation. Use the (x, y, z) coordinate system defined in the VL2 data file.

Realization	Azimuth angle of the Earth (^{o})	Zenith angle of the Earth (^{o})
0	0	90
1	270	90
2	135	45
3	225	135
4	45	45
5	315	45
6	180	90
7	0	180
8	45	135
9	135	135
10	0	0
11	225	45
12	315	135
13	90	90

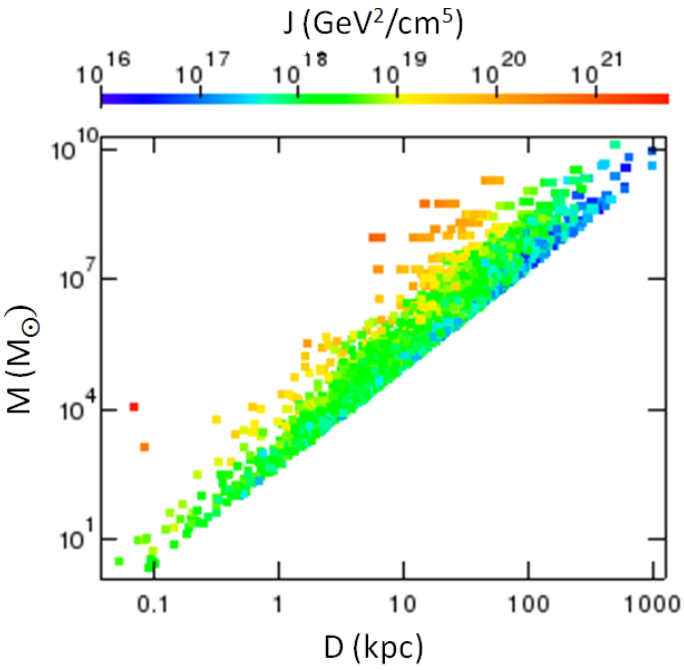

Figure 1.8 Distribution of J value as a function of the satellite mass (in solar mass) and the distance to the Earth for the 6690 satellites with $|b| > 20^o$ for the 14 realizations (478 high-latitude satellites per realization on average).

CHAPTER 2
THE *FERMI* LARGE AREA TELESCOPE

The *Fermi* Gamma-ray Space Telescope (*Fermi*), formerly the Gamma-ray Large Area Space Telescope (GLAST), is a next generation space observatory, which was successfully launched on June 11th, 2008, and has been operating in nominal configuration for scientific data taking since early August 2008. Its main instrument, the Large Area Telescope (LAT), is designed to explore the high-energy γ-ray sky in the 20 MeV to > 300 GeV energy range, with unprecedented angular resolution and sensitivity.

2.1 LAT Structure

The LAT is a pair-production telescope [54] with a precision tracker (TKR) and calorimeter (CAL), each consisting of a 4 × 4 array of 16 modules, a segmented anticoincidence detector (ACD) that covers the tracker array, and a programmable trigger and data acquisition system. The schematic diagram of the LAT is shown in Figure 2.1.

Each TKR module has 18 (x, y) tracking planes, consisting of two layers (x and y) of single-sided silicon strip detectors. The 16 planes at the top of the tracker are interleaved with high-Z converter material – tungsten. The top 12 planes, at the *Front* of the instrument, each have a thin foil with 0.03 radiation length. The following 4 planes, in the *Back* section, each have a thick foil with 0.18 radiation length. The bottom two planes have no converter and are used to follow charged particles into the calorimeter with minimal multiple scattering. The TKR is responsible for the

conversion of the incident photon into an electron-positron pair and for the tracking of the latter charged particles. Front and back sections have intrinsically different performance due to greatly increased multiple scattering in the back.

There are 16 CAL modules, each associated with a TKR module and readout electronics into a TKR-CAL tower. Every CAL module has 96 CsI (Tl) crystals, arranged in an eight-layer hodoscopic configuration with a total depth of 8.6 radiation lengths. The calorimeter's depth and segmentation enable the measurement of the energy deposition due to the electromagnetic particle shower that results from the e^+e^- pair produced by the incident photon and image the shower development profile thereby providing an important background discriminator and an estimator of the shower energy leakage fluctuations.

The ACD, made of 89 plastic scintillation tiles and 8 scintillation ribbons, provides charged-particle background rejection of at least 0.9997 efficiency (averaged over the ACD area). Secondary particles (mostly 100 – 1000 *keV* photons) from the electromagnetic shower in the CAL created by incident high-energy photons can Compton scatter in the ACD and thereby create false veto signals from the recoil electrons, the so-called backsplash effect. The ACD is segmented to suppress the backsplash effect. The 8 scintillation ribbons are used to cover the gaps between the ACD tiles so as to achieve the required efficiency of 0.9997.

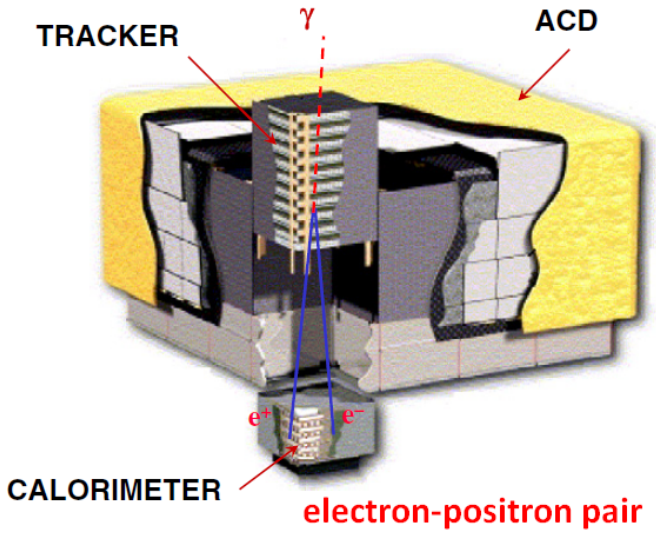

Figure 2.1 Schematic diagram of the LAT. The LAT contains 16 identical tracker and calorimeter towers, covered with a segmented anticoincidence detector. Incident photons are converted to e^+e^- pairs in the tracker. The produced charged particles are tracked in the tracker and their energy is measured in the calorimeter. (from [54])

2.2 LAT Response and Performance

The LAT response or γ-rays is expressed by means of instrument response functions (IRFs). Canonically the detector response is factored into three terms: the detector effective area, and resolutions as angular point spread function (PSF) and energy dispersion. Components of the IRFs are usually a tabular representation of the corresponding figures of merit in terms of the photon true energy and direction in the detector system of reference.

To evaluate the LAT response a dedicated Monte Carlo simulation is performed. A huge amount of γ events is simulated, in order to cover with good statistics all possible photon inclinations and energies over the nominal acceptance of the LAT. All detector volumes and all physics interactions must be simulated, so this is actually a considerable effort in terms of computer time. Pre-launch performance estimates and related IRFs, called "P6_V1", are documented in [54]. Table 2.1 summarizes the pre-

launch performance capabilities of the LAT. Table 2.2 lists three analysis classes that have been defined based on the backgrounds expected in orbit and the pre-launch performance of the LAT. The classes are differentiated by increasingly tighter requirements on the charged-particle background rejection efficiency.

However, after launch, some unexpected interactions between background and γ events, so-called *ghost events*, were observed in real data, which were not simulated in Monte Carlo simulation as this effect was not anticipated. As an example, let us consider a background event releasing energy in the detector and no trigger request is issued from this event. A ghost may occur if a photon strikes the LAT while the energy released by the background particle is still being collected: if a γ event triggers the data acquisition and LAT channels are latched and read, digitized signals caused by both the photon and the background deposition are collected and transmitted to Earth. Therefore, we have to include the inefficiencies caused by the ghost hits to the IRFs. The performance degradation is accounted for in the post-launch IRFs. Post-launch performance and related IRFs, called "P6_V3", now available publicly, are documented on the NASA *Fermi* website [55]. Additional details are in [56]. In Figure 2.2 – 2.4, we plot a direct comparison of normal-incidence effective area, 68% and 95% PSF at normal incidence in the thin (front) section of the TKR, 68% energy resolution at normal incidence for the DIFFUSE class: the solid curve is P6_V3, the dashed one is P6_V1. The P6_V3_DIFFUSE PSF shown in Figure 2.3 is the MC PSF of P6_V3. The on-orbit PSF is actually not this good at high energy, > 10 GeV, as determined from on-orbit measurement of point sources. The on-orbit PSF has only recently become available in final form. The analysis in this thesis is based on the MC PSF. We expect little change for the results of this analysis if the on-orbit PSF would be used. Figure 2.5 – 2.7 shows the effective area, 68% and 95% PSF and energy resolution for the P6_V3_DIFFUSE class.

We did some independent cross-checks of the LAT calibration on the ground, including selecting photons from ground cosmic ray data (Appendix F) and cross-checking the CAL calibration (Appendix G).

Table 2.1 Summary of LAT instrument parameters and estimated pre-launch performance (from [54]).

Parameter	Value or Range
Energy range	20 MeV–300 GeV
Effective area at normal incidence[a]	9,500 cm^2
Energy resolution (equivalent Gaussian 1σ):	
100 MeV–1 GeV (on-axis)	9%–15%
1 GeV–10 GeV (on-axis)	8%–9%
10 GeV–300 GeV (on-axis)	8.5%–18%
>10 GeV (>60° incidence)	⩽6%
Single photon angular resolution (space angle)	
on-axis, 68% containment radius:	
>10 GeV	⩽0.°15
1 GeV	0.°6
100 MeV	3.°5
on-axis, 95% containment radius	$< 3 \times \theta_{68\%}$
off-axis containment radius at 55°	< 1.7× on-axis value
Field of View (FoV)	2.4 sr
Timing accuracy	< 10 μs
Event readout time (dead time)	26.5 μs
GRB location accuracy onboard[b]	< 10′
GRB notification time to spacecraft[c]	<5 sec
Point source location determination[d]	< 0.′5
Point source sensitivity (>100 MeV)[e]	3×10^{-9} ph cm^{-2} s^{-1}

Notes.

[a] Maximum (as a function of energy) effective area at normal incidence. Includes inefficiencies necessary to achieve required background rejection. Effective area peak is typically in the 1 to 10 GeV range.

[b] For burst (<20 s duration) with >100 photons above 1 GeV. This corresponds to a burst of ~5 cm^{-2} s^{-1} peak rate in the 50 – 300 keV band assuming a spectrum of broken power law at 200 keV from photon index of –0.9 to –2.0. Such bursts are estimated to occur in the LAT FoV ~10 times per year.

[c] Time relative to detection of GRB.

[d] High latitude source of 10^{-7} cm^{-2} s^{-1} flux at >100 MeV with a photon spectral index of –2.0 above a flat background and assuming no spectral cutoff at high energy; 1σ radius; one-year survey.

[e] For a steady source after one-year sky survey, assuming a high-latitude diffuse flux of 1.5×10^{-5} cm^{-2} s^{-1} sr^{-1} (>100 MeV) and a photon spectral index of –2.1, with no spectral cutoff.

Table 2.2 LAT analysis classes (from [54]).

Analysis Class	Residual Background Rate (Hz)	Characteristics
Transient	2	Maximize effective area, particularly at low energy, at the expense of higher residual background rate; suitable for study of localized, transient sources
Source	0.4	Residual background rate comparable to extragalactic diffuse rate estimated from EGRET; suitable for study of localized sources sources
Diffuse	0.1	Residual background rate comparable to irreducible limit and tails of PSF at high-energy minimized; suitable for study of the weakest diffuse sources expected

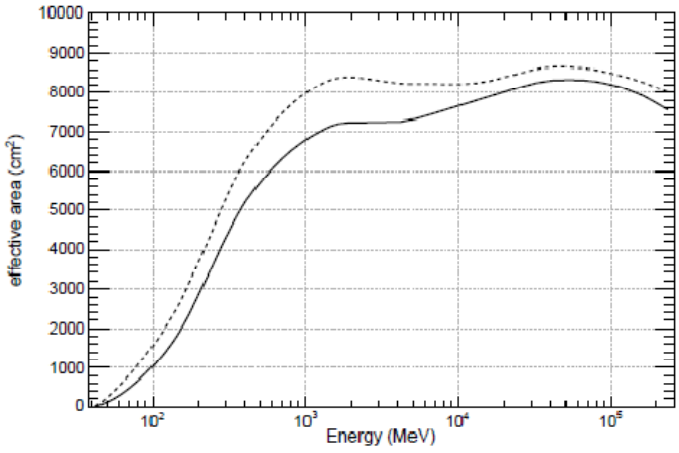

Figure 2.2 Effective area versus energy at normal incidence for P6_V1_DIFFUSE (dashed) and P6_V3_DIFFUSE (solid) event classes. (from [56])

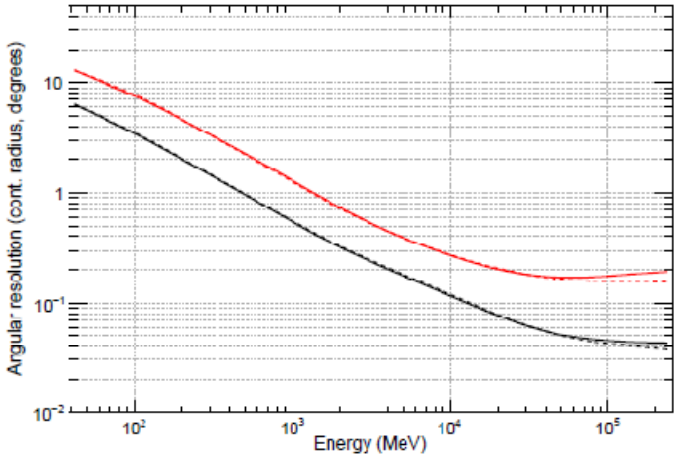

Figure 2.3 68% (black) and 95% (red) PSF containment versus energy at normal incidence for P6_V1_DIFFUSE (dashed) and P6_V3_DIFFUSE (solid) event classes for conversion in the thin (front) section of the TKR. (from [56])

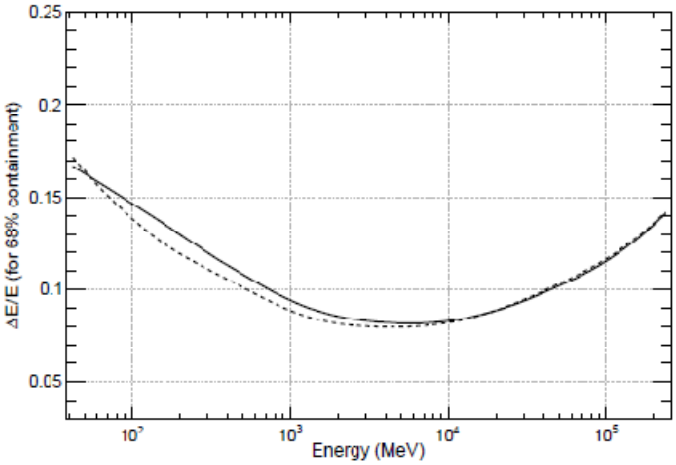

Figure 2.4 68% energy resolution versus energy at normal incidence for P6_V1_DIFFUSE (dashed) and P6_V3_DIFFUSE (solid) event classes. (from [56])

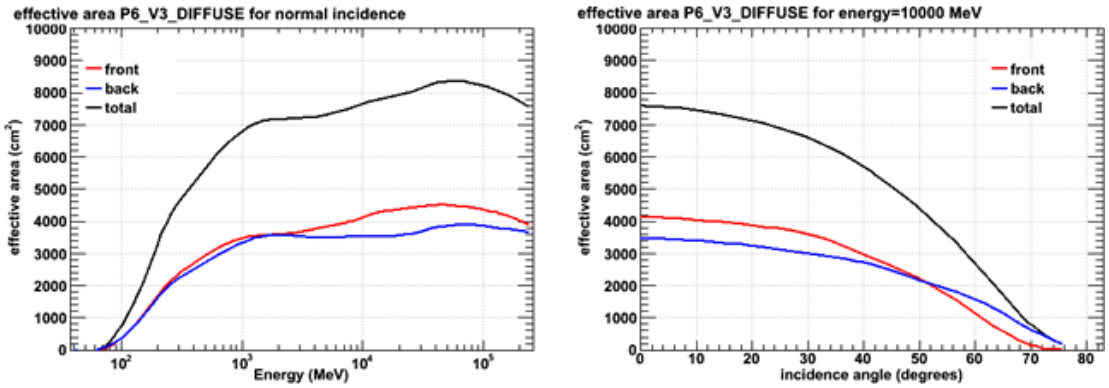

Figure 2.5 Effective area for normal-incidence photons as a function of incident energy on the left and for 10 GeV photons as a function of incident angle on the right for the P6_V3_DIFFUSE class. (from [55])

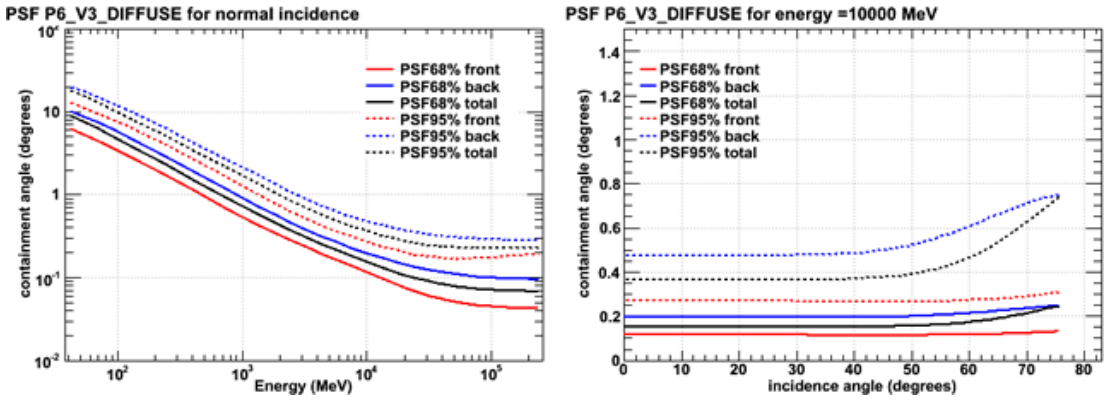

Figure 2.6 68% (solid) and 95% (dashed) PSF containment for normal-incidence photons as a function of incident energy on the left and for 10 GeV photons as a function of incident angle on the right for the P6_V3_DIFFUSE class. (from [55])

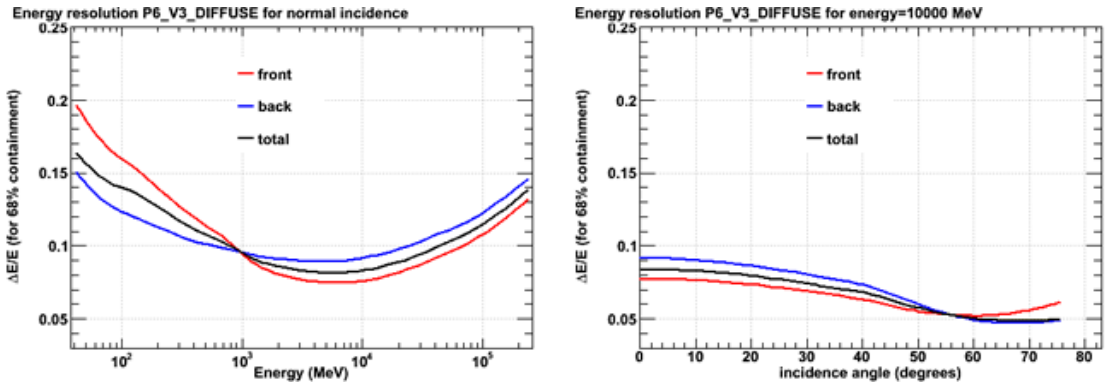

Figure 2.7 68% energy resolution for normal-incidence photons as a function of incident energy on the left and for 10 GeV photons as a function of incident angle on the right for the P6_V3_DIFFUSE class. (from [55])

CHAPTER 3
ESTIMATE OF THE LAT SENSITIVITY TO DM SATELLITES

In this chapter, we describe how to estimate the sensitivity of the LAT to γ-rays produced from DM satellites originating from WIMP annihilation. Since the DM satellites distribute spherically and the most astrophysical backgrounds focus at the Galactic plane, we decided to only search the $|b| > 20^o$ sky for DM satellites to avoid background confusion as much as possible. Generally, the γ-rays from WIMP annihilation are harder than those from the diffuse background, so we use the photons in the energy range 1 – 300 GeV to optimize the LAT efficiency for the detection of DM satellites.

3.1 Signal γ-ray Flux from WIMP Annihilation

The γ-ray continuum flux from WIMP annihilation integrated over a certain energy range and over all the directions is given by [57]

$$\Phi_\gamma = J \times \Phi^{Particle} \tag{3.1}$$

$$J = \int d\Omega \int_{l.o.s} \rho(l)^2 dl$$

$$\Phi^{Particle} = \frac{1}{4\pi} \frac{<\sigma v>}{2M_\chi^2} \int \sum_f \frac{dN_f}{dE} B_f dE$$

The particle physics model enters through the WIMP mass M_χ, the total mean annihilation cross-section σ(υ) multiplied by the relative velocity of the DM particles, υ, at the present time υ/c << 1), and the sum of all the photon yields $\frac{dN_f}{dE}$ for each annihilation channel weighted by the corresponding branching ratio B_f. The

astrophysical distribution of DM is input by the integral along the line of sight (l.o.s) of the assumed density squared, $\rho(l)^2$, of WIMPs.

In this thesis, we discuss five interesting WIMP models:

- Generic WIMP, $b\bar{b}$ channel, WIMP mass $M_\chi = 100\ GeV$, cross-section $< \sigma v >= 3 \times 10^{-26}\ cm^3 s^{-1}$, photon yields $\int_{1GeV}^{300GeV} \sum_f \frac{dN_f}{dE} B_f dE = 13.7$.
- Low mass WIMP; $b\bar{b}$ channel, $M_\chi = 10\ GeV$, $< \sigma v >= 3 \times 10^{-26}\ cm^3 s^{-1}$, $\int_{1GeV}^{300GeV} \sum_f \frac{dN_f}{dE} B_f dE = 0.85$.
- FSR model proposed to fit the ATIC, PAMELA and *Fermi* e^+e^- data, $\mu^+\mu^-$ channel, $M_\chi = 300\ GeV$, $< \sigma v >= 3.8 \times 10^{-24}\ cm^3 s^{-1}$, $\int_{1GeV}^{300GeV} \sum_f \frac{dN_f}{dE} B_f dE = 0.5$.
- Non-thermal Wino LSP WIMP [58], W^+W^- channel, $M_\chi = 177.5\ GeV$, $< \sigma v >= 2.5 \times 10^{-24}\ cm^3 s^{-1}$, $\int_{1GeV}^{300GeV} \sum_f \frac{dN_f}{dE} B_f dE = 13.3$.
- DM model proposed to fit the *Fermi* γ-ray excess from the Galactic center [59], $\tau^+\tau^-$ channel, $M_\chi = 7\ GeV$, $< \sigma v >= 1.5 \times 10^{-26}\ cm^3 s^{-1}$, $\int_{1GeV}^{300GeV} \sum_f \frac{dN_f}{dE} B_f dE = 0.74$.

The photon yields for the above models are calculated by `DarkSUSY` [57], a Monte Carlo package to simulate hadronization and / or decay of the WIMP annihilation products.

To model the distribution of DM satellites, we use the VL2 N-body simulation and extrapolated the satellite mass function down to 1 $M_\odot$. We create 14 realizations of the VL2 satellites as described in §1.5.2.

3.2 Diffuse Background γ-ray Flux

The sensitivities to a DM signal depend critically on accurate estimates of the following backgrounds: Galactic diffuse γ-rays, extragalactic diffuse γ-rays, and residual charged particles in the instrument. For the analyses described in this thesis we use models for the Galactic diffuse emission (gll_iem_v02.fit) and isotropic background (isotropic_iem_v02.txt) that are developed by the LAT team and made publicly available as models recommended for high-level analyses. The models, along with descriptions of their derivation, are available from the *Fermi* Science Support Center [60].

The Galactic diffuse model is a spatial and spectral template. It was developed using spectral line surveys of HI and CO (as a tracer of H_2) to derive the distribution of interstellar gas in Galactocentric rings. Infrared tracers of dust column density were used to correct column densities in directions where the optical depth of HI was either over or under-estimated. The model of the diffuse γ-ray emission was then constructed by fitting the γ-ray emissivities of the rings in several energy bands to the LAT observations. The fitting also required a model of the inverse Compton emission calculated using GALPROP [61] and a model for the isotropic diffuse emission. However, this Galactic diffuse model "gll_iem_v02.fit" is in the energy range from 50 MeV to 100 GeV. Since the high-energy photons for large WIMP masses are very important, we extrapolate this model up to 300 GeV. The details how we did the extrapolation is in Appendix B.

The isotropic component was derived as the residual of a fit of the Galactic diffuse emission model to the LAT data at Galactic latitude $|b| > 30^o$ and therefore included the contribution of residual (misclassified) cosmic rays for the event analysis class used (P6_DIFFUSE). Treating the residual charged particles as effectively an isotropic component of the γ-ray sky brightness rests on the assumption that the acceptance for residual cosmic rays is the same as for γ-rays. This approximation has been found to

be acceptable; the numbers of residual cosmic ray background events scale as the overall live-time and any acceptance differences from γ-rays would not introduce small-scale structure in the models for likelihood analysis.

The above background models provide the differential flux per solid angle. To estimate the background flux in the signal region, we multiply the differential flux at the source position with the solid angle of the DM satellite extension or of the PSF 68% containment at 1 GeV (~0.8^o), whichever is larger.

3.3 LAT Exposure

LAT exposure is defined as the amount of cm^2s, the LAT effective area integrates over the instrument live-time as a function of sky position and off-axis angle and energy, which is a complex calculation. The *Fermi* orbit has about a 52.5-day precession period over which the all-sky scan achieves better than the required ±20% uniformity of exposure on the sky. The 1-year exposure has the required uniformity because of integrating much longer than 52.5 days. Therefore, we assumed the exposure is the same everywhere in the sky with |b| > 20^o.

The on-axis effective area is ~7000 cm^2 at 1 GeV, the field of view is ~2.4 *sr* (20% of the sky) and the live-time fraction is ~70% [62]. Most of dead time is due to time lost during passages through the South Atlantic Anomaly (SAA). There is an increased flux of energetic particles in the SAA, so the LAT does not take data in this region thereby with about 13% time loss. The read out dead time is another main reason for the time loss (9.2%). One can estimate the uniform 1-year exposure for > 1 GeV by,

$$exposure \sim 7000 cm^2 \times 20\% \times 3.15 \times 10^7 s \times 70\% = 3.1 \times 10^{10} cm^2 s$$

One the other hand, we can use `gtexpcube` that is implemented in `Science Tools` to generate an exposure map for one year of the real LAT observation, as

shown in Figure 3.1. Our estimation is quite good compared with the real exposure map.

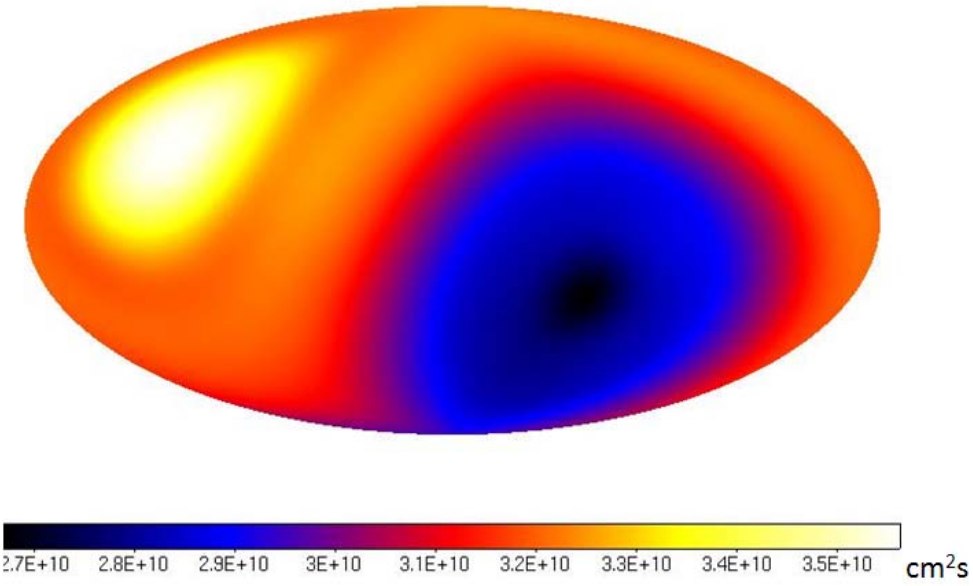

Figure 3.1 The exposure map for one year of the real LAT observation, in units of cm^2s. This exposure is calculated for a photon energy of 1 GeV. The plot is in Galactic coordinates with the values of exposure shown on the color bar.

3.4 Estimated LAT Sensitivity to the VL2 DM Satellites

The prospects for detecting γ-rays from WIMP annihilation are evaluated by comparing the number of expected signal photons N_s to the fluctuation of the observed total events (including both signal and background, N_s+N_b), inside the scale radius (or the PSF 68% containment radius at 1 GeV, whichever is larger). To this purpose we define the detection significance σ_s as:

$$\sigma_S = \frac{N_S}{\sqrt{N_S+N_b}} \tag{3.2}$$

The number of photons is the multiplication of the flux and the exposure. In Table 3.1, we list the number of satellites with $\sigma_s > 5$ for the five WIMP models. The sources with $> 5\sigma$ should be detected. Therefore, in a 1-year observation, for the generic

WIMP model and the FSR model, the LAT will not detect any satellites; for the Wino model, LAT will detect ~ 8 satellites in each realization; for the 10 GeV $b\bar{b}$ model and the 7 GeV $\tau^+\tau^-$ model, the LAT may detect a couple of satellites in some realizations and detect none in other realizations.

This simple estimate does not accurately indicate the LAT detectability to DM satellites. Actually, this method underestimates the LAT sensitivity. The main reason is that Eq (3.2) only compares the signal counts and the background counts in the energy range 1 – 300 GeV, but does not consider the detailed spectral shapes of the signal and the background. If the signal has a very distinctive spectrum, e.g., a monochromatic γ-ray line, the signal will be very easily detected even if the signal counts are much smaller than the background count in a large energy range.

In addition, this estimate only gives the number of satellites that will be detected by the LAT, including point and extended sources, but does not mean those satellites can be identified as DM sources. The fraction of the satellites that can be identified as DM sources depends on the details of our analysis method. This will be discussed in Chapter 6.

Some papers used a similar method to predict the LAT sensitivity [63 – 65], but they calculated the detection significance using $\frac{N_s}{\sqrt{N_b}}$ instead of Eq (3.2). That is inaccurate. In real experiments, the only thing can be measured is the total counts, so it is inaccurate to talk about the fluctuation of only the background events.

Table 3.1 Number of the DM satellites with the significance > 5σ for the five WIMP models based on the VL2 simulation. The Earth position in each realization is given in Table 1.1.

Realization	$N_{5\sigma}$ ($b\bar{b}$; 100 GeV; $3 \times 10^{-26}\ cm^3 s^{-1}$)	$N_{5\sigma}$ ($b\bar{b}$; 10 GeV; $3 \times 10^{-26}\ cm^3 s^{-1}$)	$N_{5\sigma}$ ($\mu^+\mu^-$; 300 GeV; $3.8 \times 10^{-24}\ cm^3 s^{-1}$)	$N_{5\sigma}$ (W^+W^-; 177.5 GeV; $2.5 \times 10^{-24}\ cm^3 s^{-1}$)	$N_{5\sigma}$ ($\tau^+\tau^-$; 7 GeV; $1.5 \times 10^{-26}\ cm^3 s^{-1}$)
0	0	0	0	10	0
1	0	2	0	7	2
2	0	1	0	8	1
3	0	1	0	9	1
4	0	2	0	9	2
5	0	1	0	6	1
6	0	0	0	9	0
7	0	1	0	9	1
8	0	1	0	7	0
9	0	0	0	8	0
10	0	0	0	6	0
11	0	4	0	10	2
12	0	0	0	6	0
13	0	1	0	7	0

CHAPTER 4
DEFINITION AND DISTRIBUTION OF THE TEST STATISTIC IN THE LIKELIHOOD RATIO TEST

4.1 Chernoff's Theorem

In this work we use a standard statistical method used by the LAT collaboration, `gtlike`, and a special statistical method that includes testing for extension of the sources as one option, `sourcelike`. We use these maximum likelihood methods to find the best-fit parameters for a specific model fit to LAT data, and then use the likelihood ratio of two hypothesis models to evaluate which model fit to the data is better. The likelihood ratio is the likelihood of the null hypothesis H_0 for the data divided by the likelihood of the alternative hypothesis H_1 for the same data. The Test Statistic (TS) is defined as -2 times the natural logarithm of the likelihood ratio.

$$TS = 2 \times [\ln(L(H_1)) - \ln(L(H_0))] \quad (4.1)$$

In our fits we limit the amplitudes of sources to be positive. This condition acts like a Bayesian prior in the fitting problem requiring source amplitudes to be greater than or equal to zero as physical source amplitudes should be. This condition means that the asymptotic statistical expectation of the fits should be given by Chernoff's theorem [66], if the asymptotic assumptions of the theorem are satisfied. From Chernoff's theorem, when the two hypotheses are hierarchically nested and the fitted parameter is on one side of a hyperplane, the asymptotic distribution of the TS is that of a random variable, which is zero half the time and behaves like χ^2 with m degrees of freedom (DOF) the other half of the time, where m is the number of additional

parameters that are optimized for the alternative hypothesis, H_1. This theorem can only be applicable under suitable regularity conditions:

- The maximum likelihood estimate must converge to the truth under H_0.
- The nuisance parameters must be identifiable under H_0.

One additional condition to use this theorem is that the number of events in data has to be large enough so that Gaussian statistics applies.

4.2 Limitation of Chernoff's Theorem

If Chernoff's theorem applies, we can easily compare two nested models quantitatively to any high significance level since the χ^2 distribution has an analytical representation. We performed a series of Monte Carlo (MC) simulation tests to verify if Chernoff's theorem applies. However, these tests indicated that this theorem does not apply in our case; actually, it does not apply in many real experiments based on our tests. `Science Tools` and `sourcelike` were used in our tests.

`Science Tools` [67] are being developed jointly by the *Fermi* Science Support Center (FSSC) and the LAT instrument team. This software package is dedicated to the *Fermi* LAT data analysis. The two main programs from `Science Tools` used in this thesis are the observation simulation tool `gtobssim` and the source analysis tool `gtlike`. `Gtobssim` allows users to define celestial γ-ray sources with any spatial and spectral properties. These sources can be point-like or spatially extended. Given incident photons generated according to the input source models, `gtobssim` uses the LAT instrument response functions (IRFs) to select photons as detected in the LAT and assign measured energies and directions. The IRFs, i.e., the effective area, energy dispersion, and PSF, are ascertained from the detailed instrument MC simulations. `Gtlike` uses a maximum likelihood method to fit source spectral parameters such as the flux and the power-law spectral index, though more complex spectral models than a simple power-law are available. It can perform unbinned and

binned likelihood analysis. Since the detected counts for sources near the detection limit will be low, `gtlike` calculates a likelihood function based on the Poisson probability using the source model folded through the LAT IRFs to provide the expected model count. A number of ancillary `Science Tools` are also used that create the counts and exposure maps for the `gtlike` program. The likelihood function employed in `gtlike` is given in Appendix C.

`Sourcelike` (not publicly available) is a software package developed by the *Fermi* LAT collaboration. This tool aims to fit source location and extension simultaneously without much dependence on the spectral shape of the source or the background. It uses energy-dependent binning of the photon data, and fits the signal fraction, the fraction of the observed photons associated with the source, in each energy band independently using a binned likelihood method. The likelihood function is also based on the Poisson probability and given in Appendix C in detail.

4.2.1 Source Extension Test: Toy Model

We did a MC test of a simple toy model to verify Chernoff's theorem. This test was done by Joshua Lande, a fellow Stanford Physics graduate student and a LAT collaborator. He simulated a point source only, and fitted it with two hypotheses and then calculated the TS value, TS_{ext}. The null hypothesis was a point source and the alternative hypothesis was a Gaussian source with a free extension parameter (= σ, width of the Gaussian distribution). In this case, there is only one additional free parameter compared to the null hypothesis – the source extension. There was no background simulated in this test. All of the complications of the LAT analysis, i.e., IRFs, were removed from this test. The PSF was assumed as a Gaussian shape with the width 3^o, so the positions of source events were consistent with the Gaussian distribution. The simulated data was only two dimensional (position) without energy dependence. The fitting was done in a $20^o \times 20^o$ region of interest (ROI) using the

binned likelihood based on the Poisson distribution. The average source counts were ~ 1,000 in the ROI, large enough to use Gaussian statistics. From Chernoff's theorem, TS_{ext} should have a probability density function (PDF) given by,

$$PDF(TS) = \frac{1}{2}(\delta(TS) + \chi_1^2(TS)) \quad (4.2)$$

where $\delta(TS)$ is the Dirac delta function. Therefore, TS_{ext} follows the $\chi_1^2/2$ distribution when $TS_{ext} > 0$. 170 million independent simulations were generated, and the cumulative density function (CDF) of the TS_{ext} is shown in Figure 4.1. The MC result agrees the $\chi_1^2/2$ distribution very well up to a significance level of 5σ.

Then a uniform background was simulated with an average event count ~ 1,000 in the ROI in addition to the source. The simulated source and background data was fitted with background plus point source hypothesis (H_0) and background plus Gaussian extended source hypothesis (H_1). The CDF of TS_{ext} is shown in Figure 4.2; the MC result disagrees by about 10% with the $\chi_1^2/2$ distribution at very low TS_{ext} values. When the average source and background counts are decreased or increased, the MC results deviate from the $\chi_1^2/2$ distribution much more, as shown in Figure 4.3 and Figure 4.4. Therefore, Chernoff's theorem applies with high precision only to the simplest toy case (Gaussian PSF, energy-independent events, no background). Any complication (uniform background, too few or too many event counts) will make the TS distribution start to deviate from Chernoff's theorem at low TS < ~10 (~ 3σ).

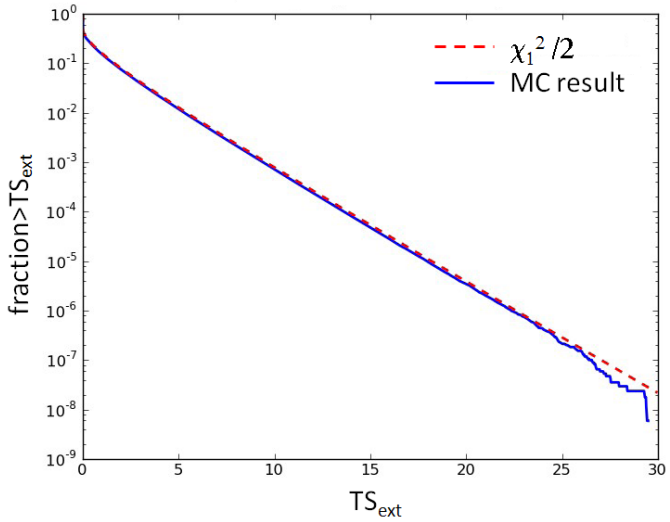

Figure 4.1 CDF of TS_{ext} for a toy model with source simulation only. The average source event count is ~ 1,000 in the ROI. (from Lande's presentation)

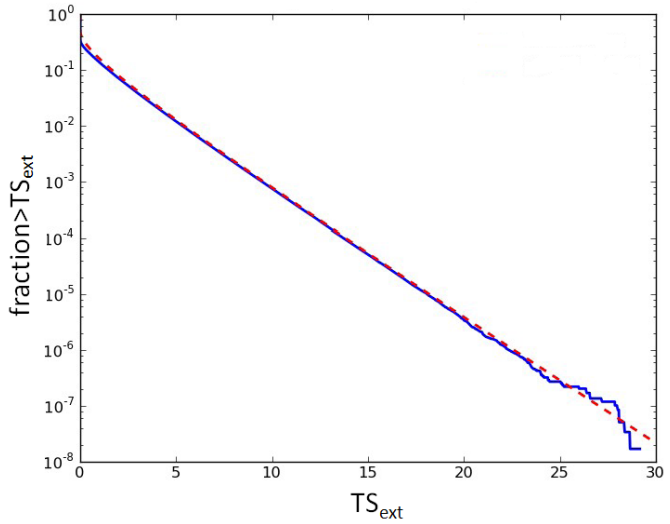

Figure 4.2 CDF of TS_{ext} for a toy model with source and background simulation. The average source event count is ~ 1,000 and the average background event count is ~ 1,000 in the ROI. (from Lande's presentation)

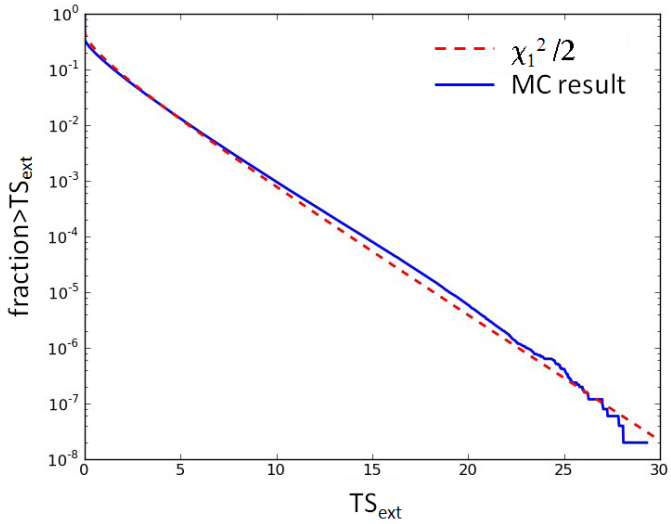

Figure 4.3 CDF of TS_{ext} for a toy model with source and background simulation. The average source event count is ~ 100 and the average background event count is ~ 100 in the ROI. (from Lande's presentation)

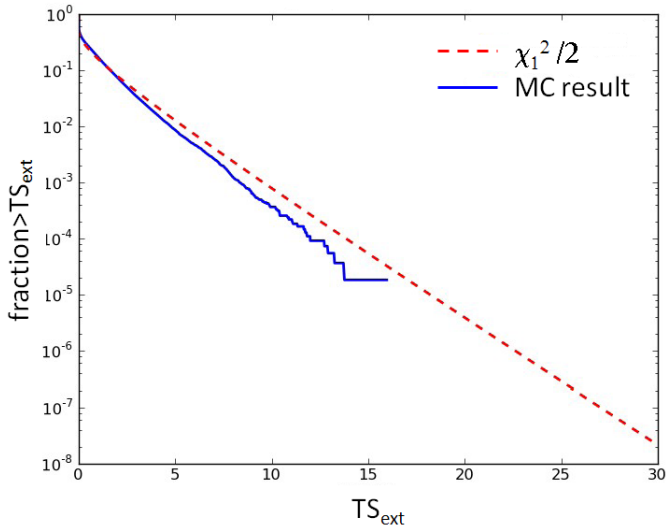

Figure 4.4 CDF of TS_{ext} for a toy model with source and background simulation. The average source event count is ~ 10,000 and the average background event count is ~ 100,000 in the ROI. (from Lande's presentation)

4.2.2 Source Extension Test: Simple Realistic Model

We generated more complicated MC simulations to show whether Chernoff's theorem applied to the source extension test used in this work. One year of LAT observation of a uniform and isotropic diffuse background and a point source was simulated by `gtobssim`. The background had a power-law spectrum with a spectral index -2.1 and an integral flux of $7.32 \times 10^{-6} cm^{-2} s^{-1} sr^{-1}$ from 200 MeV to 300 GeV [68].; the embedded point source had a power-law spectrum with a spectral index -2.0 and an integral flux $5.0 \times 10^{-8} cm^{-2} s^{-1}$ from 200 MeV to 300 GeV. The source was placed at a randomly chosen high-latitude location, *(l, b) = (272^o, 36^o)* in Galactic coordinates. Then two hypotheses, H_0 and H_1, were fitted by `sourcelike`. In order to make sure the two hypotheses were nested, a pseudo Gaussian source with a fixed extension, 10^{-8} radians, much smaller than the LAT PSF, was used in the null hypothesis, H_0. The alternative hypothesis, H_1, was a Gaussian source with a free extension. There was only one additional free parameter – the source extension for H_1. The fitting was done only in one energy band, 200 – 400 MeV, in which the radius of the ROI is ~14^o. The distribution of the TS_{ext} for 1000 independent simulations is shown in Figure 4.5. From Eq (4.2), TS_{ext} should follow the $\chi_1^2/2$ distribution when $TS_{ext} > 0$. The CDF of TS_{ext} for $TS_{ext} > 0$ is shown in Figure 4.6. The MC result does not follow the $\chi_1^2/2$ curve at all.

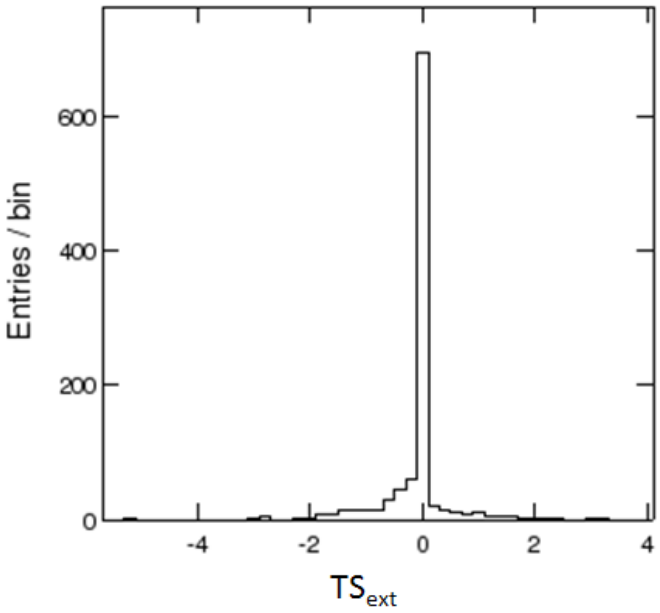

Figure 4.5 TS_{ext} distribution for 1000 independent simulations. The source flux is $5.0 \times 10^{-8} cm^{-2} s^{-1}$.

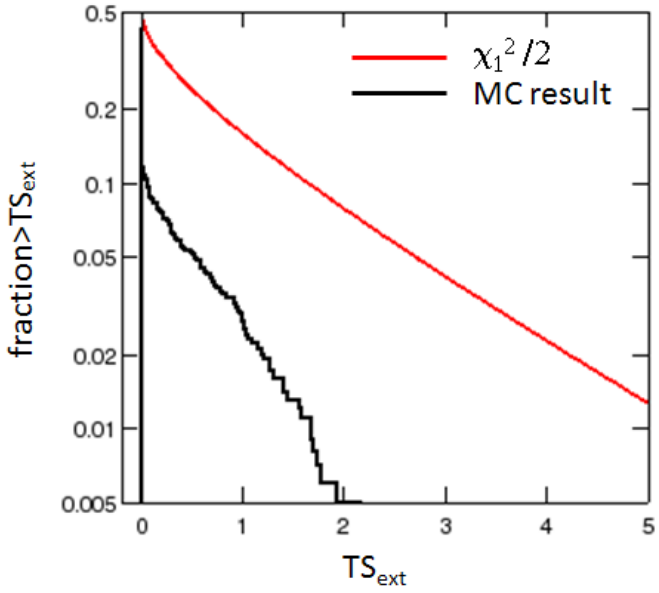

Figure 4.6 CDF of TS_{ext} for 1000 independent simulations (black curve), and cumulative distribution of $\chi_1^2/2$ (red curve) for $TS_{ext} > 0$. The source flux is $5.0 \times 10^{-8} cm^{-2} s^{-1}$.

4.2.3 Source Detection Test: Simple Realistic Model

We used MC simulations of background only to show whether Chernoff's theorem applied to the source detection. The uniform background MC is the same as described in §4.2.2. Two hypotheses, H_0 and H_1,were fitted by `sourcelike` to the background only MC data. The null hypothesis, H_0, was background only and the alternative hypothesis, H_1, was background plus a point source at $(l, b) = (272^o, 36^o)$. There was only one additional free parameter – the signal fraction for H_1. The fitting was also done in only one energy band, 200 – 400 MeV. In the ROI, there were ~ 24,000 events which was large enough to use Gaussian statistics. The distribution of the TS_{point} for 1000 independent simulations is shown in Figure 4.7. The CDF of TS_{point} for $TS_{point} > 0$ is shown in Figure 4.8. The MC result does not agree the $\chi_1^2/2$ curve.

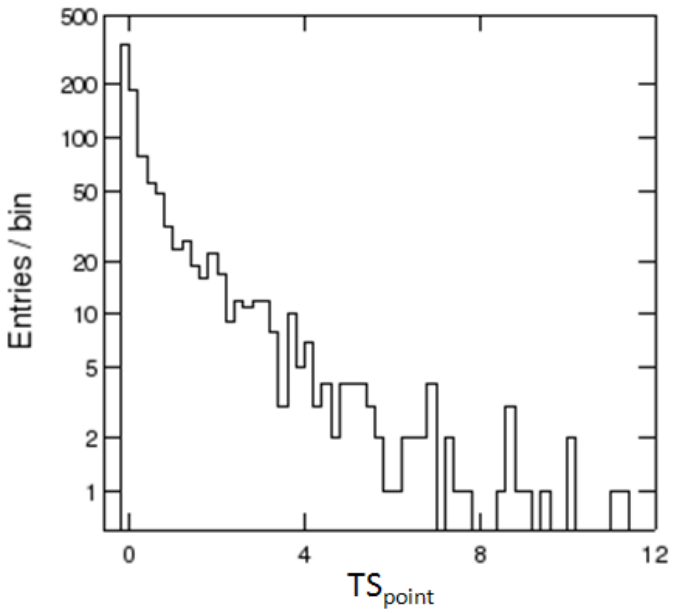

Figure 4.7 TS_{point} distribution for 1000 independent simulations of background only.

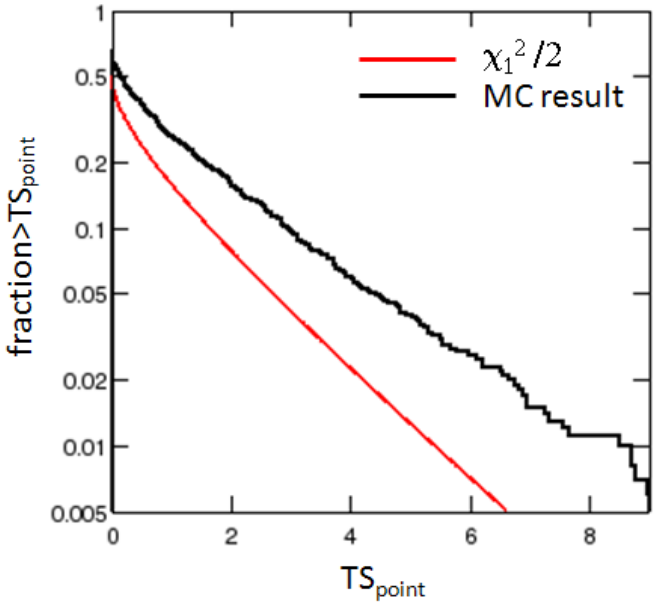

Figure 4.8 CDF of TS_{point} for 1000 independent simulations of background only (black curve), and cumulative distribution of $\chi_1^2/2$ (red curve) for $TS_{point} > 0$.

4.2.4 Source Detection Test: Very Realistic Model

In the analysis of real data, we fit the data in the energy range 200 MeV – 300 GeV using 11 energy bins with lower energies of 200, 400, 800, 1600, 3200, 6400, 12800, 25600, 51200, 102400, 204800 MeV in each bin. During the source detection, we fit data with background only hypothesis and background plus a point source hypothesis. There is only one additional free parameter – signal flux in each energy bin, so the PDF of the TS for each energy bin follows Eq (4.2). Since the final TS_{point} is the sum of the TS in all the energy bins, the PDF of TS_{point} is a convolution of Eq (4.2):

$$PDF(TS_{point}) = \frac{1}{2^n}(\delta(TS_{point}) + \sum_{m=1}^{n}\binom{n}{m}\chi_m^2(TS_{point})) \quad (4.3)$$

where n is the number of the energy bins (n = 11 in our analysis), $\binom{n}{m}$ is the binomial coefficient and χ_m^2 is χ^2 distribution with m degrees of freedom. The CDF of TS_{point} is

$$CDF(TS_{point}) = \int_{TS_{point}}^{\infty} \frac{1}{2^n}(\delta(TS) + \sum_{m=1}^{n} \binom{n}{m} \chi_m^2(TS))dTS \quad (4.4)$$

We did two realizations of 1-year diffuse background MC simulation in 200 MeV – 300 GeV. The diffuse background included the extrapolated LAT Galactic diffuse model (Appendix B) and the LAT isotropic diffuse model. For the sky with $|b| > 20^o$, there are 27,144 deg^2. For each realization, in order to avoid the correlations due to the too close locations, we only chose 25,000 random locations at $|b| > 20^o$ and fitted with background only hypothesis and background plus a point source hypothesis. The distribution of the randomly chosen locations is uniform. This method can average the background fluctuations for the high latitude sky and does not bias for any specific location. The CDF of the TS_{point} of 50,000 samples is shown in Figure 4.9. It is clear that the MC result does not agree with Eq (4.4) for n = 11 or even for any n value. From the MC result, we found the cutoff value $TS_{point} = 24$ for the significance level of 10^{-4} which corresponds to a one-sided 3.7σ significance. We will use this cutoff value latter in the source detection in §5.2.1.

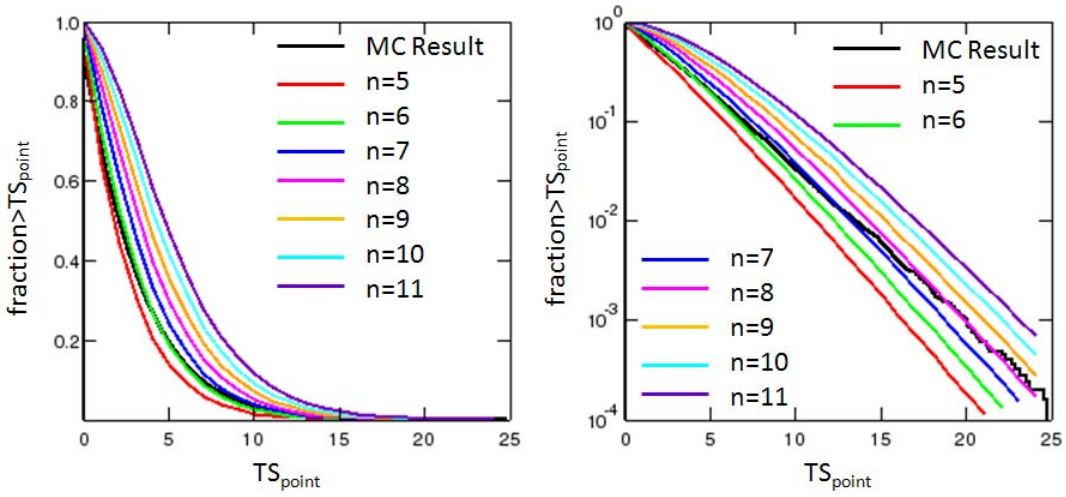

Figure 4.9 CDF of TS_{point} of 50,000 random locations for background only simulation (black curve). Different color curves are Eq (4.4) for different values of n. Left panel is in linear scale. Right panel is in logarithm scale.

4.2.5 Conclusion

Chernoff's theorem does not apply to the source extension test and the source detection test, even for a simple power-law uniform background and for only one energy band. The TS distribution varies with many different factors, e.g., source and background intensity. In final analysis, we must use MC simulation to determine the TS distribution and cutoff values. Computer time then limits the value of TS we can accurately test to.

CHAPTER 5
ANALYSIS OF ONE YEAR OF LAT DATA

In this chapter, we present the analysis method for the search for DM satellites using one year of LAT data. The criteria to identify a source as a DM satellite are:

- unassociated with other known sources
- has spatial extent
- has non-power-law spectra or extremely hard power-law spectra ($\sim E^{-1}$)
- no time variability
- no astronomical counterparts in x-ray, radio or CO observations (molecular clouds)

5.1 Dataset

For the analysis of LAT data, we select events based on the online caveats [69].

- "DIFFUSE" class is recommended to use for all point and extended source analysis. Other event classes have higher charged-particle background contamination and may result in spurious spectral features.
- Data below 100 MeV can not be used for spectral analysis because of the rapid change of effective area with energy and because of residual uncertainty in the instrument response. For best results, we recommend starting above 200 MeV.
- Given the current limited statistics in the study of IRFs at hundreds of GeV, we recommend limiting spectral analysis to energies less than 300 GeV.

Therefore, one year of LAT data (Aug 8th 2008 – Aug 7th 2009) is used in this thesis and only "DIFFUSE" class events with the reconstructed energy in the range

200 MeV – 300 GeV are considered. To avoid albedo γ-ray contamination, we also apply a maximum zenith angle cut of 105^{o} and a maximum rocking angle cut of 47^{o} as during the data collection time for this work, the LAT rocking angle for nominal all-skay scanning was $\pm 35^{o}$. Throughout, we use the *Fermi* `Science Tools` version v9r18p1 and P6_V3_DIFFUSE IRFs.

5.2 Unassociated Sources at High Latitude

The LAT Catalog Group has published the bright source list based on 2.5 months data in 2009 [70] and the first *Fermi* Gamma-ray LAT (1FGL) source catalog based on 11 months data in 2010 [62]. The analysis method used in these papers assumed only point sources in the search, thus faint and extended sources might be missed from the catalogs since these sources would have a lower significance when using a point source hypothesis. In addition, some non-power-law sources could also be omitted from the catalog because all the sources were modeled with simple power-law spectra in the catalog analysis, and this might lead to very low significance for a candidate source due to the spectral fits not converging if the source has an unconventional spectrum. Finally, the *Fermi* catalogs used data in the energy range 100 MeV to 100 GeV; however, the LAT energy reconstruction algorithm below 200 MeV is still under study at this writing. When attempting to work below 200 MeV for this study, we obtained results inconsistent with those obtained when starting above 200 MeV. Thus we have concluded that data below 200 MeV is not reliable for the characterization of faint extended sources at this time. In addition, omitting photons with energy larger than 100 GeV might limit the detectability of hard spectrum sources. Therefore, in this analysis we use P6_V3_DIFFUSE class photons in the energy range 200 MeV to 300 GeV.

Given the above discussions, we independently search the sky in a way that is sensitive to faint extended sources on the 1^{o} scale. `Sourcelike` is chosen as our

primary tool because it can search for extended and point sources without much dependence on the spectral shape of the source.

We do not expect that using `sourcelike` alone can rediscover all the sources in the 1FGL catalog because the 1FGL catalog is a union of the results from four different detection methods as well as including external seeds from the BZCAT and WMAP catalogs [62]. However, we do expect `sourcelike` to find some faint sources which are not in the 1FGL catalog due to the issues mentioned above.

Ultimately, we combine the sources which are in our `sourcelike` result but not in the 1FGL catalog (non-1FGL sources) and the unassociated sources in the 1FGL catalog as our candidate source list. Therefore, we will analyze not only all the unassociated sources in the 1FGL but also some non-1FGL sources.

5.2.1 Search Algorithm of `sourcelike`

`Sourcelike` uses hypothesis testing. It uses the Test Statistic (TS), defined as -2 times the natural logarithm of the likelihood ratio, to tell which hypothesis is better fitting the data.

We are interested in the sky with $|b| > 20^o$ because the Region Of Interest (ROI) for our source analysis should not include the region within 5^o of the galactic plane (gas emission and source confusion) and our ROI size is about 15^o radius at low energy.

`Sourcelike` uses energy-dependent binning of the photon data, choosing 11 energy bands in 200 MeV – 300 GeV. It searches for candidate point sources by maximizing the likelihood function for trial point sources and yields a TS at each direction in a HEALPix (Gorski et al. 2005) order 9 (pixel size ~ 0.1^o x 0.1^o)

tessellation of the sky, i.e., a TS map on the sky. For our case, 2496 pixels are searched ($|b| > 20^o$). At this step, we assume that the diffuse background is adequately described by the LAT Galactic diffuse model and the isotropic diffuse model and ignore any nearby point sources. After the initial localization is performed, the bright spots in the TS map of the sky indicating the more significant sources (TS > 16) are refit taking nearby bright neighbors (TS > 16) into account. The likelihood is optimized with respect to the signal fraction in each energy band, with the TS being the sum over all the bands. This makes the result independent of the spectrum of the point source or of the diffuse background. The source list is then further pruned by removing sources with TS < 24 which is the cutoff value for the significance level of 10^{-4} as discussed in §4.2.4.

Comparing the above source list with the 1FGL catalog, we decided that the two sources were the same if the error circles of their locations had any overlap. After removing from our source list the sources which are in the 1FGL and combining the remaining sources we found with the unassociated sources in the 1FGL, we obtained a new catalog of the high latitude unassociated sources.

5.2.2 High-latitude Unassociated Sources in One Year of LAT Data

We searched the high latitude sky with $|b| > 20^o$ using `sourcelike`, and found 710 sources among which 154 sources are not in the 1FGL catalog. Combining the 154 non-1FGL sources with the 231 unassociated sources with $|b| > 20^o$ in the 1FGL catalog, we obtained our new catalog of the high latitude unassociated sources with 385 sources in total.

The 385 unassociated sources were then analyzed over the full energy range from 200 MeV to 300 GeV with an unbinned likelihood technique implemented in `gtlike`. We employed a point-source spatial model and a power-law spectral model for each

source. Figure 5.1 shows the distribution of the spectral index and the integral flux from 200 MeV to 300 GeV for the 385 unassociated sources. The black squares are the 231 unassociated sources with $|b| > 20^o$ in the 1FGL catalog. The red squares are the 154 non-1FGL sources with $|b| > 20^o$. The strong correlation between spectral indices and fluxes is due to the LAT sensitivity to point sources. It is apparent that there are more non-1FGL sources in this sample with very hard spectra (spectral index ~ -1.0) and very low fluxes (~ 10^{-10} cm^{-2} s^{-1}).

We selected 5 typical spectral indices: -0.9, -1.5, -2.0, -2.5 and -3.0, and found the minimum and maximum integral flux from 200 MeV to 300 GeV for each spectral index, as shown in Table 5.1. Those 10 power-law models are a representative of the 385 unassociated sources. When we developed and tested our analysis method to distinguish DM satellites from usual astrophysical sources, we would use those 10 power-law models as a representative of usual astrophysical sources that the LAT could detect.

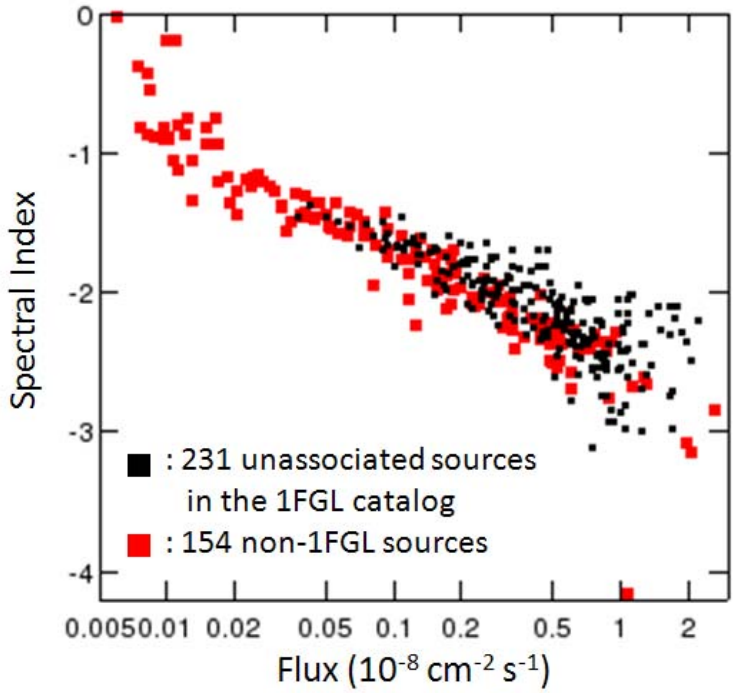

Figure 5.1 Distribution of the spectral index and the integral flux from 200 MeV to 300 GeV for the 385 unassociated sources. The black squares are the 231 unassociated sources with $|b| > 20^o$ in the 1FGL catalog. The red squares are the 154 non-1FGL sources with $|b| > 20^o$ found by `sourcelike` in this work.

Table 5.1 10 representative power-law models of the 385 unassociated sources and their range of fluxes detected by the LAT.

Spectral Index	Minimum Flux (10^{-8} cm^{-2} s^{-1})	Maximum Flux (10^{-8} cm^{-2} s^{-1})
-0.9	0.008	0.02
-1.5	0.02	0.11
-2.0	0.12	1.2
-2.5	0.5	2.1
-3.0	1.0	1.7

5.2.3 Spurious Sources

The TS of each source can be related to the probability that such an excess can be obtained from background fluctuations alone. Mattox et al. [71] showed that, as the expectation based on Wilks' theorem (actually Chernoff's theorem), the distribution of TS at a fixed point for the background only simulation data followed 1/2 of the χ^2 distribution with one degree of freedom (one additional parameter: the number of point-source counts). However, our case is much more complex than the above simulated case of Mattox et al. `Sourcelike` fits the signal fraction in each energy band, so it has many more degrees of freedom than a constrained power-law fit over the entire energy range. In Chapter 4, we have shown that our TS distribution did not follow Chernoff's theorem at all.

Since Chernoff's theorem does not seem to apply in our case, to estimate the number of spurious sources, we decided to apply the same search method to the background MC data (Galactic and isotropic diffuse only) as we did to one year of real LAT data. The real data was in the energy range 200 MeV – 300 GeV, so the MC data was also required to be in this energy range. However, the standard LAT Galactic diffuse model "gll_iem_v02.fit" is a mapcube from 50 MeV to 100 GeV. For consistency with the range of the data used, this model was extrapolated from 100 GeV up to 300 GeV (Appendix B). The one year of *Fermi* observation simulation of the diffuse background was generated by `gtobssim` based on the actual LAT pointing history. The same cuts were applied to the MC data as applied to the real data (P6_V3 IRFs, time range, energy range, zenith angle and rocking angle).

We searched the background MC data for $|b| > 20^o$ using `sourcelike`, and found 193 sources. Of course, in this case the 193 sources are all spurious sources. Figure 5.2 shows the location distribution in galactic coordinates of the 193 spurious sources. This distribution is uniform over the high-latitude sky. There is no indication of any spatial features as is expected as these spurious sources arise from random

fluctuations in the background. The locations of the spurious sources have no coincidences with any of the “real” 385 unassociated sources found in the real LAT data.

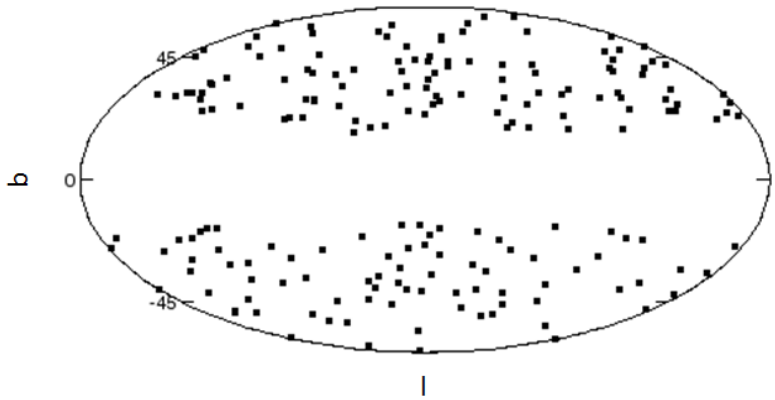

Figure 5.2 Location distribution in galactic coordinates of the 193 spurious sources found in MC data with `sourcelike`.

The 193 spurious sources were also individually analyzed with `gtlike`, using a point-source spatial model and a power-law spectral model. Figure 5.3 shows the distribution of the spectral index and the integral flux from 200 MeV to 300 GeV for the 193 spurious sources (blue crosses) and the 385 unassociated sources (black and red squares). The same correlation between spectral indices and fluxes hold for the spurious sources and the unassociated “real” sources.

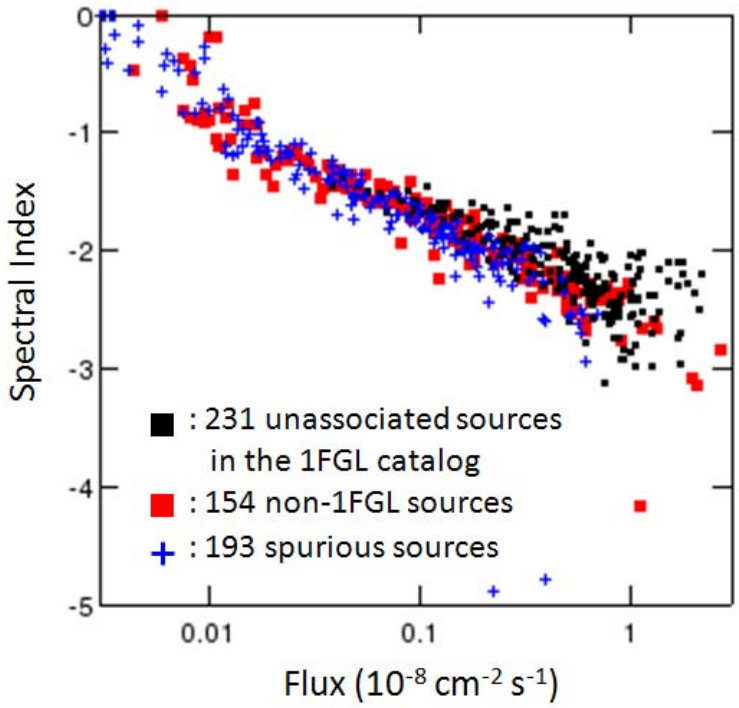

Figure 5.3 The spectral index versus the integral flux from 200 MeV to 300 GeV for the 193 spurious sources and 385 unassociated "real" sources. The blue crosses are the 193 spurious sources. The black squares are the 231 unassociated sources with $|b| > 20^o$ in the 1FGL catalog. The red squares are the 154 non-1FGL sources with $|b| > 20^o$.

We specifically studied the spurious sources and unassociated sources with the spectral index in the range from -1.0 to -0.7. In this spectral index range, there are 12 spurious sources and 13 unassociated "real" sources. We applied the P6_V3_EXTRADIFFUSE cuts (an event class to obtain a cleaner photon sample than the DIFFUSE class, not publicly available), which removed most of the charged particle background at high energy, to the 13 unassociated "real" source photons. This resulted in the reduction of the source significance and two sources even disappeared (TS ~ 0), which implied that some unassociated hard sources detections were due to the high energy charged particle contamination. Then we compared the spatial and spectral distribution of the P6_V3_EXTRADIFFUSE photons from the 13

unassociated sources with the simulated photons from the 12 spurious sources, and found no obvious difference. We also analyzed those 13 unassociated "real" sources using 25 months of LAT data, and 10 of them showed a decrease in source significance compared to one year of data. Thus, these 13 unassociated sources have a high probability of being spurious sources arising from coincidence of background photons and / or charged particle background.

The TS distribution of the 193 spurious sources is shown in Figure 5.4. The horizontal axis is the TS calculated by `gtlike`, and the vertical axis is the TS calculated by `sourcelike`. The red line shows TS_sourcelike = TS_gtlike. Most spurious sources had TS_sourcelike > TS_gtlike, because of the extra degrees of freedom when fitting using `sourcelike`. In general, the TS values of the spurious sources were less than 40, no matter if calculated by `sourcelike` or `gtlike`. The TS values (from `sourcelike` and `gtlike`) of the 13 unassociated "real" sources with spectral index in the range from -1.0 to -0.7 were all less than 40.

Given the discussion above, we concluded that the 13 unassociated "real" sources with the spectral index in the range from -1.0 to -0.7 were spurious sources. Moreover, it appears clear that it is not appropriate to use "DIFFUSE" class events to detect and analyze hard sources because there is too much charged particle contamination at high energy in the P6_V3_DIFFUSE class. "DATACLEAN" class [72] events would be the best choice to detect and analyze faint hard sources.

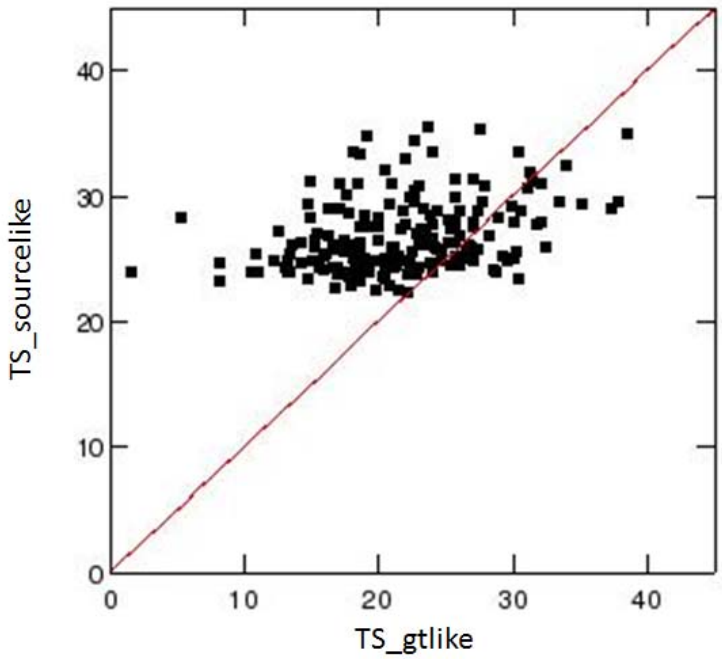

Figure 5.4 The TS distribution of the 193 spurious sources. The horizontal axis is the TS calculated by `gtlike`, and the vertical axis is the TS calculated by `sourcelike`. The red line shows TS_sourcelike = TS_gtlike.

We did another independent realization of diffuse background MC simulation, and this time found 188 spurious sources using `sourcelike`. The spatial distribution and TS distribution of the 188 spurious sources were similar to what was shown above. Therefore, we could confirm the distribution of spurious sources due to the diffuse background fluctuations and charged-particle background found by `sourcelike`.

5.3 Source Extension Test

5.3.1 Source Extension of the VL2 Satellites

As described in Appendix A and §1.5.2, we extrapolated the mass function of the VL2 DM satellites down to 1 $M_{\odot}$ and created 14 realizations of the VL2 satellites

corresponding to 14 viewpoints on the 8.5 *kpc* solar sphere centered on the galactic center. Since the 14 realizations are not independent VL2 simulations, the same satellites may appear in more than one viewpoint realization. By pre-cutting on the satellite distance and mass, there are 9758 satellites in total for the 14 realizations among which 6690 satellites have $|b| > 20^o$ (478 high-latitude satellites per realization on average). The distribution of the satellite extension, MC truth known from the simulation, for the 6690 satellites, R_0, is shown in Figure 5.5. The extension of the NFW source is defined as the angle subtended by the scale radius, $R_0 = r_s/D$. This extension is actually three times the 68% containment radius of the source flux, R_{68}. For example, 68% of the photons produced by an NFW source with a 1^o extension are contained in a circle with a 0.33^o radius. Thus, an NFW source with a few degrees extension in scale radius actually does not appear very extended in the LAT. From Figure 5.5, the extension distributions of the 5103 original VL2 satellites, and the 1587 low-mass satellites obtained by extending the mass function are very consistent. The satellite with the largest extension, 9^o, is a low-mass satellite with the mass $1.1 \times 10^4\ M_\odot$ and with the distance to the Earth of 0.07 *kpc*.

The LAT PSF, which depends on the photon energy and angle of incidence, can be approximated by the function$0.8^o(\frac{E}{1GeV})^{-0.8}$, yielding ~$0.8^o$ at 1 GeV and ~ 0.13^o at 10 GeV. Therefore, we do not expect to resolve satellites with extension < 0.5^o (R_{68} = 0.17^o) for large DM mass, or satellites with the extension < 1.0^o ($R_{68} = 0.33^o$) for small DM mass. There are 375 satellites with $|b| > 20^o$ and $R_0 > 0.5^o$ for the 14 realizations (27 satellites per realization on average). Figure 5.6 shows the distribution of the J value versus the extension of those 375 satellites, where the J value is defined in Eq (1.5) as the line of sight integral of the DM density distribution squared.

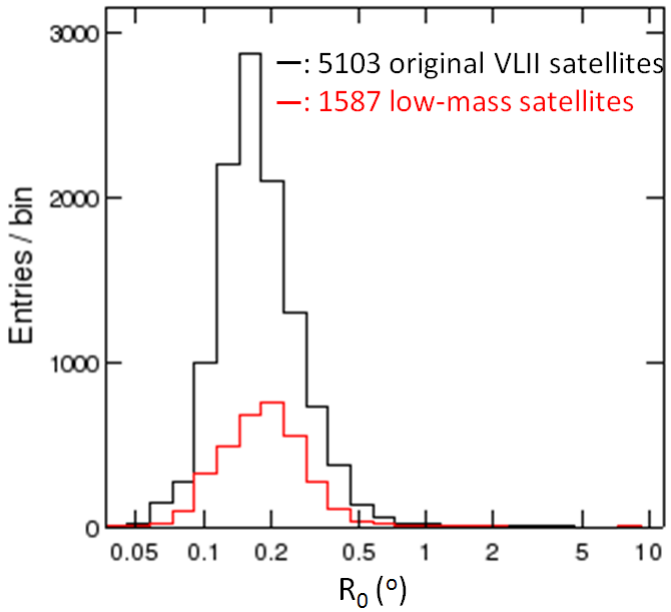

Figure 5.5 Satellite extension for the 6690 satellites with $|b| > 20^o$ for the total 14 realizations. 5103 original VL2 satellites are shown in black and 1587 low-mass satellites are shown in red.

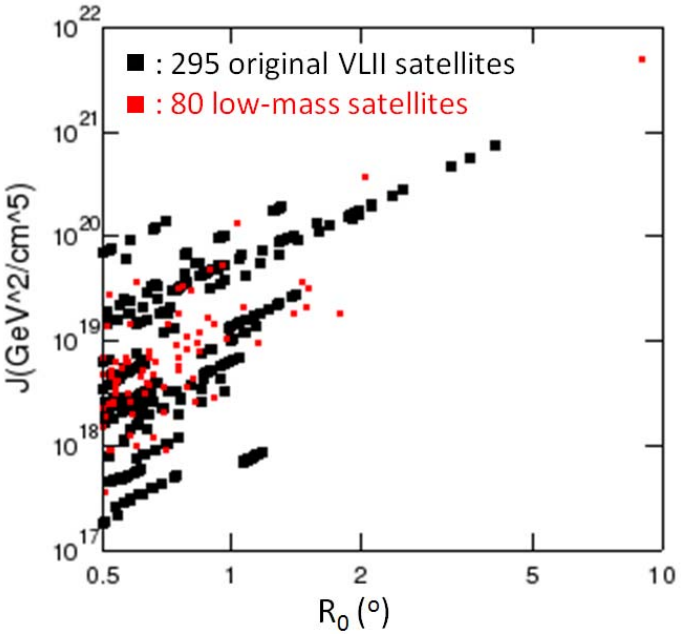

Figure 5.6 Satellite extension versus J value of the 375 satellites with $|b| > 20^o$ and $R_0 > 0.5^o$ for the 14 realizations. 295 original VL2 satellites are shown in black and 80 low-mass satellites are shown in red. The correlation between J and R_0 is because some different realizations contain the same satellites.

We used TS_{ext} to determine the extension of sources. For this application, the null hypothesis was a point source, and the alternative hypothesis was an extended source with the NFW profile. In order to make sure the two hypotheses were nested, a pseudo NFW source with a fixed extension, 10^{-8} radians, much smaller than the LAT PSF, was used as the null hypothesis.

When fitting the null hypothesis, the signal fraction and the localization of the source were free parameters. The extension of the source was an additional free parameter when fitting the alternative hypothesis. Based on Chernoff's theorem [66], the TS_{ext} should be distributed as $\chi_1^2/2$ when $TS_{ext} > 0$. However, in Chapter 4, we showed that Chernoff's theorem did not apply to the source extension test. Therefore, we had to use MC simulations to decide on our cutoff value of TS_{ext} at the significance level (meaning the probability to reject the null hypothesis when it is in fact true) of 0.01 instead of using Chernoff's theorem. To determine the significance level of 0.01 to sufficient statistical precision requires 1000 simulations.

5.3.2 Source Extension Test Using Embedded MC Simulation

In the real data analysis, many uncertainties may affect the source extension test, such as some subtle structures in the background not well characterized in the diffuse model and some faint undetected sources around the target source. In order to model the situation we would face when analyzing the real data, we decided to combine a MC point source with one year of real LAT data and then obtained the TS_{ext} distribution.

To derive the significance level of the test, a point source was simulated. Instead of simulating and fitting a point source at a fixed location 1000 times, we placed a MC point source at a random location for $|b| > 20^o$ 1000 times. The distribution of the

randomly chosen locations was uniform on the sky. This method averaged the fluctuations on the high-latitude sky and did not bias for any specific location. The simulation was based on the actual *Fermi* pointing history using `gtobssim` and P6_V3_DIFFUSE IRFs. For the point source simulation, 10 typical power-law models in Table 5.1 were chosen to determine the effects of different spectral indices and fluxes to the source extension test.

For each simulation, we used `sourcelike` to calculate TS_{point} for the null hypothesis and TS_{NFW} for the alternative hypothesis, and then obtained $TS_{ext} = TS_{NFW} - TS_{point}$. The fitting results are in Table 5.2. The first two columns are the spectral index and the integral flux from 200 MeV to 300 GeV; the third and forth columns are the average values of TS_{NFW} and TS_{point} for 1000 simulations. The last column, $TS_{ext}^{0.01}$, is the cutoff value of TS_{ext} at the significance level 0.01. The $TS_{ext}^{0.01}$ value varied a lot for different spectral indices and fluxes. Given this behavior, we could not use one universal cutoff value for all the sources. Thus, we decided to linearly interpolate the $TS_{ext}^{0.01}$ in the two-dimensional space of spectral indices and fluxes according to the values in Table 5.2.

Table 5.2 Source extension test results of the embedded MC simulation for the 10 typical power-law point source models. The last column shows the cutoff values of TS_{ext} at the 0.01 significance level.

Spectral Index	Flux (cm^{-2} s^{-1})	$< TS_{NFW} >$	$< TS_{point} >$	$TS_{ext}^{0.01}$
-0.9	2.0×10^{-10}	40.58	40.31	6.18
-0.9	8.0×10^{-11}	23.69	23.44	7.87
-1.5	1.1×10^{-9}	58.52	58.25	5.09
-1.5	2.0×10^{-10}	19.25	18.82	14.98
-2.0	1.2×10^{-8}	240.03	239.68	5.11
-2.0	1.2×10^{-9}	22.59	22.13	9.63
-2.5	2.1×10^{-8}	210.03	209.56	6.74
-2.5	0.5×10^{-8}	31.09	30.56	10.78
-3.0	1.7×10^{-8}	90.28	89.75	9.81
-3.0	1.0×10^{-8}	46.78	46.12	11.87

5.3.3 High-latitude Unassociated Extended Sources in One Year of LAT Data

For each of the 385 unassociated sources, we interpolated $TS_{ext}^{0.01}$ values in Table 5.2 according to the source's best fit spectral index +/- 1σ error and best fit flux +/- 1σ error to obtain four different cutoff values for each source. Then we chose the largest cutoff value as the $TS_{ext}^{0.01}$ for such source and determined whether the source was extended or not. After cutting the TS_{ext} values of the 385 unassociated sources, two sources preferred the extended NFW profile with the significance level of 0.01. These two extended sources are also in the 1FGL catalog. The detailed information is listed in Table 5.3.

1FGL J1302.3-3255 is unassociated in the 1FGL catalog, but it is identified as a millisecond pulsar by a follow-up observation of NRAO's Green Bank Telescope in December 2009. The LAT detection of this pulsar has not been publically reported by the LAT collaboration at the time of this writing. (This will be in the Second Millisecond Pulsar Population paper to be published.)

The other unassociated and possibly extended source 1FGL J2325.8-4043 may be associated with two AGNs, 1ES_2322-409 and PKS_2322-411, in the First LAT AGN Catalog (1LAC) [72], and this is a probable reason that it turns out extended. The probability that 1ES_2322-409 was the correct association was 70% and the probability that PKS_2322-411 was the correct association was 55%. The association threshold is 80% for the 1FGL catalog and 10% for the 1LAC catalog. Therefore, it is unassociated in the 1FGL catalog but associated in the 1LAC catalog.

On the other hand, since the significance level of the extension test is 0.01, we expect to find 3.85 (= 385 * 0.01) spurious extended sources due to the fluctuation in the 385 unassociated sources. Based on the Poisson distribution, the probability to find at least one spurious extended source is 98%.

In addition, we did the same extension test to the spurious sources as described in §5.2.3, and no spurious sources preferred the NFW profile.

Table 5.3 Two possibly extended unassociated sources with $|b| > 20^o$ with the significance level of 0.01.

1FGL Name	RA (^{o})	Dec (^{o})	r_{68} (^{o})	l (^{o})	b (^{o})	R_0 (^{o})	TS_{NFW}	TS_{point}	TS_{ext}	Flux (10^{-8} cm^{-2} s^{-1})	Spectral Index	$TS_{b\bar{b}}$	TS_{pwl}	TS_{spec}
1FGL J1302.3-3255	195.51	-32.87	0.05	305.50	29.95	1.2	141.1	131.9	9.3	1.07 ± 0.23	-2.05 ± 0.10	124.0	119.4	4.6
1FGL J2325.8-4043	351.53	-40.72	0.045	349.76	-67.79	1.3	219.5	206.3	13.2	1.99 ± 0.31	-2.36 ± 0.095	230.8	250.0	-19.1

The description of all the columns:

1FGL Name	Source name in the 1FGL catalog
RA	Right Ascension
Dec	Declination
r_{68}	68% error radius of the source location
l	Galactic Longitude
b	Galactic Latitude
R_0	Best fit source extension calculated by `sourcelike` assuming the source has the NFW profile
TS_{NFW}	TS value calculated by `sourcelike` assuming the source has the NFW profile
TS_{point}	TS value calculated by `sourcelike` assuming the source is a point source
TS_{ext}	$TS_{NFW} - TS_{point}$
Flux	Best fit integral flux from 200 MeV to 300 GeV and 1σ error calculated by `gtlike` assuming the source is a point power-law source
Spectral Index	Best fit power-law slope and 1σ error calculated by `gtlike` assuming the source is point power-law source
$TS_{b\bar{b}}$	TS value calculated by `gtlike` assuming the source is a point source with the $b\bar{b}$ spectrum
TS_{pwl}	TS value calculated by `gtlike` assuming the source is a point power-law source
TS_{spec}	$TS_{b\bar{b}} - TS_{pwl}$

5.4 Source Spectrum Test

As discussed in §1.3.1, the continuum γ-ray flux produced from WIMP annihilation has two main types of contributions: secondary photons from tree-level annihilation [24, 25] and additional photons from QED corrections - final state radiation (FSR) [26]. We use the hypothesis testing to distinguish a WIMP DM spectrum from a power-law spectrum. For the tree-level annihilation, the photon yields from all the quark and boson channels are quite similar as shown in Figure 1.3. The τ-channel spectrum is considerably harder. Without loss of generality, we use the energy spectrum for the $b\bar{b}$ channel as a representative tree-level annihilation spectrum for the heavy quark and boson channels. For the FSR theories, the photon yields are similar to E^{-1} spectrum, so we use a power-law with the spectral index -1.0 as an approximation of the FSR spectrum.

5.4.1 $b\bar{b}$-like Spectrum Test

The unbinned likelihood analysis treats each individual photon independently which is very important for faint sources (low statistics). Due to the low intensities of DM satellites, we decided to apply the unbinned likelihood analysis. We used TS_{spec} to distinguish between the $b\bar{b}$-like spectrum and power-law spectrum. For this application, the null hypothesis was that the candidate source was a power-law point source, and the alternative hypothesis was that it was a DM point source with a $b\bar{b}$ spectrum. We used a point source as the model because the unbinned likelihood could not handle spatial templates for extended sources. And more important, the point source hypothesis was a conservative assumption regarding the TS_{spec} value for the significance level of 0.01. The TS_{spec} distribution for a point source was wider than that for an extended source when they had the same spectrum and intensity, so the TS_{spec} value at the significance level of 0.01 for a point source was actually at a significance level < 0.01 for an extended source.

When fitting the null hypothesis, the free parameters were the background flux, the signal flux and the spectral index. When fitting the alternative hypothesis, the free parameters were the background flux, the signal flux and the DM mass. Those two hypotheses were not nested so Chernoff's theorem certainly would not apply. Therefore, we used 1000 embedded MC simulations to determine our cutoff value of TS_{spec} at the significance level of 0.01.

We used the same embedded simulation for the 10 power-law models as in §5.3.2. For each simulation, we used `gtlike` to calculate TS_{pwl} for the null hypothesis and $TS_{b\bar{b}}$ and TS_{FSR} for the alternative hypothesis, and then obtained $TS_{spec} = TS_{b\bar{b}} - TS_{pwl}$. The fitting results are in Table 5.4. The first two columns are the spectral index and the integral flux from 100 MeV to 300 GeV; the third and fourth columns are the average values of $TS_{b\bar{b}}$ and TS_{pwl} for 1000 simulations. The last column, $TS_{spec}^{0.01}$, is the cutoff values of TS_{spec} for the significance level 0.01. The $TS_{spec}^{0.01}$ varied a lot for different spectral indices and fluxes. Therefore, we also linearly interpolated them between different spectral indices and fluxes according to the values in Table 5.4.

Table 5.4 The $b\bar{b}$-like spectrum test results of the embedded MC simulation for the 10 typical power-law point source models. The last column shows the cutoff values of TS_{spec} at the 0.01 significance level.

Spectral Index	Flux (cm^{-2} s^{-1})	$< TS_{b\bar{b}} >$	$< TS_{pwl} >$	$TS_{spec}^{0.01}$
-0.9	2.0×10^{-10}	110.42	112.93	2.38
-0.9	8.0×10^{-11}	50.42	51.85	2.46
-1.5	1.1×10^{-9}	65.51	66.93	4.96
-1.5	2.0×10^{-10}	15.96	16.32	2.88
-2.0	1.2×10^{-8}	253.95	286.29	2.24
-2.0	1.2×10^{-9}	18.63	19.48	4.28
-2.5	2.1×10^{-8}	195.51	230.84	1.78
-2.5	0.5×10^{-8}	24.75	28.71	5.66
-3.0	1.7×10^{-8}	1576.00	1638.44	2.14
-3.0	1.0×10^{-8}	909.45	947.06	6.02

5.4.2 FSR Spectrum Test

After fitting the power-law hypothesis to the embedded MC simulation in last section, we compared the best-fit spectral indices and -1.0. If they were compatible within the 1σ error of fit, this sample had a spectrum consistent with the E^{-1} spectrum or the FSR spectrum. The significance level of this test, shown in Table 5.5, is also dependent on the source spectral indices and fluxes. For hard sources with spectral indices > -1.5, we can not tell whether they were the FSR spectrum. For soft sources with spectral indices < -3.0, we can distinguish them from the FSR spectrum with the significance level < 0.01. For the sources with spectral indices between -1.5 and -3.0, the significance level of the test depends on the fluxes of the sources.

Table 5.5 The significance level of the FSR spectrum test for the 10 typical power-law point source models. Since we only had 1000 simulations for each model, we could only reach the significance level down to 0.01.

Spectral Index	Flux (cm^{-2} s^{-1})	Significance Level for the FSR Spectrum Test
-0.9	2.0×10^{-10}	0.744
-0.9	8.0×10^{-11}	0.752
-1.5	1.1×10^{-9}	0.633
-1.5	2.0×10^{-10}	0.816
-2.0	1.2×10^{-8}	<0.01
-2.0	1.2×10^{-9}	0.730
-2.5	2.1×10^{-8}	<0.01
-2.5	0.5×10^{-8}	0.248
-3.0	1.7×10^{-8}	<0.01
-3.0	1.0×10^{-8}	<0.01

5.4.3 High-latitude Unassociated Extended $b\bar{b}$-like Sources in One Year of LAT Data

Using the same interpolation method in §5.3.3, we cut the TS_{spec} values for the two possibly extended unassociated sources in Table 5.3. The source 1FGL J1302.3-3255 preferred the $b\bar{b}$-like spectrum. But it cannot be a DM satellite candidate because it was a millisecond pulsar as discussed in §5.3.3.

Thus, we did not find any DM satellite with the NFW profile and the $b\bar{b}$-like spectrum for the significance level of 10^{-4} (0.01 for extension test and 0.01 for spectrum test) which corresponded to a one-sided 3.7 sigma significance.

Our spectrum test aims to remove the power-law sources; it could not distinguish the exponentially cutoff power-law spectra with the $b\bar{b}$-like spectra. Therefore, the AGN 1FGL J2325.8-4043 does not pass our test but the pulsar 1FGL J1302.3-3255 passes.

5.4.4 High-latitude Unassociated Extended FSR Sources in One Year of LAT Data

We did the FSR spectrum test to the two possibly extended unassociated sources, and they did not prefer the FSR spectrum. Thus, we did not find any DM satellite with the NFW profile and the FSR spectrum for a significance level < 0.008 (0.01 for extension test and <0.8 for spectrum test) corresponding to a one-sided 2.4σ significance at least.

5.5 Conclusion and Discussion

Based on our search algorithm, source extension test and source spectrum test, we did not find any DM satellite in one year of LAT data. Regarding this result, we can set constraints on different DM models in Chapter 6.

In the $b\bar{b}$-like spectrum test, we found that we could not distinguish the pulsar spectra from the $b\bar{b}$ spectra. The observed spectral shape of pulsars is well fitted with an exponentially cutoff power-law model of the form [73]:

$$\frac{dN}{dE} = KE_{GeV}^{-\Gamma} \exp(-\frac{E}{E_{cutoff}}) \quad (5.1)$$

in which the three parameters are the photon index at low energy Γ, the cutoff energy E_{cutoff}, and a normalization factor K (in units of $ph\ cm^{-2}\ s^{-1}\ MeV^{-1}$). In Figure 5.7, we show the best-fit exponentially cutoff power-law (with $\Gamma = 1.22$ and $E_{cutoff} = 1.8\ GeV$) of a millisecond pulsar J0030+0451 (in black) and the best-fit $b\bar{b}$ spectrum (with $M_\chi = 25\ GeV$) of this pulsar (in red). The two curves are normalized to the same value at E_{cutoff}. For $E > 200$ MeV, the two curves are very similar. It is not surprising that our spectrum test can not distinguish those two spectral models.

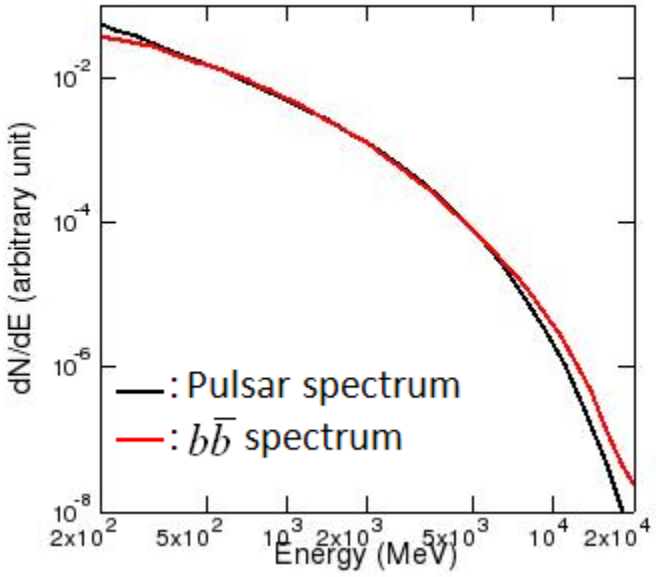

Figure 5.7 The best-fit exponentially cutoff power-law (with $\Gamma = 1.22$ and $E_{cutoff} = 1.8\ GeV$) of a millisecond pulsar J0030+0451 (in black) and the best-fit $b\bar{b}$ spectrum (with $M_\chi = 25\ GeV$) of this pulsar (in red).

In order to study if the $b\bar{b}$-like spectrum test can reject pulsars, we did the spectrum test with all the *Fermi* LAT collaboration observed 25 high-latitude ($|b| > 20^o$) pulsars, including 14 pulsars identified in the 1FGL catalog and the 11 pulsars unidentified in the 1FGL catalog but identified by the follow-up observations of radio telescope detections. 24 pulsars pass the spectrum test, preferring $b\bar{b}$-like spectra to power-law spectra. The best-fit DM mass of the 25 pulsars is shown in Figure 5.8. Although the statistics are limited, the distribution shows a peak around 25 GeV with most pulsars having $M_\chi < 60\ GeV$. Thus, if the true mass of DM is < 60 GeV, the unidentified high-latitude pulsars present a big confusion for the spectral search for DM satellites, and so the extension test is necessary and important. If the DM mass is > 60 GeV, the pulsar contamination will be much less (~ 1/25) given the current one-year *Fermi* LAT pulsar sample.

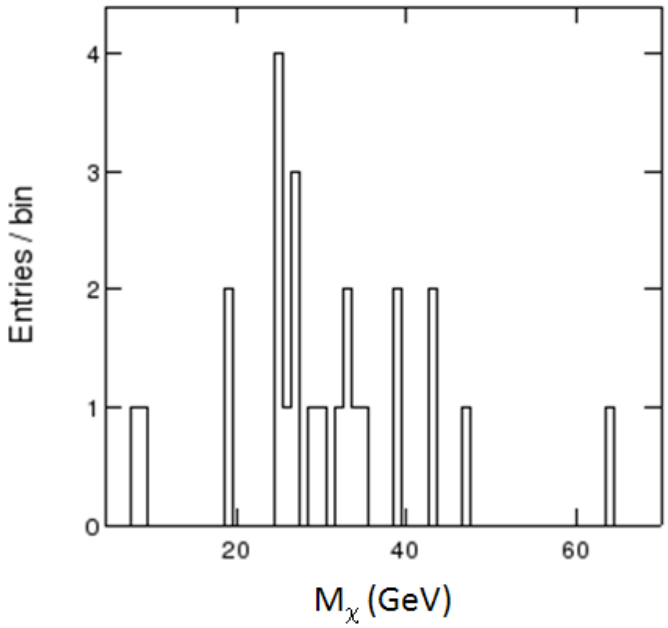

Figure 5.8 Best-fit DM mass of the 25 high-latitude ($|b| > 20^o$) pulsars.

CHAPTER 6
CONSTRAINTS ON WIMP MODELS

6.1 Predicted Number of Observed Satellites in the VL2 Simulation

The overall efficiency of our analysis method (defined as the fraction of the true DM satellites that can be detected by the LAT and pass the source extension test and the source spectrum test) depends on the spectrum shape, the flux and the extension of the source. In this thesis, we discussed five interesting WIMP models:

- Generic WIMP, $b\bar{b}$ channel, WIMP mass $M_\chi = 100\ GeV$, cross-section $< \sigma v >= 3 \times 10^{-26}\ cm^3 s^{-1}$.
- Low mass WIMP, $b\bar{b}$ channel, $M_\chi = 10\ GeV$, $< \sigma v >= 3 \times 10^{-26}\ cm^3 s^{-1}$.
- FSR model proposed to fit the ATIC, PAMELA and *Fermi* e^+e^- data, $\mu^+\mu^-$ channel, $M_\chi = 300\ GeV$, $< \sigma v >= 3.8 \times 10^{-24}\ cm^3 s^{-1}$.
- Non-thermal Wino LSP DM [58], W^+W^- channel, $M_\chi = 177.5\ GeV$, $< \sigma v >= 2.5 \times 10^{-24}\ cm^3 s^{-1}$.
- DM model proposed to fit the *Fermi* γ-ray excess from the Galactic center [59], $\tau^+\tau^-$ channel, $m_\chi = 7\ GeV$, $< \sigma v >= 1.5 \times 10^{-26}\ cm^3 s^{-1}$.

Based on the J values of the satellites for the 14 realizations of the VL2 satellites in Figure 5.6, we can bin the number of satellites in source extension and flux. The lowest flux of the 385 unassociated sources is about $5.0 \times 10^{-11}\ cm^{-2} s^{-1}$, and the minimum source extension that could be resolved by the LAT is about 0.5^o. Therefore,

we are only interested in calculating the efficiency for the sources with fluxes larger than $5.0 \times 10^{-11}\ cm^{-2}s^{-1}$ and extensions larger than 0.5^{o}.

We used the average number of satellites per realization and the standard deviation for the 14 realizations to estimate the fluctuations due to the different Earth's positions. In Table 6.1, we list the average number of satellites and the standard deviation for each flux and extension bin. The minimum flux (integrated from 200 MeV to 300 GeV) of the bin is in the first row and the minimum extension of the bin is in the first column.

We used the same embedded MC simulation technique described in §5.3.2 for the five WIMP models for each flux and extension bin with non-zero satellites. Since we used the union of the 1FGL unassociated sources and the non-1FGL sources found by `sourcelike` as the number of unassociated sources which are DM satellite candidates, five different search methods were actually applied. Different methods gave different detection efficiency, so it was not easy to calculate the efficiency of the union of five source search algorithms. Therefore, we decided to use the fraction of the MC satellites with TS_sourcelike > 24 to determine the detection efficiency because `sourcelike` would detect sources with TS > 24 as described in §5.2.1. Then we obtained the overall efficiency of our search for DM satellites by multiplying this detection efficiency with the efficiency for the satellites passing the extension test and the spectrum test.

Due to the limited computer time, we stopped calculating the overall efficiency if it was below 5%. The overall efficiency of the tests is listed in parentheses in Table 6.1.

Table 6.1 The average number of satellites per realization and the standard deviation and the overall efficiency of our analysis method for each flux and extension bin for the five WIMP models for the 14 realizations of the VL2 satellites. The overall efficiency is given in parentheses.

$b\bar{b}$ channel, 100 GeV, $3 \times 10^{-26}\ cm^3 s^{-1}$

Flux (10^{-8} cm^{-2} s^{-1}) \ R_0 (^{o})	0.005	0.01	0.02	0.05	0.1	0.2	0.5	1.0	2.0	5.0
0.5	1.71 $\pm$ 1.16 (< 5%)	2.50 $\pm$ 1.05 (< 5%)	1.50 $\pm$ 0.63 (< 5%)	0	0	0	0	0	0	0
1.0	1.00 $\pm$ 0.65 (< 5%)	0.29 $\pm$ 0.59 (< 5%)	1.07 $\pm$ 0.96 (< 5%)	0.71 $\pm$ 0.45 (< 5%)	0	0	0	0	0	0
2.0	0	0	0	0.29 $\pm$ 0.45 (< 5%)	0.29 $\pm$ 0.45 (< 5%)	0.07 $\pm$ 0.26 (< 5%)	0	0.07 $\pm$ 0.26 (83.0%)	0	0

$b\bar{b}$ channel, 10 GeV, $3 \times 10^{-26}\ cm^3 s^{-1}$

Flux (10^{-8} cm^{-2} s^{-1}) \ R_0 (^{o})	0.005	0.01	0.02	0.05	0.1	0.2	0.57	1.0	2.0	5.0
0.5	1.57 $\pm$ 1.12 (< 5%)	1.50 $\pm$ 1.18 (< 5%)	6.79 $\pm$ 2.11 (< 5%)	2.86 $\pm$ 1.19 (< 5%)	2.07 $\pm$ 1.22 (< 5%)	2.71 $\pm$ 1.28 (< 5%)	1.50 $\pm$ 0.98 (< 5%)	0.36 $\pm$ 0.48 (< 5%)	0	0
1.0	1.00 $\pm$ 0.00 (< 5%)	0	0	0.21 $\pm$ 0.56 (< 5%)	0.93 $\pm$ 0.59 (< 5%)	0.64 $\pm$ 0.72 (< 5%)	0.86 $\pm$ 0.74 (< 5%)	1.0 $\pm$ 0.53 (< 5%)	0	0
2.0	0	0	0	0	0	0	0	1.43 $\pm$ 0.35 (< 5%)	0.36 $\pm$ 0.48 (28.1%)	0.21 $\pm$ 0.56 (91.0%)

FSR model ($\mu^+\mu^-$ channel), 300 GeV, $3.8 \times 10^{-24}\ cm^3 s^{-1}$

Flux (10^{-8} cm^{-2} s^{-1}) \ R_0 (^{o})	0.005	0.01	0.02	0.05	0.1	0.2	0.5	1.0	2.0	5.0
0.5	1.86 ± 1.06 (<5%)	0.79 ± 0.67 (<5%)	0	0	0	0	0	0	0	0
1.0	0.43 ± 0.62 (< 5%)	0.93 ± 0.88 (< 5%)	0.57 ± 0.49 (< 5%)	0	0	0	0	0	0	0
2.0	0	0	0.36 ± 0.48 (< 5%)	0.29 ± 0.59 (< 5%)	0	0	0.07 ± 0.26 (45.7%)	0	0	0

W^+W^- channel, 177.5 GeV, $2.5 \times 10^{-24}\ cm^3 s^{-1}$

Flux (10^{-8} cm^{-2} s^{-1}) \ R_0 (^{o})	0.005	0.01	0.02	0.05	0.1	0.2	0.5	1.0	2.0	5.0
0.5	1.71 ± 0.88 (< 5%)	3.00 ± 1.07 (< 5%)	6.21 ± 1.42 (< 5%)	1.64 ± 0.81 (< 5%)	2.29 ± 1.53 (< 5%)	2.64 ± 1.11 (< 5%)	1.36 ± 0.72 (38.5%)	0.07 ± 0.26 (93.0%)	0	0
1.0	1.00 ± 0.00 (< 5%)	0	0	0.43 ± 0.62 (< 5%)	1.00 ± 0.84 (< 5%)	0.50 ± 0.73 (5.0%)	0.86 ± 0.83 (51.5%)	0.86 ± 0.52 (90.0%)	0	0
2.0	0	0	0	0	0	0	0	0.21 ± 0.41 (80.8%)	0.36 ± 0.61 (98.0%)	0.14 ± 0.35 (100.0%)

$\tau^+\tau^-$ channel, 7 GeV, $1.5 \times 10^{-26}\ cm^3 s^{-1}$

Flux (10^{-8} cm^{-2} s^{-1}) \ R_0 (^{o})	0.005	0.01	0.02	0.05	0.1	0.2	0.5	1.0	2.0	5.0
0.5	5.21 $\pm$ 2.21 (< 5%)	3.57 $\pm$ 1.40 (< 5%)	2.50 $\pm$ 1.40 (< 5%)	2.14 $\pm$ 1.12 (< 5%)	1.50 $\pm$ 0.98 (< 5%)	0.79 $\pm$ 0.67 (< 5%)	0	0	0	0
1.0	0	1.43 $\pm$ 0.35 (< 5%)	1.14 $\pm$ 0.83 (< 5%)	0.50 $\pm$ 0.63 (< 5%)	0.43 $\pm$ 0.62 (< 5%)	1.43 $\pm$ 0.82 (< 5%)	0	0	0	0
2.0	0	0	0	0	0	1.43 $\pm$ 0.35 (< 5%)	0.21 $\pm$ 0.41 (< 5%)	0.29 $\pm$ 0.59 (55.0%)	0	0.07 $\pm$ 0.26 (99.5%)

Table 6.2 Predicted number of observed DM satellites, N_{pred}, for the five WIMP models for each of the 14 realizations of the VL2 satellites. The Earth position in each realization is given in Table 1.1.

Realization	N_{pred} ($b\bar{b}$; 100 GeV; $3 \times 10^{-26}\ cm^3 s^{-1}$)	N_{pred} ($b\bar{b}$; 10 GeV; $3 \times 10^{-26}\ cm^3 s^{-1}$)	N_{pred} ($\mu^+\mu^-$; 300 GeV; $3.8 \times 10^{-24}\ cm^3 s^{-1}$)	N_{pred} (W^+W^-; 177.5 GeV; $2.5 \times 10^{-24}\ cm^3 s^{-1}$)	N_{pred} ($\tau^+\tau^-$; 7 GeV; $1.5 \times 10^{-26}\ cm^3 s^{-1}$)
0	0	0	0	1.285	0
1	0	1.191	0	4.165	1.1
2	0	0	0	2.315	0
3	0	0.281	0	3.73	0.55
4	0	0.281	0	4.295	0
5	0	0	0	1.708	0
6	0	0	0	2.235	0
7	0	0.281	0	2.638	0
8	0	0	0	1.77	0
9	0	0	0	2.193	0
10	0	0	0	1.285	0
11	0.83	2.101	0.457	4.245	1.545
12	0	0	0	1.85	0
13	0	0	0	1.285	0

The predicted number of observed DM satellites based on our analysis method in each bin was the multiplication of the number of the satellites and the efficiency in that bin. For each WIMP model, we summed up all the bins with efficiencies > 5% in Table 6.1 and obtained the predicted number of observed DM satellites, N_{pred}, for each realization. In Table 6.2, we list N_{pred} for the five WIMP models for each realization. In Table 6.3, we calculate the average number and the standard deviation of N_{pred} for the 14 realizations.

Table 6.3 The average and the standard deviation of N_{pred} for the 14 realizations of the VL2 satellites.

WIMP Model	N_{pred}^{avg}	Standard Deviation
$b\bar{b}$; 100 GeV; 3×10^{-26} $cm^3 s^{-1}$	0.06	0.21
$b\bar{b}$; 10 GeV; 3×10^{-26} $cm^3 s^{-1}$	0.30	0.59
$\mu^+\mu^-$; 300 GeV; 3.8×10^{-24} $cm^3 s^{-1}$	0.03	0.12
W^+W^-; 177.5 GeV; 2.5×10^{-24} $cm^3 s^{-1}$	2.50	1.09
$\tau^+\tau^-$; 7 GeV; 1.5×10^{-26} $cm^3 s^{-1}$	0.23	0.48

6.2 Discussion

The probability to find N DM satellites for a given predicted number of observed DM satellites, λ, is expressed as a Poisson distribution,

$$P(N|\lambda) = \frac{\lambda^N}{N!} e^{-\lambda} \tag{6.1}$$

For the W^+W^- model, $\lambda = 2.50$, so the probability to find one or more DM satellites is

$$P(N \geq 1|\lambda = 2.50) = 1 - P(N = 0|\lambda = 2.50) = 92\% \tag{6.2}$$

Thus, the W^+W^- model can be ruled out at a confidence level of 92%.

In addition, if a WIMP model gives $\lambda = 3.00$, then this model can be ruled out at a confidence level of 95%. For a 100 GeV WIMP annihilating into the $b\bar{b}$ channel, the

cross section $< \sigma v >= 1.2 \times 10^{-24}\ cm^3 s^{-1}$ corresponds to $= 3.23 \pm 1.09$. Therefore, the 95% upper limit of the cross section for a 100 GeV WIMP annihilating into the $b\bar{b}$ channel is $1.2 \times 10^{-24}\ cm^3 s^{-1}$. When we use a higher significance level, 0.005, for the extension test and the spectrum test, the 95% upper limit of the cross section is unchanged within 8%. Therefore, our method for deriving the upper limit is quite robust.

In this chapter, we assume that the DM satellites in our galaxy are distributed as the VL2 simulation without any boost factor. We use the NFW profile for all the satellites; however this is a conservative assumption since the VL2 reported a steeper inner density profile [15]. Therefore, the NFW assumption without boost factor underestimates the fluxes of the VL2 satellites, and as a result, generally underestimates the number of observed satellites.

Figure 5.5 shows that most VL2 satellites are point sources with the extension < 0.5^o. If we do not require the extension test, we should predict more observed satellites (including point and extended sources). However, there will also be more false detections because many unassociated sources, e.g. unidentified pulsars and blazars, have non-power-law spectra. Thus, we have to use a higher significance level for the spectrum test to remove the false detections. In that case, the predicted number of the observed satellites will depend on the significance level we choose, and the predicted number may be larger or smaller.

In the future, our analysis method for the search for unknown DM satellites can be used with more LAT data. However, more data means more unassociated sources, so we have to push the significance level of the tests higher to avoid false detections. In that situation, many more MC simulations will be needed, and computer time will be a critical issue.

APPENDIX A
EXTRAPOLATION OF THE VIA LACTEA II SATELLITE MASS FUNCTION [a]

A.1 Via Lactea II Satellites

The Via Lactea II (VL2) simulation [15] employs over one billion 4,100 $M_\odot$ particles to model the formation and evolution of a $M_{200} = 1.93 \times 10^{12}\ M_\odot$ Milky-Way-size DM halo and its substructure. It resolves over 50,000 satellites within the host's $r_{200} = 402\ kpc$ (the radius enclosing an average density 200 times the cosmological mean matter density), and 20,045 of these satellites (including the main halo) are publicly available. Each satellite has associated with it a relative position, velocity, tidal mass, maximum circular velocity (V_{max}), and a radius of maximum circular velocity ($R_{V_{max}}$).

We create *N* realizations of the satellite distributed corresponding to *N* viewpoints on the 8.5 *kpc* solar sphere. While the detailed distribution of DM within the VL2 satellites is not publicly available, we can uniquely define an NFW profile for each satellite using the relations [57]:

$$r_s = \frac{R_{Vmax}}{2.163} \tag{A.1}$$

$$\rho_s = \frac{4.625}{4\pi G}\left(\frac{V_{max}}{r_s}\right)^2 \tag{A.2}$$

To deal with the divergent nature of the NFW profile, we fix a hard core density ($\rho_c = \rho(r_c)$) at radii $r < r_c = 10^{-5}\ pc$. Thus, the final form of our density distribution is:

[a]: Acknowledge Alex Drlica-Wagner and Louie Strigari for their work on this section.

$$\rho = \begin{cases} \frac{\rho_s}{\frac{r}{r_s}(1+\frac{r}{r_s})^2} & for\ r < r_c \\ \rho_c & for\ r < r_c \end{cases} \quad (A.3)$$

This is a somewhat conservative assumption, since current N-body simulations suggest that the DM profiles of satellites are more peaked [15].

The γ-ray flux from annihilating DM in a satellite is expressed as:

$$\Phi_\gamma = J \times \Phi^{SUSY}$$

$$J = \int d\Omega \int_{l.o.s} \rho(l)^2 dl$$

$$\Phi^{SUSY} = \frac{1}{4\pi} \frac{<\sigma v>}{2M_\chi^2} \int \sum_f \frac{dN_f}{dE} B_f dE \quad (3.1)$$

where $< \sigma v >$ is the total mean annihilation cross-section σ multiplied by the relative velocity of the DM particles, M_χ is the mass of the DM particle, $\rho(l)$ is the density profile of the DM satellite. The astrophysical factor, *J*, is the line-of-sight (l.o.s) integral of the DM density distribution. For satellites at large distances, this can be approximated as [74]:

$$J \approx \frac{1}{D^2} \int_V \rho(r)^2 dV \quad (A.4)$$

where *D* is the distance of the satellite from the Earth, and the integration is performed over the satellite volume inside the tidal radius.

A.2 Extrapolation of the Satellite Mass Function

The satellite mass resolution of the VL2 simulation is $\sim 10^5\ M_\odot$. We planned to extrapolate the satellite mass function to lower mass.

The first step in characterizing low-mass satellites is to determine the local number and distribution. We begin by fitting a power-law to the mass function of satellites with mass greater than $10^6\ M_\odot$ within 50 *kpc* of the galactic center. The best fit index of this power-law is -1.86, a value that agrees well with values in the literature [75, 76]. By extrapolating this mass function below the resolution limit of VL2, we can predict

the number of satellites with a given mass found within 50 *kpc* of the galactic center, as shown in Figure A.1. Assuming that there is negligible mass-dependence in the spatial distribution of satellites, we model the radial distribution of satellites with [4]:

$$N(x) \propto \frac{20x^{2.9}}{1+19x^{1.9}} \tag{A.5}$$

where *N* is the cumulative number of satellites interior to *x*, and $x = r/r_{200}$. The distribution of *N* as a function of the satellite distance to the galactic center is shown in Figure A.2.

In order to implement the NFW profile in Eq (A.1) and Eq (A.2), it is necessary to develop a relationship between tidal mass, maximum circular velocity and radius of maximum circular velocity. Using the VL2 satellites with mass $> 10^6\ M_\odot$ within 50 *kpc* of the galactic center, we find that $V_{max} \propto M^{0.30}$ with a log-Gaussian scatter of $\sigma = 0.063$, as shown in Figure A.3. Additionally, we find that $R_{V_{max}} \propto M^{0.39}$ with a log-Gaussian scatter of $\sigma = 0.136$, as shown in Figure A.4. Extrapolating these relationships to lower masses, we define NFW profiles for satellites under the resolution limit of VL2. Simulation of theses low-mass halos then proceeds identically to those halos native to VL2.

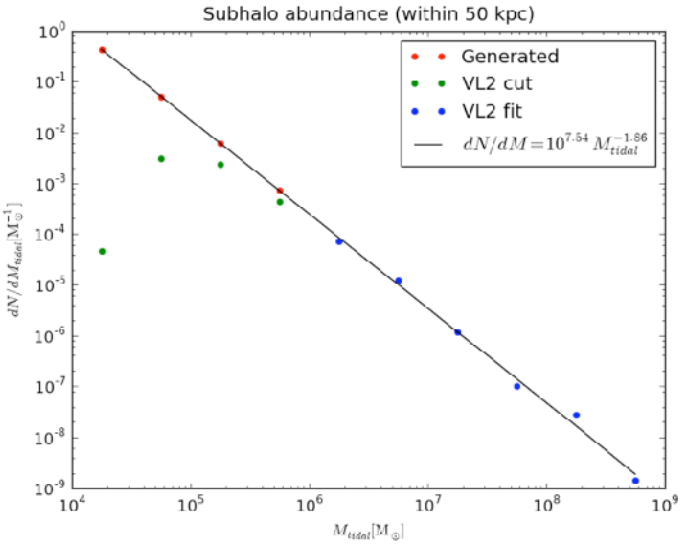

Figure A.1 Mass function of the VL2 satellites within *50* kpc of the galactic center. The original VL2 satellites with mass $> 10^6\ M_\odot$ (in blue) are used to fit with a power-law function; the original VL2 satellites with mass $< 10^6\ M_\odot$ (in green) are too close to the mass resolution to follow the power-law mass function; low-mass satellites are generated (in red) by extrapolating the power-law mass function fitted using the satellites with mass $> 10^6\ M_\odot$.

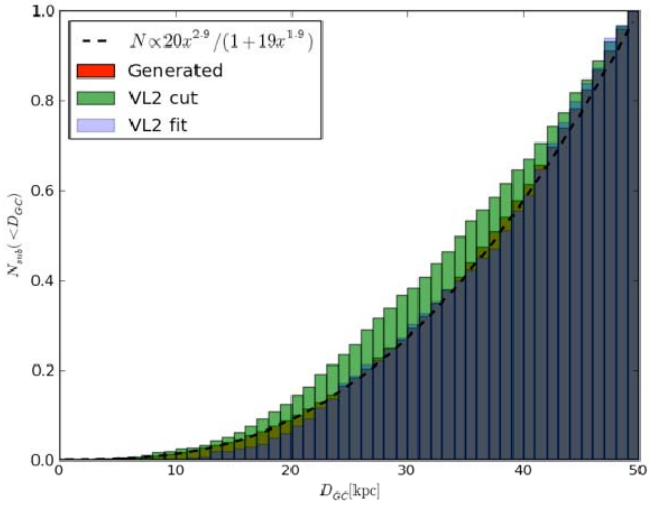

Figure A.2 Cumulative number of satellites as a function of the satellite distance to the galactic center. The original VL2 satellites with mass $> 10^6\ M_\odot$ are in blue; the original VL2 satellites with mass $< 10^6\ M_\odot$ are in green; low-mass satellites are generated (in red) by extrapolating the power-law mass function. The dash line is Eq (A.5).

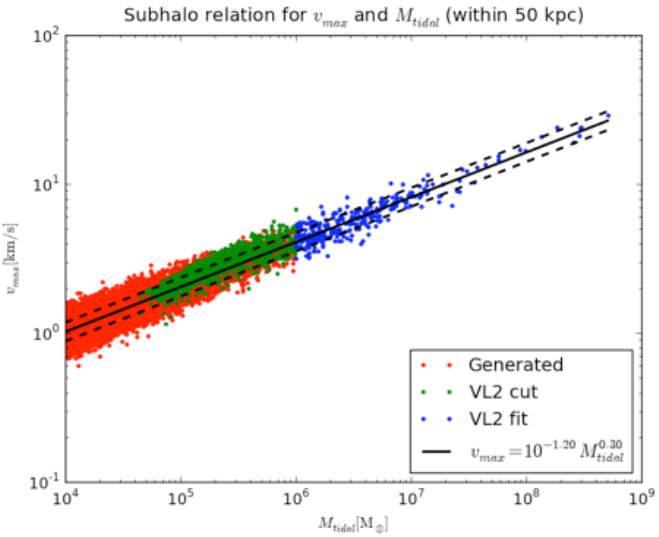

Figure A.3 Relation between tidal mass and maximum circular velocity. The original VL2 satellites with mass $> 10^6\ M_\odot$ are in blue; the original VL2 satellites with mass $< 10^6\ M_\odot$ are in green; low-mass satellites are generated (in red) by extrapolating the power-law mass function. The solid line is the fitted power-law function and the dash lines show the log-Gaussian scatter.

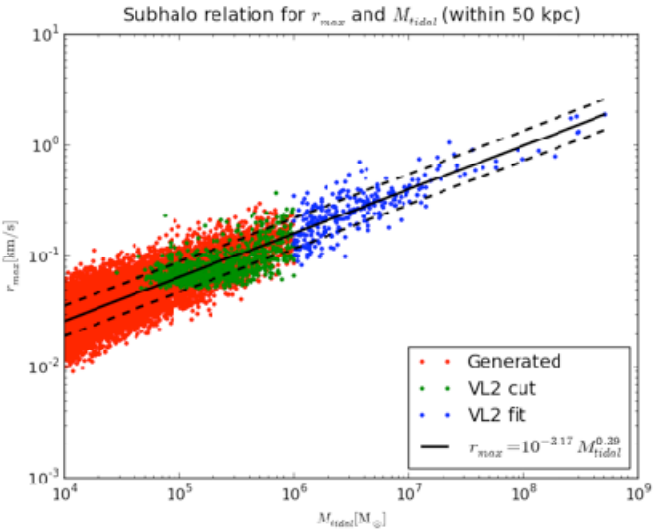

Figure A.4 Relation between tidal mass and radius of maximum circular velocity. The original VL2 satellites with mass $> 10^6\ M_\odot$ are in blue; the original VL2 satellites with mass $< 10^6\ M_\odot$ are in green; low-mass satellites are generated (in red) by extrapolating the power-law mass function. The solid line is the fitted power-law function and the dash lines show the log-Gaussian scatter.

A.3 Flux Cut for Low-mass Satellites

While the nature of the satellite mass function means that the number density of satellites increases with decreasing mass, the flux from satellites will not necessarily follow this trend. Using the relations derived in the last section, it is possible to compute how the astrophysical factor in the satellite flux depends on satellite mass.

For satellites at large distances from the Earth, the astrophysical factor in the flux is described by:

$$J \propto \frac{r_s^3 \rho_s^2}{D^2} \tag{A.6}$$

Using the relations that $r_s \propto M^{0.39}$ and $\rho_s \propto M^{-0.18}$, it is found that:

$$J \propto \frac{M^{0.81}}{D^2} \tag{A.7}$$

which can be compared to the relation $J \propto \frac{M^{0.87}}{D^2}$ in [77]. Using this extension, it is possible to directly compare the astrophysical component of the flux for different halos based on their mass and distance from Earth. The choice of particle physics model merely scales all satellites by the same constant factor.

In Figure A.5, the yellow, red and black stars indicate the distance of Draco dSph while its mass is $10^7\ M_\odot$, $10^8\ M_\odot$ and $10^9\ M_\odot$. The yellow, red and black lines show $J \propto \frac{M^{0.81}}{D^2} = constant$. Based on Eq (A.7), all the satellites on the same line have the same J value which is the J value of Draco dSph. The mass of Draco derived from the optical observation is > $10^7\ M_\odot$, so the cut based on the yellow line is actually conservative. Since all the satellites above the yellow line have the J values less than that of Draco and Draco is not detected by the LAT so far, the satellites above the yellow line are definitely not detectable by the LAT for one year of observation either. Therefore, while generating low-mass satellites, we will firstly cut mass and distance based on the yellow line to save computer time.

It can be seen in Figure A.5, that while the total number of satellites increases with decreasing mass, these low-mass satellites tend to have a decreasing J value. This means that low-mass satellites, while dominating the local volume in number, are not the dominant contributor to flux. For low-mass satellites to dominate the γ-ray signal from satellites, it would be necessary to either increase the concentration for low-mass satellites, or decrease the slope of the mass function.

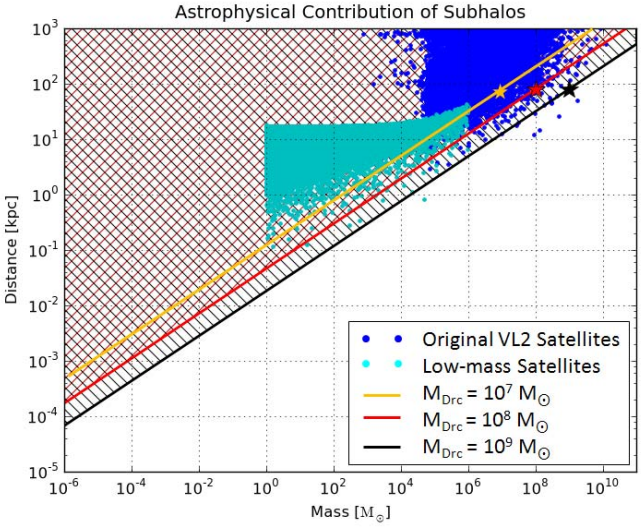

Figure A.5 Distribution of satellite mass and distance for the original VL2 satellites (in blue) and the low-mass satellites by extending the mass function (in cyan). The yellow, red and black stars indicate the distance of Draco dSph while its mass is $10^7\ M_\odot$, $10^8\ M_\odot$ and $10^9\ M_\odot$. The yellow, red and black lines show $J \propto \frac{M^{0.81}}{D^2} = constant$.

APPENDIX B

EXTRAPLOATION OF THE LAT GALACTIC DIFFUSE MODEL

Since our analysis with real data is done in the energy range 200 MeV – 300 GeV, we need MC data also in this energy range while studying the LAT sensitivity to DM satellites, the spurious sources found by `sourcelike` and the TS distribution in the source extension test and the source spectrum test. However, the Galactic diffuse model "gll_iem_v02.fit" [60] is a mapcube from 50 MeV to 100 GeV. We had to extrapolate this model up to 300 GeV.

Yvonne Edmond, a fellow Stanford Physics graduate student and a LAT collaborator, studied on the diffuse background using two years of LAT data. Her study showed the total diffuse background followed a power-law very well for > 20 GeV, as shown in Figure B.1. The background below 20 GeV could be fitted with a power-law with a different spectral index while the fit was not good. Therefore, for each Galactic coordinate *(l, b)* bin, we fitted the Galactic diffuse model in the energy range 20 – 100 GeV with a power-law and extrapolated it to higher energy. The fit was done in log-log space using the method "least squares".

Figure B.2 is an example of the bin (l, b) = (-179.75^{o}, -89.75^{o}). The data points are from the standard model which is obviously not a power-law at low energy; the red line is a power-law fitted to the model in the full energy range 50 MeV – 100 GeV; the blue line is a power-law fitted to the model in the energy range 20 – 100 GeV. We used the fit in blue to do the extrapolation.

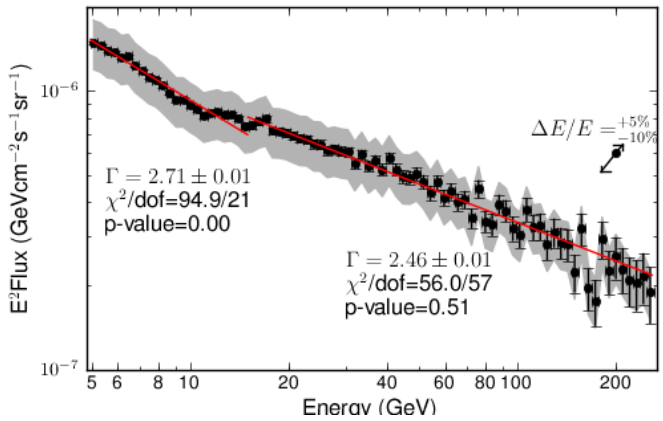

Figure B.1 Total diffuse background of 2 years of LAT data. Grey band indicates systematic errors. The fit in 20 – 240 GeV is very good with p-value = 0.51 and the fit in 5 – 20 GeV is poor with p-value ~ 0. (from Edmond's presentation)

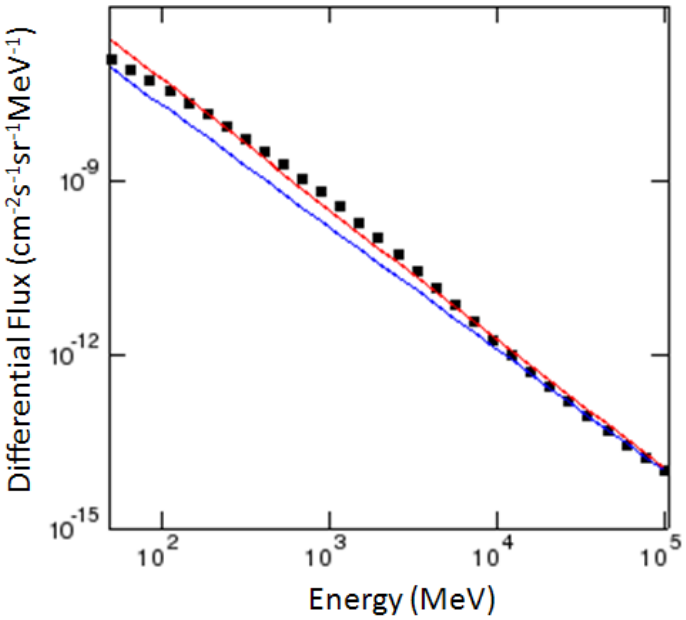

Figure B.2 Power-law fit for the bin *(l, b) = (-179.75°, -89.75°)*. The data points are from the standard model; the red line is a power-law fitted to the model in the full energy range 50 MeV – 100 GeV; the blue line is a power-law fitted to the model in the energy range 20 – 100 GeV. The blue line is used to extrapolate to higher energy.

APPENDIX C
LIKELIHOOD FUNCTION IN GTLIKE [a] AND SOURCELIKE [b]

The maximum likelihood analysis has been successfully used in the analysis of γ-ray data and it has also a central role in the LAT data analysis.

C.1 Gtlike

Gtlike uses the likelihood to find the best fit model parameters including the source's spectrum, spatial distribution and position. It can perform unbinned and binned likelihood analysis. Unbinned likelihood analysis is the preferred method for spectral fitting of the LAT data. However, a binned analysis is provided for cases where the unbinned analysis cannot be used. For example, the computer memory required for the likelihood calculation scales with number of photons and number of sources. This memory usage becomes excessive for long observations of complex regions.

Before gtlike analysis, we need to select Region of Interest (ROI) and Source Region (SR). Assume that we are analyzing the spectrum of a single source. Because of the large PSF at low energies (e.g., 68% of the counts will be within 3.5^{o} at 100 MeV), we want to use the counts within a region around the source. Nearby sources will contribute counts to this region, and we want to model them, i.e., to model a single source we are forced to model a handful of sources. Therefore, we need to include counts from an even larger region. For the greatest accuracy possible in

[a]: Acknowledge the *Fermi* Collaboration for gtlike and Science Tools.
[b]: Acknowledge Toby Burnet and Josh Lande for their work on sourcelike. This is not a supported code under Science Tools.

modeling a single source, we should model the entire sky, but this is not usually feasible and, in reality, the influence of sources a very great distance away from the source will be greatly attenuated. Thus, we include sources from a large SR and counts from a smaller ROI.

The total source model is the sum of contributions from individual point-like and diffuse sources:

$$S(\varepsilon, \hat{p}) = \sum_i S_i(\varepsilon, \hat{p}) \quad \text{(C.1)}$$

where ε is the true energy of the photon and $\hat{p}$ is the true direction on the sky. We assume spatial and spectral parts factor and that the sources are time-steady:

$$S_i(\varepsilon, \hat{p}) = s_i(\varepsilon)\widetilde{S_i}(\hat{p}) \quad \text{(C.2)}$$

For a point source i,

$$S_i(\varepsilon, \hat{p}) = s_i(\varepsilon)\delta(\hat{p} - \hat{p}_i) \quad \text{(C.3)}$$

Typically, only the spectral part of the source models is fit, with relatively simple spectral models, e.g., power-laws:

$$s(\varepsilon) = N_0 \varepsilon^{-\Gamma} \quad \text{(C.4)}$$

The instrument response is typically factored into three components:

$$R(\varepsilon', \hat{p}'; \varepsilon, \hat{p}, t) = A(\varepsilon, \hat{p}, t)P(\hat{p}'; \varepsilon, \hat{p}, t)D(\varepsilon'; \varepsilon, \hat{p}, t) \quad \text{(C.5)}$$

Here ε' and $\hat{p}'$ are the measured energy and direction of the photon respectively. $P(\hat{p}'; \varepsilon, \hat{p}, t)$ is the PSF; and $D(\varepsilon'; \varepsilon, \hat{p}, t)$ is the energy dispersion; both functions are PDFs. The effective area $A(\varepsilon, \hat{p}, t)$ is the cross-section of the LAT for detecting an incident photon with $(\varepsilon, \hat{p})$ at a time *t*. The time-dependence of each factor is required since $\hat{p}$ is in sky coordinates, and the LAT pointing is not fixed. The expected distribution of detected counts is

$$M(\varepsilon', \hat{p}', t) = \int_{SR} d\varepsilon d\hat{p} S(\varepsilon, \hat{p}) R(\varepsilon', \hat{p}'; \varepsilon, \hat{p}, t) \quad \text{(C.6)}$$

$$= \sum_i \left[\int_{SR} d\varepsilon d\hat{p} S_i(\varepsilon, \hat{p}) R(\varepsilon', \hat{p}'; \varepsilon, \hat{p}, t)\right] \quad \text{(C.7)}$$

$$= \sum_i M_i(\varepsilon', \hat{p}', t) \quad \text{(C.8)}$$

$\int_{SR} d\varepsilon d\hat{p}$ is the integral over the SR, which in principle, covers the whole sky and all energies.

For data binned in $(\varepsilon', \hat{p}')$, the Poisson likelihood is

$$L = \prod_j \frac{e^{-\theta_j} \theta_j^{n_j}}{n_j!} \tag{C.9}$$

Of course, what is actually used is the natural logarithm of the likelihood:

$$\ln L = -\sum_j \theta_j + \sum_j n_j \ln \theta_j - \sum_j \ln n_j! \tag{C.10}$$

Here n_j is the measured number of events in the bin *j* and θ_j is the predicted number of events lying in that bin given the model:

$$\theta_j = \int dt \int_j d\varepsilon' d\hat{p}' M(\varepsilon', \hat{p}', t) \tag{C.11}$$

Here $\int_j d\varepsilon' d\hat{p}'$ indicates the integral over the bin *j*, and the time integral is over the duration of the observation.

The log-likelihood for the **binned** case (dropping the terms independent on source models):

$$\ln L = -\sum_j \theta_j + \sum_j n_j \ln \theta_j = \sum_j n_j \ln \theta_j - N_{pred} \tag{C.12}$$

The predicted number of events within a given ROI is

$$N_{pred} = \int dt \int_{\varepsilon_{min}}^{\varepsilon_{min}} d\varepsilon' \int_{\Omega_{ROI}} d\hat{p}' M(\varepsilon', \hat{p}', t) \tag{C.13}$$

In the limit of very small bins, where we have n_j = 0 or 1 event,

$$\theta_j = \delta\varepsilon' \delta\hat{p}' \delta t M(\varepsilon_j', \hat{p}_j', t_j) \tag{C.14}$$

Here *j* labels each detected photon, and we obtain the expression for our **unbinned** likelihood calculation:

$$\ln L = \sum_j \ln M(\varepsilon_j', \hat{p}_j', t_j) - N_{pred} \tag{C.15}$$

Writing the first term explicitly in Eq (C.15):

$$\sum_j \ln(\sum_i \int d\varepsilon s_i(\varepsilon) \int d\hat{p}\, \widetilde{S}_\iota(\hat{p}) A(\varepsilon, \hat{p}, t_j) P(\hat{p}_j'; \varepsilon, \hat{p}, t_j) D(\varepsilon_j'; \varepsilon, \hat{p}, t_j)) \tag{C.16}$$

For a point source at location $\hat{p}_j$,

$$\sum_j \ln(\sum_i \int d\varepsilon s_i(\varepsilon) A(\varepsilon, \hat{p}_j, t_j) P(\hat{p}_j'; \varepsilon, \hat{p}_j, t_j) D(\varepsilon_j'; \varepsilon, \hat{p}_j, t_j)) \tag{C.17}$$

For every evaluation of the log-likelihood, the integral over the energy dispersion must be computed for every event *j* and every source *i*. The situation is even worse for

diffuse sources since the integral over $\hat{p}$ must also be folded in. The current implementation neglects this integral, simplifying the calculation to

$$\sum_j \ln(\sum_i s_i(\varepsilon'_j) A(\varepsilon'_j, \hat{p}_j, t_j) P(\hat{p}'_j; \varepsilon'_j, \hat{p}_j, t_j)) \quad \text{(C.18)}$$

This speeds things up enormously. Making the same approximation for the diffuse sources,

$$\sum_j \ln(\sum_i s_i(\varepsilon'_j) [\int d\hat{p} \widetilde{S}_i(\hat{p}) A(\varepsilon'_j, \hat{p}_j, t_j) P(\hat{p}'_j; \varepsilon'_j, \hat{p}_j, t_j)]) \quad \text{(C.19)}$$

The factor in square brackets can be pre-computed for each event and stored as a single number. These are the diffuse response quantities produced by `gtdiffrsp`.

C.2 `Sourcelike`

`Sourcelike` uses binned likelihood. Data is binned in position and energy, and the fitting is done independently in each energy band. The likelihood function is defined as the product of the log-likelihood for each HEALPix spatial bin j for a particular energy band, written as Eq (C.10):

$$\ln L = -\sum_j \theta_j + \sum_j n_j \ln \theta_j - \sum_j \ln n_j! \quad \text{(C.10)}$$

Here n_j is the measured number of photons in the bin and θ_j is the predicted number of photons in the bin given the spatial model. In a given energy band ε', for each spatial bin j, n_j is read from the FT1 file and

$$\theta_j(\varepsilon') = N(\varepsilon') \times PDF_j(model, \varepsilon') \times \Omega_j(\varepsilon') \quad \text{(C.20)}$$

where $N(\varepsilon')$ is the total number of photons in the ROI, $PDF_j(model, \varepsilon')$ is the PDF of the photon spatial distribution in the given bin for the given model and $\Omega_i(\varepsilon')$ is the solid angle of such bin. $PDF_j(model, \varepsilon')$ is normalized to 1 in the ROI, so that $\sum_j \theta_j = N$. Since the photons are binned in HEALPix, $\Omega_j = \Omega$ is a constant.

`Sourcelike` assumes that all the photons can be attributed to either the source or the background so

$$PDF_j(model, \varepsilon') = \alpha PDF_j(source, \varepsilon') + (1-\alpha) PDF_j(background, \varepsilon') \quad \text{(C.21)}$$

where $PDF_j(source, \varepsilon')$ and $PDF_j(background, \varepsilon')$ are the PDF of the source and background photon spatial distribution which are the source and background photon spatial model weighted by the LAT exposure and then convolved with the PSF in the given energy band. `Sourcelike` requires that the source photon spatial distribution is radial symmetric, so

$$PDF\left(\overrightarrow{r'}, \varepsilon'\right) = \int d\vec{r} P\left(\left|\overrightarrow{r'} - \vec{r}\right|, \varepsilon'\right) \tilde{S}(\vec{r}) \int dt A(\varepsilon', \vec{r}, t) \quad \text{(C.22)}$$

where $\tilde{S}(\vec{r})$ is the intrinsic radial profile of source photons, $\int dt A(\varepsilon', \vec{r}, t)$ is the LAT exposure in the direction $\vec{r}$ and at energy ε', and $P\left(\left|\overrightarrow{r'} - \vec{r}\right|, \varepsilon'\right)$ is the PSF. α is called the signal fraction.

The purpose of maximizing during a source analysis is to calculate the particular value of α which maximizes the log-likelihood function for a particular source model, so any additive terms in Eq (C.10) not depending on the signal fraction may be dropped from the calculation:

$$\ln L = \sum_j n_j \ln \theta_j = \sum_j n_j \ln(\alpha P_j(source) + (1-\alpha) P_j(background)) \quad \text{(C.23)}$$

This log-likelihood function does not depend on the source or background spectral model at all.

The maximization is done independently for each energy band. The TS for the energy band is defined as

$$TS = 2 \times [\ln\left(L(\alpha = \alpha_{max})\right) - \ln\left(L(\alpha = 0)\right)] \quad \text{(C.24)}$$

and the final TS is the sum of the TS value for each energy band.

APPENDIX D
NFW PROFILE IN `SOURCELIKE`

D.1 Implementation [a]

The NFW profile is a typical density profile for DM satellites. Its unique cuspy shape makes it very different with other source profiles. In order to optimize the `sourcelike` sensitivity to DM extended satellites, we implement the NFW profile in `sourcelike`.

As described in Appendix C, we need to provide the intrinsic radial distribution of source photons $\tilde{S}(\vec{r})$. Since the γ-ray flux from WIMP annihilation is as Eq (3.1), then

$$\tilde{S}(\vec{r}) \propto \int_{l.o.s} \rho(\vec{r}(l))^2 dl$$
$$\propto \int_{l.o.s} \left(\frac{1}{\frac{r(l)}{r_s}\left(1+\frac{r(l)}{r_s}\right)^2}\right)^2 dl \quad \text{(D.1)}$$

When the satellite is far away ($D \gg r_s$, D is the satellite distance to the Earth) as Figure D.1 shows, we can approximate the above integral using the cylinder coordinate:

$$\tilde{S}(\vec{r}) \propto \int_{-\infty}^{\infty} \rho(\overrightarrow{r'})^2 d\,z \quad \text{(D.2)}$$

Assuming $\sin\alpha = \frac{r}{r'}$, then $z = \frac{r}{\tan\alpha}$. So Eq (D.2) can be written as

$$\tilde{S}(\vec{r}) \propto \int_0^{\pi} \frac{1}{\left(\frac{r'}{r_s}\right)^2\left(1+\frac{r'}{r_s}\right)^4} d\left(\frac{r}{\tan\alpha}\right)$$
$$= \int_0^{\pi} \frac{1}{\left(\frac{r}{r_s}\right)^2 \frac{1}{(\sin\alpha)^2}\left(1+\frac{r}{r_s\sin\alpha}\right)^4} \frac{r}{(\sin\alpha)^2} d\alpha$$
$$= \int_0^{\pi} \frac{{r_s}^2}{r} \frac{1}{\left(1+\frac{r}{r_s\sin\alpha}\right)^4} d\alpha \equiv I(r) \quad \text{(D.3)}$$

[a]: Acknowledge Markus Ackermann for his help on this section.

The integral in Eq (D.3) can not be computed analytically. `Sourcelike` can only take a analytical function of $\tilde{S}(\vec{r})$. Therefore, we use an analytic function $f(r)$ to approximate the integral $I(r)$:

$$f(r) = \frac{r_s}{r}\frac{3.14}{(1+\frac{r}{r_s})^5} \tag{D.4}$$

where r is the radial distance from the satellite center.

In Figure D.2, we directly compare the numerical integral *I(r)* (in black) and the function *f(r)* (in red) on the left panel, and plot the fractional difference of the two as a function of r/r_s on the right panel. The two curves are very consistent at small r/r_s. Although at large r/r_s the deviation of the two curves is large, it contributes very few photons at large radius. The flux inside r_s is about 92% of the total flux, and the flux inside $r_s/3$ is about 68% of the total flux.

Finally, we normalize *f(r)* to 1 and obtain

$$\tilde{S}(R) = \frac{2}{\pi R_0 R(1+\frac{R}{R_0})^5} \tag{D.5}$$

where $R_0 = r_s/D$ is the satellite extension and $R = r/D$ is the angular distance from the satellite center seen from the Earth. `Sourcelike` can find the best-fit R_0 by maximizing the likelihood function.

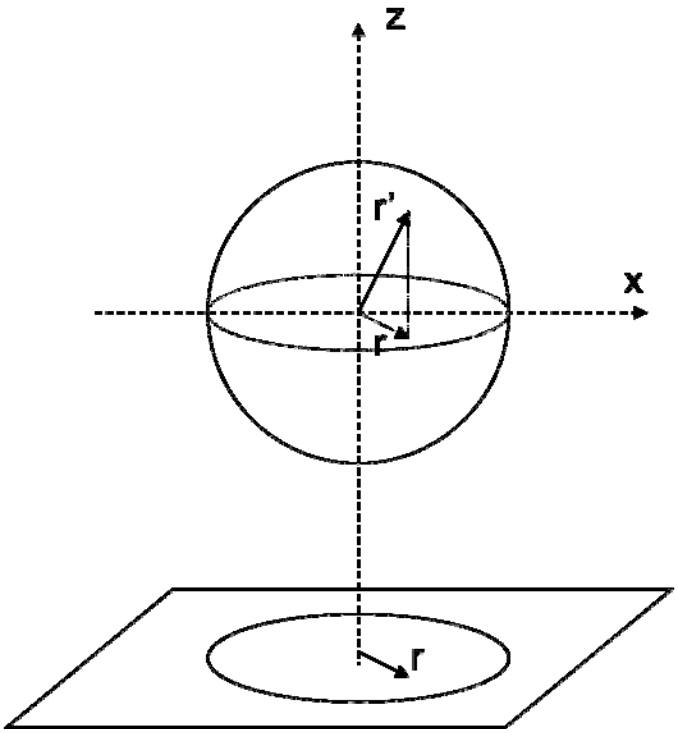

Figure D.1 A cartoon diagram demonstrating the satellite distance and radius in cylinder coordinate.

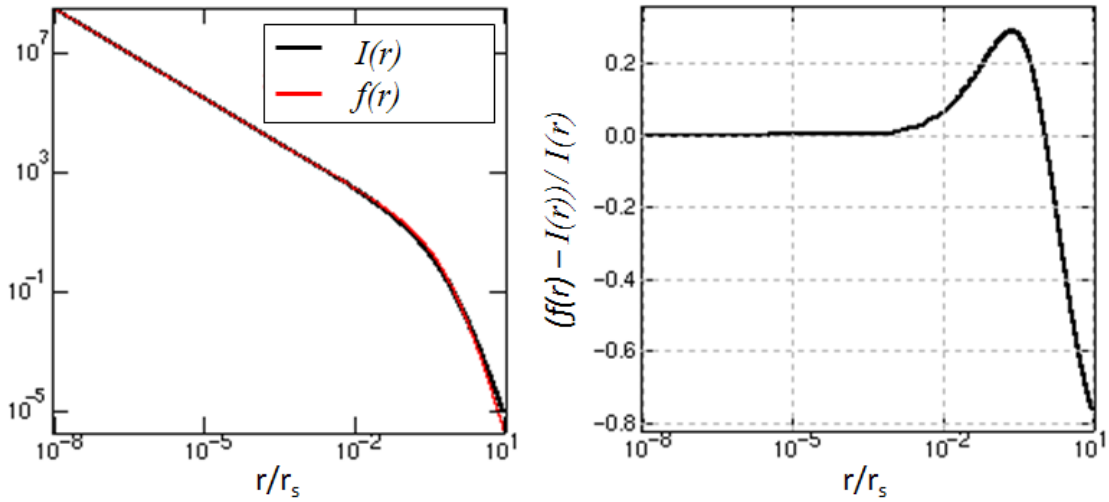

Figure D.2 Left panel: numerical integral *I(r)* (in black) and the function *f(r)* (in red) versus r/r_s. Right panel: fractional difference of the two lines versus r/r_s.

D.2 Validation

To verify the NFW profile works correctly on fitting source extension, we generated MC simulation of sources with the NFW profile, fitted them with the NFW profile using `sourcelike` and compared the input and the best-fit extension.

First, we used `gtobssim` to simulate a point source with the integral flux $5 \times 10^{-8} cm^{-2} s^{-1}$ in the energy range 200 MeV – 300 GeV. The source spectrum is a power-law with the spectral index -2.0. The spectral model does not affect the fitting result because the likelihood function in `sourcelike` does not depend on spectral models. Instead of simulating and fitting a point source at a fixed location 1000 times, we threw a MC point source at a random location with $|b| > 20^o$ 1000 times. Then we combined this point source with the diffuse background which was simulated using the extrapolated Galactic diffuse model (see Appendix B) and the isotropic diffuse model (isotropic_iem_v02.txt). After fitting the combined data with the input diffuse background models and point source model, the distribution of the best-fit source extension R_0 for 1000 simulations is shown in Figure D.3. The distribution has a narrow spike at zero extension and a small tail spread to large extension, which agrees with what we expected for a point source.

Second, we simulated a bright NFW source with a large extension $R_0 = 2^o$and the integral flux $10^{-7} cm^{-2} s^{-1}$ (200 MeV – 300 GeV) using `gtobssim`. The source spectrum is the spectrum for 100 GeV WIMPs annihilating into the $b\bar{b}$ channel. After fitting the combined MC background and source data with the input diffuse models and NFW source model, the distribution of the best-fit source extension R_0 for 1000 simulations is shown in Figure D.4. The distribution can be fitted with a Gaussian function with the mean 1.91^o and the standard deviation 0.09^o. Although the best-fit mean is less than the true extension, it is still consistent with the true value within 1σ.

Finally, we simulated two fainter and less extended NFW sources $R_0 = 1^o and\ 0.5^o$ and integral flux $3 \times 10^{-9} cm^{-2} s^{-1}$ (200 MeV – 300 GeV). We fitted the background and source with the input models. The distribution of the best-fit source extension R_0 for 1000 simulations is shown in Figure D.5. The left panel is for the simulated NFW sources with $R_0 = 0.5^o$, and the right panel is for the ones with $R_0 = 1^o$. The distributions are well approximated by Gaussian functions. The fitted Gaussian mean values are 0.42^o and 0.89^o, and the standard deviations are 0.41^o and 0.48^o, respectively. The best-fit means are consistent with the true extensions within 1σ. The effect of disallowing negative extension shows up in the distribution for the less extended source as a piling up of the distribution at zero extension.

In summary, the NFW profile is successfully implemented in `sourcelike` and works well on fitting the extension of NFW sources although the best-fit extension R_0 is systematically smaller than the true value. The systematic offset of the mean value and the width of the distribution of R_0 depend on the source's true extension and flux. Brighter and more extended sources tend to have smaller systematic offset of the mean value and a narrower distribution of R_0.

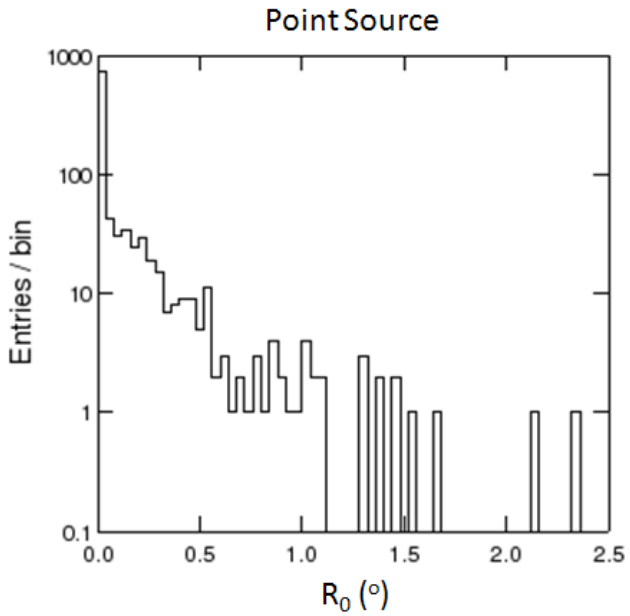

Figure D.3 Best-fit source extension R_0 for 1000 simulations of a point source. Most of the fits give 0.0.

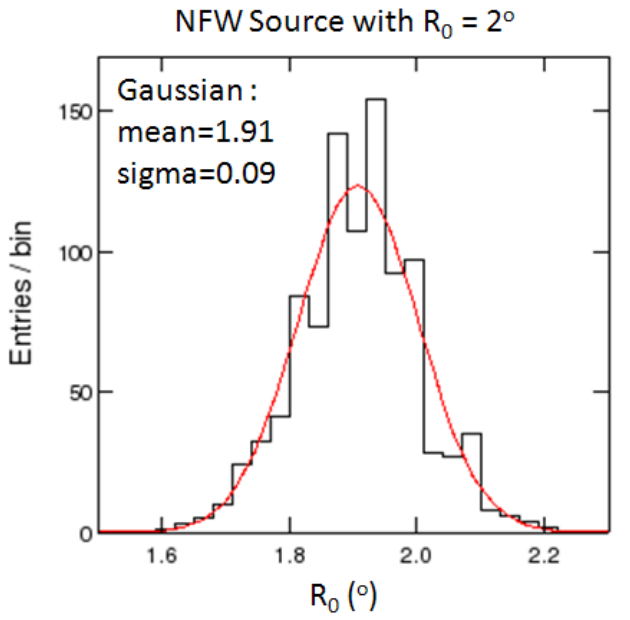

Figure D.4 Best-fit source extension R_0 for 1000 simulations of a bright NFW source with the true extension $R_0 = 2^o$ and the integral flux $10^{-7} cm^{-2} s^{-1}$ in the energy range 200 MeV – 300 GeV. The distribution can be fitted with a Gaussian function (in red) with the mean 1.91° and the standard deviation 0.09°.

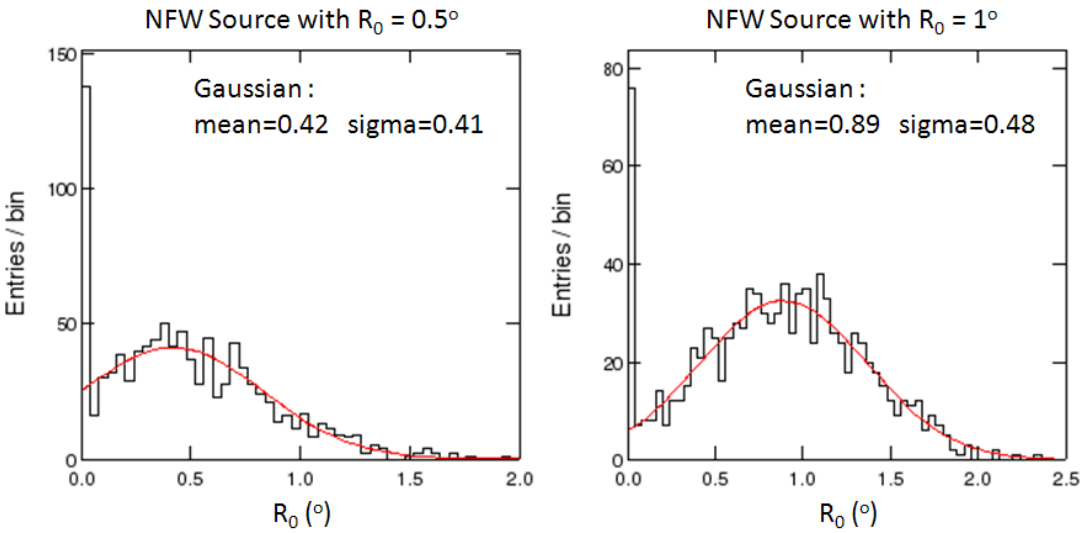

Figure D.5 Best-fit source extension R_0 for 1000 simulations of NFW sources. Left panel is for the simulated NFW sources with the true extension $R_0 = 0.5^o$ and the integral flux $3 \times 10^{-9} cm^{-2} s^{-1}$ in the energy range 200 MeV – 300 GeV. Right panel is for the simulated NFW sources with the true extension $R_0 = 1^o$ and the integral flux $3 \times 10^{-9} cm^{-2} s^{-1}$ in the energy range 200 MeV – 300 GeV. The distributions are well approximated by Gaussian functions (in red). The fitted Gaussian mean values are 0.42^o and 0.89^o, and the standard deviations are 0.41^o and 0.48^o, respectively. The effect of disallowing negative extension shows up in the distribution for the less extended source as a piling up of the distribution at zero extension.

APPENDIX E

DMFIT [a] IN `GTLIKE`

DMFIT is a fitting interface initially written in FORTRAN by Tesla Jeltema and Stefano Profumo for XSPEC [78]. The core functionalities have been translated in C and interfaced to `gtlike`. It allows for the simultaneous fit of the spectrum normalization, the DM candidate mass, and the branching ratio between two given possible annihilation channels. The DM annihilation spectra for different masses and channels are defined in a table, which is calculated by `DarkSUSY`.

In order to verify that DMFIT works correctly in `gtlike`, we generated MC simulation of point sources with the spectrum for 100 GeV WIMPs annihilating into the $b\bar{b}$ channel and the integral flux $8.6 \times 10^{-9} cm^{-2} s^{-1}$ in the energy range 200 MeV – 300 GeV. These simulations were then fitted with the $b\bar{b}$ channel using `gtlike` DMFIT and we compared the input and the output best-fit DM mass and flux. We did 1000 simulations. Figure E.1 shows the best-fit DM mass (left panel) and the best-fit flux (right panel). The distributions can be fitted with Gaussian functions. The fitted Gaussian mean values are 96.1 GeV and $8.9 \times 10^{-9} cm^{-2} s^{-1}$, and the standard deviations are 13.1 GeV and $6.4 \times 10^{-10} cm^{-2} s^{-1}$, respectively. Thus, DMFIT works well on fitting the DM mass and flux of DM sources.

[a]: Acknowledge Johann Cohen-Tanuge for his contributions to DMFIT in `Science Tools`.

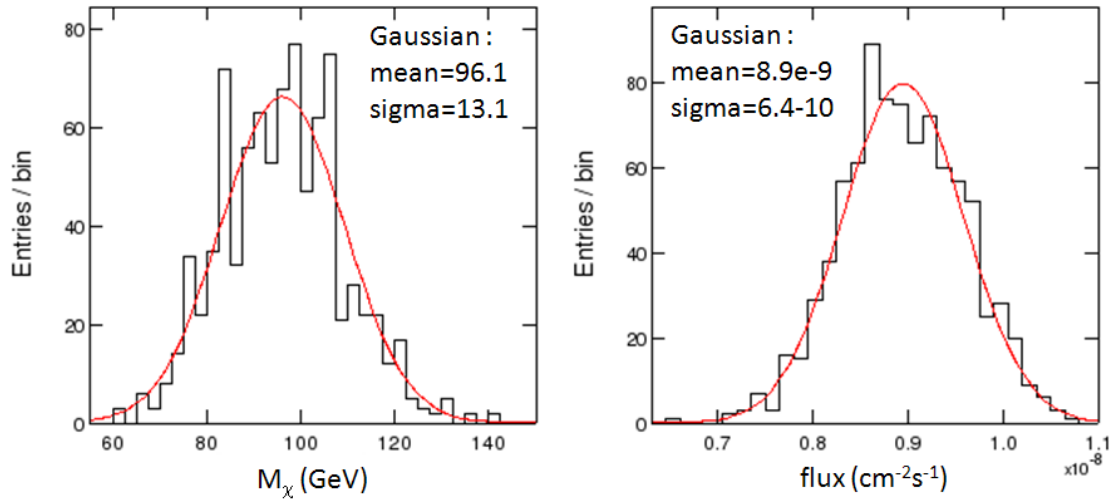

Figure E.1 Best-fit DM mass (left panel) and the best-fit flux (right panel). The distributions are fitted with Gaussian functions (in red). The fitted Gaussian mean values are 96.1 GeV and $8.9 \times 10^{-9} cm^{-2} s^{-1}$, and the standard deviations are 13.1 GeV and $6.4 \times 10^{-10} cm^{-2} s^{-1}$, respectively.

APPENDIX F

PHOTON SELECTION FROM LAT GROUND COSMIC RAY DATA [a]

The *Fermi* LAT was calibrated on the ground with Cosmic Ray (CR) muons. We proposed to use CR photons to cross check the LAT calibration independently. If we knew how to obtain a clean CR photon sample from the cosmic rays, we could compare real photon data with the Monte Carlo (MC) photon data, "Engineering Model (EM)-v6070329p16/All_gamma_10MeV_20GeV_4M" generated by SLAC fellow Anders Borgland in May 2006. Based on the comparison, we could evaluate how well the LAT was calibrated.

F.1 Photon Purity Cuts

According to the photon's properties, we came up with a series of cuts to select pure photons. These cuts were highly efficient in removing CR muons and electrons. This series of cuts is:

- AcdTileCount = 0 and AcdRibbonCount = 0

Select events which do not fire any ACD tile or ribbon, since only charged particles can fire the ACD.

- AcdCornerDoca < -50 or AcdCornerDoca > 50 *mm*

Select events whose tracks do not point anywhere near a gap in the side ACD tiles at 4 corners, in case of charged particles coming through gaps of ACDs at corners.

[a]: This work was done in 2006.

- 30 < CalEnergyRaw < 20000 MeV

Select events with the same energy range as the corresponding MC photon simulation.

- 0 < CalEdgeEnergy < 20 MeV

Select events which leak small energy from the edges between CAL modules.

- 0 < CalTransRms < 35 *mm*

Select events which have the correct shapes of electromagnetic showers in the CAL, so as to reject multiple particles.

- -0.5 < CalTrackAngle < 0.8

Select events whose incident directions are in good alignment with propagation directions in the CAL, since photons' tracks line up roughly in the TKR and CAL.

- -180 < CalZEcntr < -50 *mm*

Select events whose energy centroid is not too far back in the CAL to prevent too much energy leakage from the bottom of the CAL.

- 0.5 < TkrNumTracks < 3.5

Select events with one, two or three tracks in the TKR to make sure incident directions are correctly reconstructed.

By applying the above cuts to MC muon data, 99.999997% of the muons were filtered out. Thus, after the photon purity cuts, we obtained the CR photons of high purity.

F.2 Fiducial Beam Cuts

In order to optimize the angular resolution and the energy resolution of photon events, we performed another series of cuts to make sure all the photon conversions (vertices) were well contained in the fiducial volume of the tracker (TKR) and all the photons went through the whole length of the calorimeter (CAL). The fiducial volume was defined as the center 1000 *mm* by 1000 *mm* region of the TKR. This group of cuts is:

- -500 *mm* < VtxX0 < 500 *mm* and -500 *mm* < VtxY0 < 500 *mm*

Select events whose vertices are in the center 1000 *mm* by 1000 *mm* region of the TKR.

- VtxZDir < VtxZDir_critical

Select events which go through the whole CAL. VtxZDir_critical is defined as

$$VtxZDir\_critical = -\cos\alpha \tag{F.1}$$

where α is as shown in Figure F.1, and

$$\tan\alpha = \frac{740 - \max\left(|VtxX0|, |VtxY0|\right)}{876.2} \tag{F.2}$$

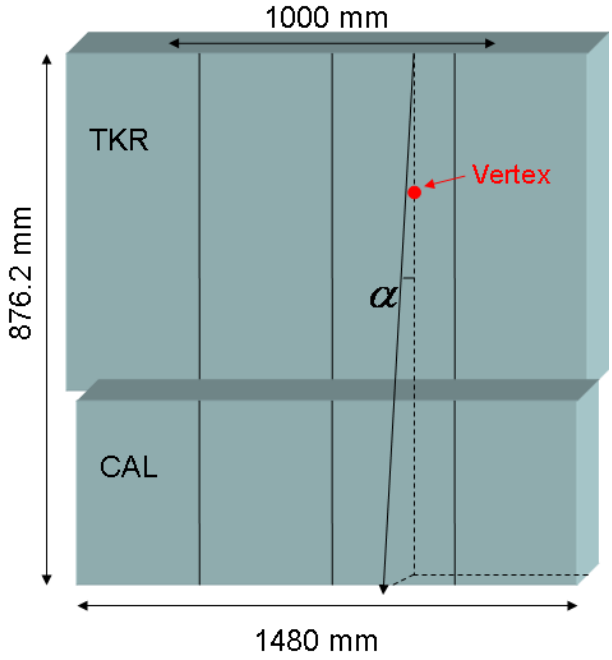

Figure F.1 A cartoon diagram of the LAT structure to demonstrate the definition of VtxZDir_critical.

After applying the photon purity cuts and the fiducial beam cuts to the MC photon data, good agreement was found on the spatial distribution of the photon vertex between the MC truth and the real data measurements. Figure F.2 shows the distribution of the MC true position of the photon vertex (left) and the distribution of the measured position of the photon vertex (right) for the MC photon data "Engineering Model (EM)-v6070329p16/All_gamma_10MeV_20GeV_4M" generated by SLAC fellow Anders Borgland in May 2006. After the cuts 99.998% of the photons were indeed in the fiducial volume. Therefore, the photon purity cuts and the fiducial beam cuts worked very well.

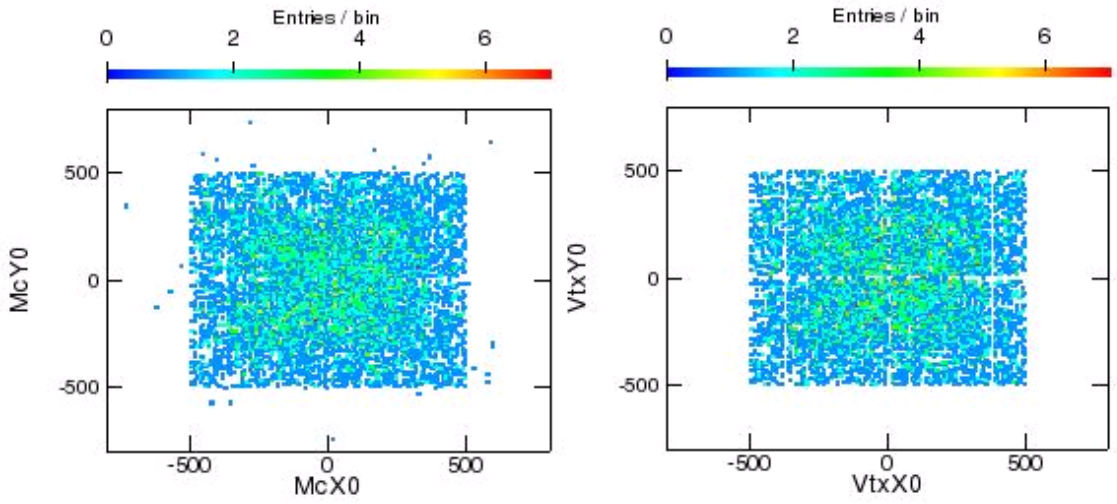

Figure F.2 Distribution of the MC true position of the photon vertex (left) and the distribution of the measured position of the photon vertex (right) for the MC photon data "EM-v6070329p16/All_gamma_10MeV_20GeV_4M" after the photon purity cuts and the fiducial beam cuts.

F.3 New Energy Variable – EvtEnergyCorr_CalCfp

Before figuring out how to calculate the energy spectrum for the clean CR photons, we had to validate that the photon energy was correctly measured. At present, CTBBestEnergy is considered as the best measured energy which uses the method called classification trees to decide the most suitable energy reconstruction algorithm from the three algorithms – parametric, profile [79] and likelihood [80]. However, in 2006 our collaboration did not have such agreement on the best reconstructed energy. In that situation, we proposed a new energy variable called EvtEnergyCorr_CalCfp as the best measured energy, based on the two energy variables – "EvtEnergyCorr" using a parametric method and "CalCfpEnergy" using a profile method. It was defined as

$$EvtEnergyCorr\_CalCfp = \begin{cases} EvtEnergyCorr & \text{If CalEnergyRaw <= 1GeV} \\ CalCfpEnergy & \text{If CalEnergyRaw > 1 GeV and CalCfpEffRLn > 4} \\ N/A & \text{Otherwise} \end{cases} \quad \text{(F.3)}$$

where N/A means the energy of such photons could not be well reconstructed.

This new energy variable worked well in our analysis. We compared "EvtEnergyCorr_CalCfp" with the MC true energy "McEnergy" for the MC photon data "EM-v5r070305p4/LAT_All_Gamma_10MeV-20GeV". As shown in Figure F.3, the excellent agreement between the distributions of those two variables indicated that EvtEnergyCorr_CalCfp was an accurate measurement of photon energy.

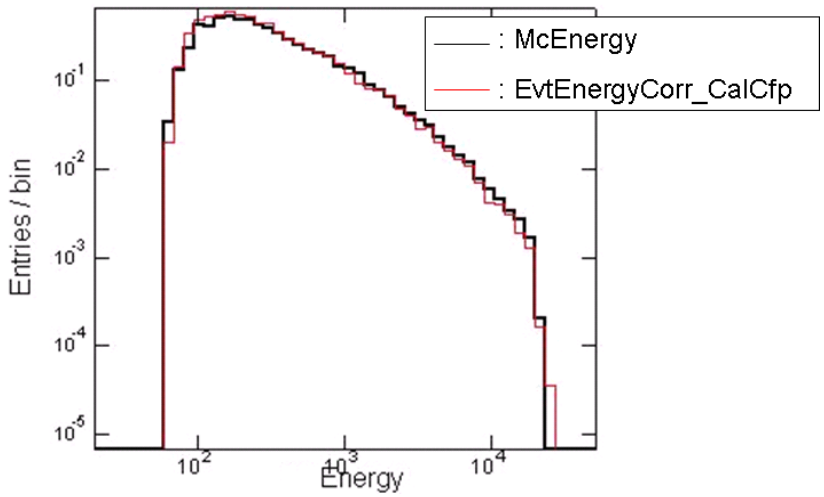

Figure F.3 Distribution of EvtEnergyCorr_CalCfp (in red) and McEnergy (in black) for the MC photon data "EM-v5r070305p4/LAT_All_Gamma_10MeV-20GeV".

F.4 Input CR Photon Energy Spectrum

The input photon energy spectrum is the energy spectrum of the incident CR photons. The output energy spectrum is the energy spectrum of the photons after the photon purity cuts and the fiducial beam cuts. The photon selection efficiency is the ratio of the input and the output energy spectrum. This efficiency can be obtained using the MC photon data. If we assume the photon selection efficiency is the same for the real CR photon data and for the MC photon data, the input energy spectrum can be estimated by multiplying the output energy spectrum by the photon selection

efficiency obtained from the MC. Due to the backsplash effect, high-energy photons can trigger the ACD so that they will be rejected by the photon purity cuts. Therefore, only the output energy spectrum below 5 GeV is eligible in our analysis.

Here are the four steps to obtain the input energy spectrum of the real CR photons.

First, we used the MC photon data "EM-v6070329p16/All_gamma_10MeV_20GeV_4M" generated by Anders Borgland in May 2006 to obtain the input and the output spectrum. In Figure F.4, the left panel shows the input energy spectrum which is a simple power law function with the spectral index -1.0; the right panel shows the output energy spectrum which is fitted to a Log Parabola function. As a result, the two spectra were expressed as

$$\frac{dN_{MC,input}}{dE} = 5.26 \times 10^5 \times E^{-1.0} \quad \text{(F.4)}$$

$$\frac{dN_{MC,output}}{dE} = norm \times E^{-(\alpha+\beta lnE)} \quad \text{(F.5)}$$

where $norm = 5.74726, \alpha = -0.75968, \beta = 0.129754$.

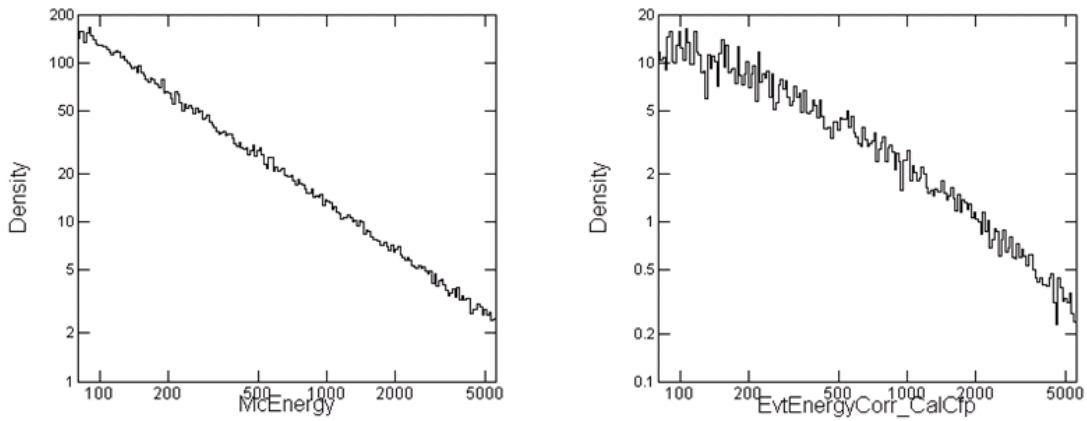

Figure F.4 The input (left panel) and the output (right panel) energy spectrum of the MC photon data "EM-v6070329p16/All_gamma_10MeV_20GeV_4M".

Second, the photon selection efficiency was calculated using the input and the output energy spectrum obtained above:

$$Efficiency(E) = \frac{\frac{dN_{MC,output}}{dE}}{\frac{dN_{MC,input}}{dE}} \quad \text{(F.5)}$$

This efficiency was a function of energy as shown in Figure F.5.

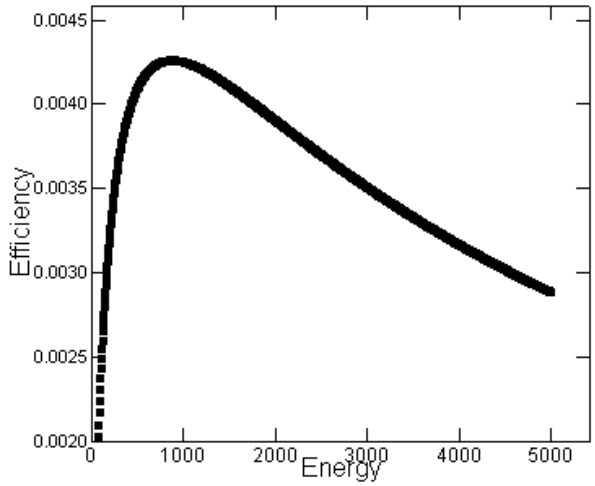

Figure F.5 Photon selection efficiency for the MC photon data "EM-v6070329p16/All_gamma_10MeV_20GeV_4M".

Third, we applied photon purity cuts and the fiducial beam cuts to the 14 runs of real CR data to generate the output energy spectrum. These 14 runs of data were produced by exposing the LAT in the CR in SLAC Bldg 33 with the nominal settings. The run ids were from 77003051 to 77003064. The output energy spectrum is shown in Figure F.6. It was fitted to a Log Parabola function:

$$\frac{dN_{CR,output}}{dE} = norm \times E^{-(\alpha+\beta lnE)} \quad \text{(F.6)}$$

where $norm = 46.1267, \alpha = -1.74579, \beta = 0.336248$.

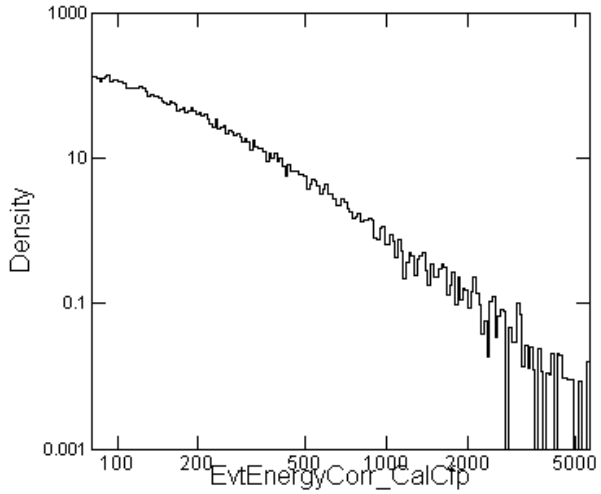

Figure F.6 Output energy spectrum for the 14 runs of real CR data.

Finally, the input energy spectrum of the real CR photons was calculated as:

$$\frac{dN_{CR,input}}{dE} = Efficiency(E) \times \frac{dN_{CR,output}}{dE} \quad \text{(F.7)}$$

Figure F.7 shows the input energy spectrum for the 14 runs of data. In other words, it was the energy spectrum of the incident CR photon in SLAC Bldg 33. This input energy spectrum was fitted as:

$$\frac{dN_{CR,input}}{dE} = norm \times E^{-(\alpha+\beta lnE)} \quad \text{(F.8)}$$

where $norm = 4.2216 \times 10^6, \alpha = -0.01389, \beta = 0.206494$.

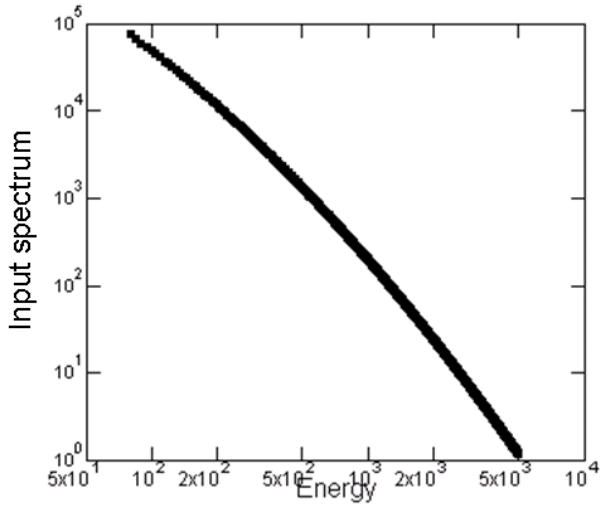

Figure F.7 Input energy spectrum for the real CR photons in SLAC Bldg 33.

F.5 MC Simulation of CR Photons

Since the input energy spectrum of the real CR photons in SLAC Bldg 33, Eq (F.8), was derived, we used this spectrum function to generate the MC photon data "testMC_3051_3064/All_gamma_10MeV_20GeV_45M" in July 2006. By applying photon purity cuts and the fiducial beam cuts to this MC data and to the 14 runs of real CR data mentioned in §F.4, we had two output data sets. Those two data sets were supposed to be the same; if not, it meant something was wrong with the LAT calibration. We simulated 45 million photons to make the number of the after-cut photons for the MC data comparable to that for the real data. Figure F.8 shows the output energy spectrum and Figure F.9 shows the distribution of photon vertex direction for the MC and the real data after cuts. From these plots, the energy spectra and the distribution of photon vertex direction were very consistent for the MC photon data and the real CR photon data. However, it was impossible to compare hundreds of variables by eyes. Hence we needed a tool to quantify the differences of all variables from the MC photon data and the real CR photon data.

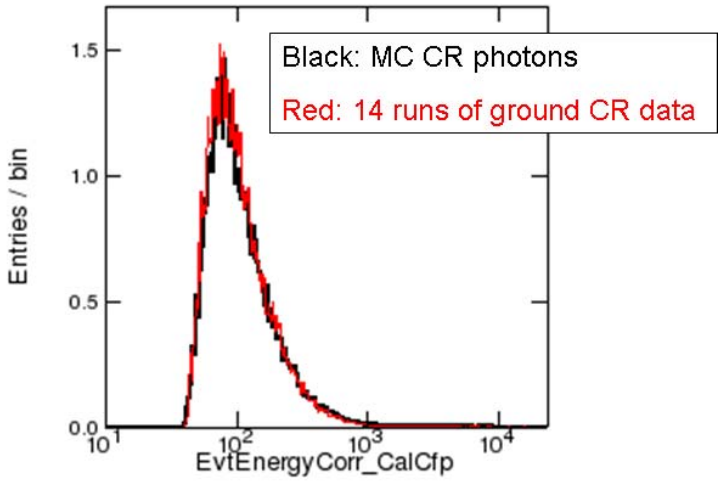

Figure F.8 Output energy spectrum for the MC photon data "testMC_3051_3064/All_gamma_10MeV_20GeV_45M" (in black) and for the 14 runs of real CR photon data (in red).

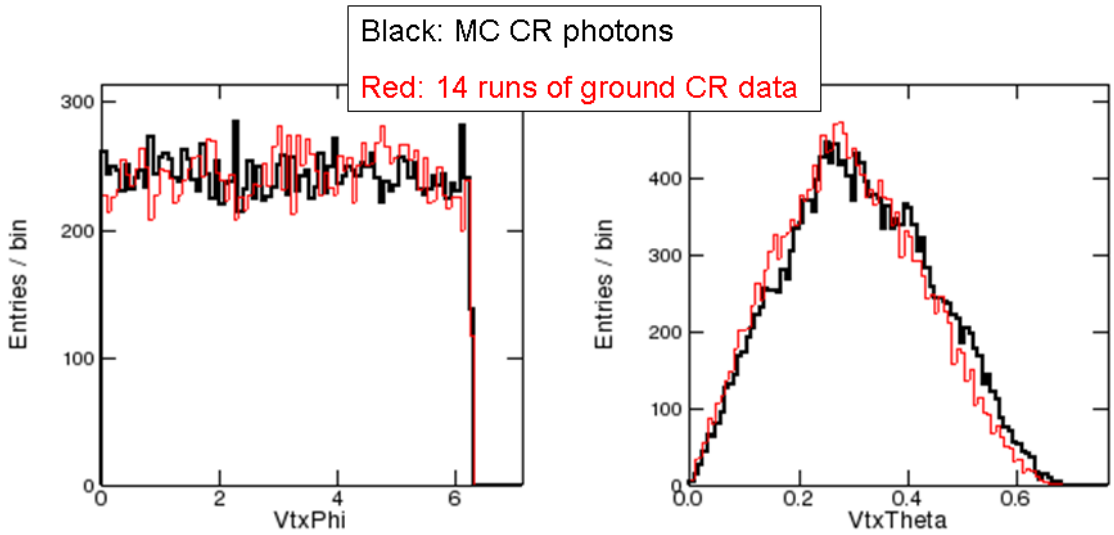

Figure F.9 Distribution of photon vertex direction for the MC photon data "testMC_3051_3064/All_gamma_10MeV_20GeV_45M" (in black) and for the 14 runs of real CR photon data (in red).

F.6 Comparison of Real Input CR Photons and Simulated CR Photons Using `rForest` [a]

`RForest` [81][82] is a statistical analysis tool based on the classification trees. It performs background rejection for *Fermi* LAT data using random forests. This tool can also tell how much difference between two data sets with partially or all common variables.

In order to correctly interpret the results from `rForest`, we created a simple test case. We randomly split the after-cut MC data "testMC_3051_3064/All_gamma_10MeV_20GeV_45M" into two data sets with equal number of events in each, and ran `rForest` to compare these two independent MC data sets. Because these two MC data sets originally came from the same MC data, they should have identical distributions for all the variables. The five most important variables used to distinguish the two data sets from the result of `rForest` are listed in Table 1. Z-score is the number of σ for a standard normal distribution, which is used to distinguish the null and the alternative hypothesis. Here, the null hypothesis is the variable has the same distribution for the two data sets and the alternative hypothesis is the variable has different distributions for the two data sets. Significance level (a.k.a p-value) is the area of the tail above the value of z-score for the standard normal distribution, which means the probability that a value >= z-score would be observed under the null hypothesis.

In Table F.1, the most important variable is TkrEnergyCorr, and if this variable has the same distribution in the two data sets, the probability that z-score >= 3.4 is 0.03% which is a 3.4 σ significance. Qualitatively speaking, according to Table F.1, the maximum z-score is about 3 for the two data sets with identical distributions of all the variables.

[a]: Acknowledge David Paneque for his help on this section.

Table F.1 The five most important variables when comparing two independent MC data sets with identical distributions for all variables.

Variable	Raw Score	Z-score	Significance Level
TkrEnergyCorr	0.0804604	3.44079	0.000290012
VtxS2	0.0096729	2.97544	0.00146287
TkrUpstreamHC	0.0108485	2.73885	0.00308277
CalZEcntr	0.0498681	2.61028	0.00452343
Tkr1CoreHC	0.0319121	2.55805	0.00526298

After the exploration of the above test case, we used the same technique to compare the MC photon data with the real CR photon data described in §F.5. The ten most important variables used to distinguish the two data sets from the result of `rForest` are listed in Table F.2. Those variables have much larger z-scores than those in Table F.1, which means the MC photon data and the real CR photon data had big differences.

Table F.2 The ten most important variables when comparing the MC photon data and the real CR photon data.

Variable	Raw Score	Z-score	Significance Level
AcdRibbonCount	3.03183	54.2258	0
GltWord	1.62063	14.196	0
AcdTotalEnergy	1.46759	13.1433	9.30087e-40
Tkr1ToTTrAve	0.300316	7.949	9.40124e-16
EvtECalXtalRatio	0.876486	6.9006	2.58909e-12
CalTotRLn	0.1028	5.86633	2.22771e-09
GltGemSummary	0.737837	5.86453	2.25206e-09
CalMIPRatio	0.218158	5.71679	5.42774e-09
CalTwrEdgeCntr	0.413068	5.63263	8.87386e-09
CTBCalFrontBackRatio	0.10352	5.0421	2.30222e-07

F.7 Discussion

Based on the above result from `rForest`, we found general agreement between the MC photon data and the real CR photon data with some interesting exceptions due to the problems in the LAT MC and real data calibration and reconstruction software.

First of all, the reason why ACD variables have such huge differences between the MC data and the real data is that the Pulse Height Analysis (PHA) thresholds for ACD tiles / ribbons are different values in the two data sets. For example, ACD tiles' threshold is 0.1 Minimum Ionization Particles (MIPs) in MC data and 0.02 MIPs in real data. In addition, the different ACD thresholds can lead to other problems, such as different trigger information recorded in MC data and real data. Figure F.10 shows the distribution of GltGemSummary which represents the trigger information. For real data, there is no trigger bit equal 3 or 7, which means no Region Of Interest (ROI) bit is set. The ROI bit is set only if there is a TKR trigger from the "shadowed" tower, in other words, only when the particle triggers TKR condition in the tower which has triggered ACDs. Therefore, the difference of GltGemSummary is due to the difference of ACD thresholds in the two data sets.

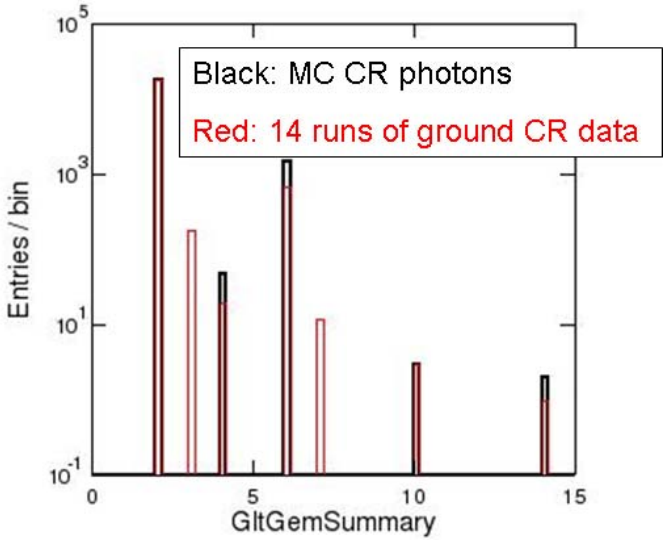

Figure F.10 Distribution of GltGemSummary for the MC photon data "testMC_3051_3064/All_gamma_10MeV_20GeV_45M" (black) and the 14 runs of real CR photon data (red).

Second, GltWord is another variable storing the trigger information besides GltGemSummary; nevertheless, GltWord used an incorrect CAL Low Energy (LO) threshlold to set CAL LO bit. For real data, the trigger has the correct CAL LO threshlold of 100 MeV, but the GltWord calculation uses the threshold of 20 MeV from an offline calibration file; while for MC data, the trigger and the calculation of GltWord both use the threshold of 20 MeV. Therefore, when comparing GltWord for real data and MC data we end up comparing CAL LO trigger for two different thresholds. As a result, GltWord has much more importance or more difference than GltGemSummary in the two data sets.

Third, CalTwrEdgeCntr is the distance of the energy centroid from the nearest tower boundary, and its distribution for real data and MC data is shown in Figure F.11. The peaks in real data correspond to the positions of the gaps between crystals, and they are due to the sampling effect to quantify CalTwrEdgeCntr for showers with small incoming angle. The first peak in MC data is due to both the inter-tower crack

and sampling effect. However, why is the first peak missing in real data? There were two hypotheses: problems in the reconstruction of the position in the CAL in real data because of the non-linearity in asymmetry based on the two diodes measurements, or lack of detection efficiency at the tower edges which is not properly described by MC simulation. This subtle problem will be finally corrected in Pass8 of the LAT reconstruction software due to be released sometime in 2012. Modification of the MC and new CAL reconstruction software was needed to make this improvement.

Finally, Tkr1ToTTrAve is the average Time Over Threshold (ToT) for the hits on the best track. As shown in Figure F.12, Tkr1ToTTrAve has a long tail at the right end for real data. This was a bug in the ToT reconstruction software that was recently fixed.

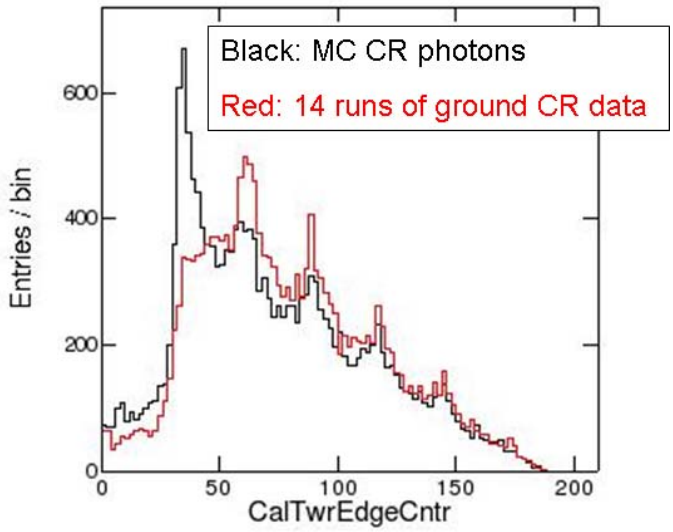

Figure F.11 Distribution of CalTwrEdgeCntr for the MC photon data "testMC_3051_3064/All_gamma_10MeV_20GeV_45M" (black) and the 14 runs of real CR photon data (red).

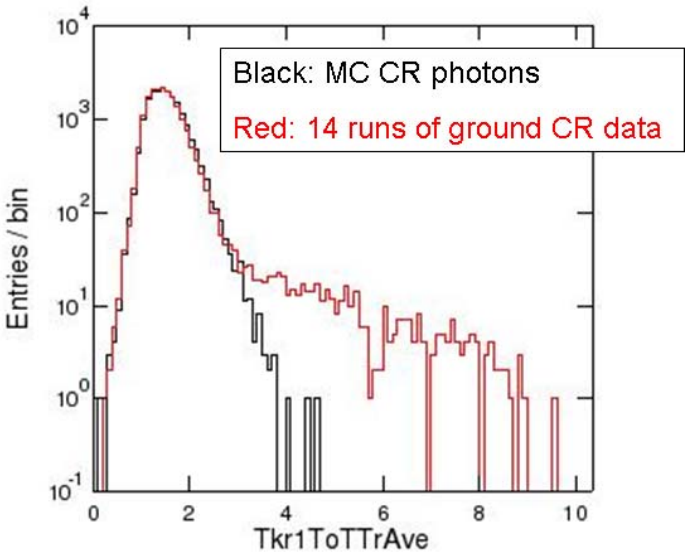

Figure F.12 Distribution of Tkr1ToTTrAve for the MC photon data "testMC_3051_3064/All_gamma_10MeV_20GeV_45M" (black) and the 14 runs of real CR photon data (red).

APPENDIX G
CROSS-CHECK OF THE LAT CALORIMETER CALIBRATION [a]

On the ground, the LAT CsI calorimeter (CAL) was calibrated with a front end charge injection system and cosmic ray muons [83]. On orbit, the CAL was calibrated using charge injection and cosmic ray protons. However, we originally intended to use cosmic ray heavy ions to calibrate the higher energy scales in 2006. Therefore, at that time it was crucial to know how the CAL responds to relativistic protons and heavy ions. In 2006, B. Lott et al. [84] presented their work on this question, showing that the measured energy was larger than the deposited energy which was opposite to that commonly expected, called the "antiquenching" effect. This "antiquenching" effect was unexpected as quenching of the light was expected, and there was no good physical explanation for it. In order to find out the reason for this unexpected "antiquenching" effect, we cross-checked parts of the previously done CAL calibration on the ground.

G.1 Energy Loss of Particles in GEANT4 and GLEAM

In the paper [84], they measured the energy deposition of relativistic nuclei (form carbon to iron) in the CAL at the GSI Helmholtz Accelerator Center, and then divided them by those extracted from the GEANT4 simulations to yield the quenching factors. Therefore, the unexpected larger-than-one quenching factors might have been due to incorrect GEANT4 simulations. Thus, it was necessary to verify the energy loss of relativistic heavy ions in the CAL calculated by GEANT4 before cross-checking the CAL calibration.

[a]: This work was done in 2007 – 2008.

G.1.1 WW dEdx Code

Weaver and Westphal (WW) [85] developed a state of the art dEdx code to calculate the energy loss of charged particles in matter based on the theory of ionization energy loss. This code has been confirmed by many experiments and been applied in the MARS15 MC code [86]. Therefore, the energy loss in the CAL can be cross-checked by using the WW dEdx code.

G.1.1.1 Muons

Figure G.1 shows the mean rate of energy loss of muons in CsI, calculated by the WW dEdx code, the Bethe-Bloch formula and the Particle Data Group (PDG). The results from those three methods are very consistent. For a muon with the kinetic energy 1021 MeV, the WW dEdx code gives dE/dx = 6.255 MeV/*cm*.

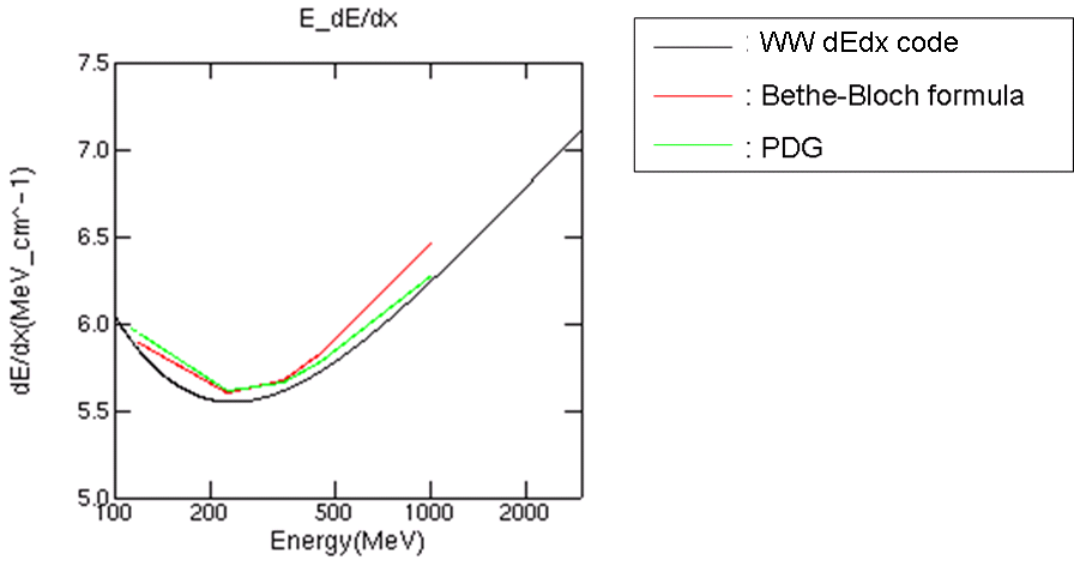

Figure G.1 Mean rate of energy loss of muons in CsI, calculated by the WW dEdx code, Bethe-Bloch formula and PDG respectively.

G.1.1.2 Protons

Figure G.2 shows the mean rate of energy loss of protons in CsI, calculated by the WW dEdx code, the Bethe-Bloch formula, the National Institute of Standards and Technology (NIST) and the Stopping and Range of Ions in Matter (SRIM) calculation. The NIST stopping power table is on the webpage http://physics.nist.gov/PhysRefData/Star/Text/PSTAR.html. SRIM is a group of programs which calculate the stopping and range of ions (up to 5 GeV/amu) into matter using a quantum mechanical treatment of ion-atom collisions, written by J. F. Ziegler and J. P. Biersack. The results from those four methods are very consistent. For a proton with the kinetic energy 6 GeV, the WW dEdx code gives dE/dx = 5.979 MeV/*cm*.

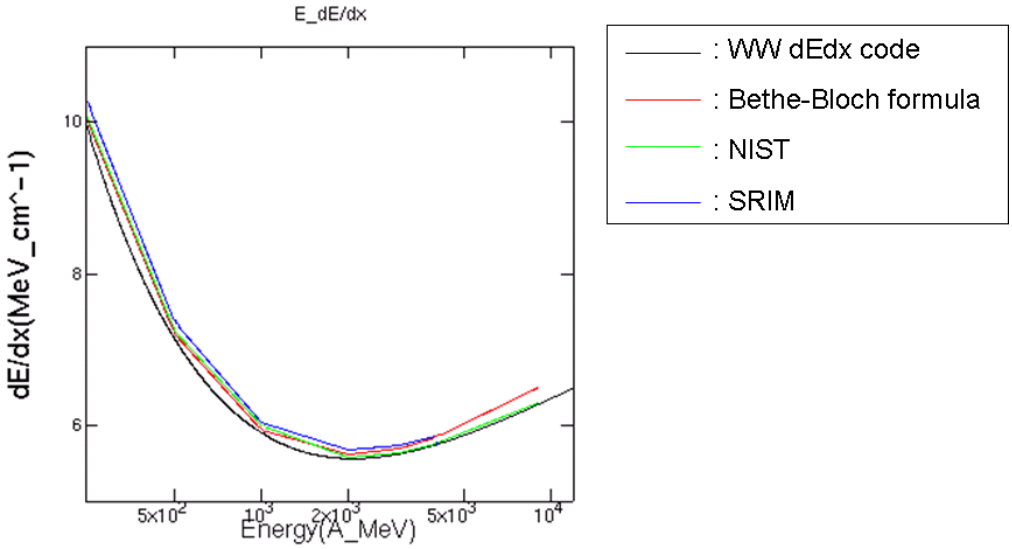

Figure G.2 Mean rate of energy loss of protons in CsI, calculated by the WW dEdx code, Bethe-Bloch formula, NIST and SRIM respectively.

G.1.1.3 Carbons

Figure G.3 shows the mean rate of energy loss of carbon in CsI, calculated by the WW dEdx code, the Bethe-Bloch formula and the SRIM calculation. The results from those three methods are very consistent. For a carbon with the kinetic energy 18 GeV (or 1.5 GeV/nucleon), the WW dEdx code gives dE/dx = 203.636 MeV/*cm*.

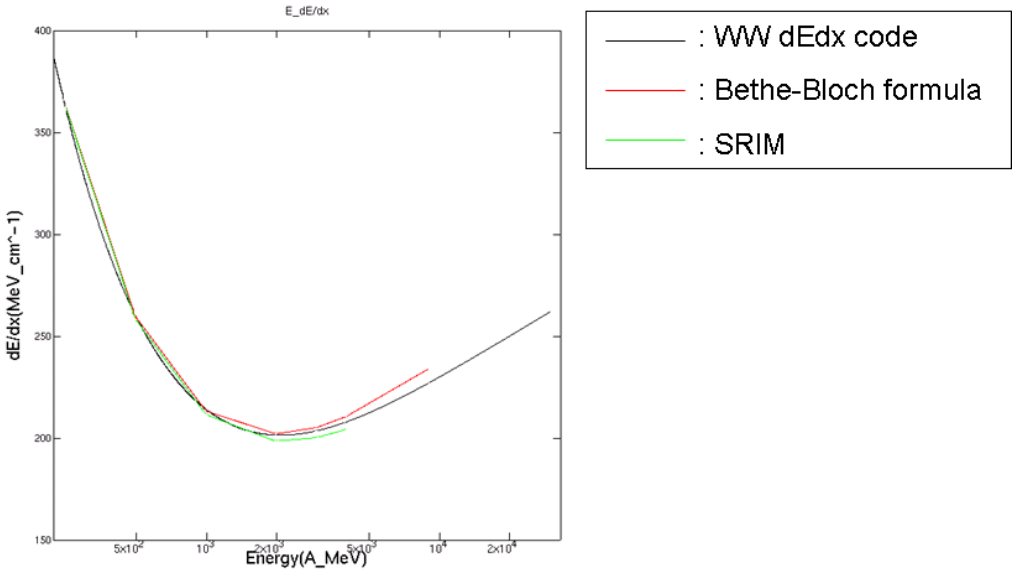

Figure G.3 Mean rate of energy loss of carbons in CsI, calculated by the WW dEdx code, the Bethe-Bloch formula and SRIM respectively.

G.1.2 GEANT4 Simulation of Muons

We used the version GEANT4 [87] 8.0.p01. We set up a simple CAL geometry in vacuum, which contained 8 layers of 12 CsI crystals. Each crystal had a height 1.99 cm, a width 3 cm and a length 40 cm. Muons with the kinetic energy 1021 MeV were vertically incident into the center of the central crystal. The cut value was set to be 1 mm. This cut value was converted to threshold energies for each material and for each particle type so that the particle with threshold energy stops (or is absorbed) after traveling the range cut distance.

We respectively calculated the rate of energy loss of muons, dE/dx, in the first crystal and in the whole CAL. Each muon went into the CsI crystals, and GEANT4 recorded its trajectory information at each step. The GEANT4 kept record of each step point on the volume boundary. In other words, the start points and end points of muons in each crystal were always saved, as point 1 and point 3 in Figure G.4. The other trajectory points between boundaries were calculated based on the mean free path of the particle, as point 2 in Figure G.4. For the muon's trajectory shown in Figure F.4, the energy loss was $dE\_FC = E_3\text{-}E_1$, the propagation distance was $dx\_FC = |\overrightarrow{x_1} - \overrightarrow{x_2}| + |\overrightarrow{x_2} - \overrightarrow{x_3}|$, and the rate of energy loss in the first crystal was $dE/dx\_FC = dE\_FC/dx\_FC$. In the same way, we calculated the energy loss and the total propagation distance in the whole CAL and the rate of energy loss in the whole CAL dE/dx_CAL.

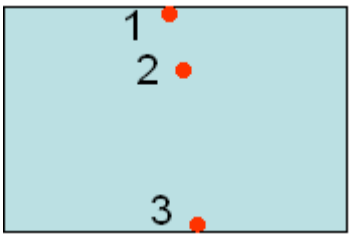

Figure G.4 A cartoon diagram of the first crystal. The red points show the muon's trajectory points. Point 1 and 3 are step points on the volume boundary.

The GEANT4 simulation result for 10000 muon events is shown in Figure G.5. The mean rate of energy loss in the first crystal, 6.349 MeV/cm, and that in the whole CAL, 6.322 MeV/cm, is reasonably the same. This rate agrees with the result from the WW dEdx code within 1.5% error.

We also checked the simulation result for 20000 muon events, and the mean rate of energy loss was very consistent with that from the simulation for 10000 muon events.

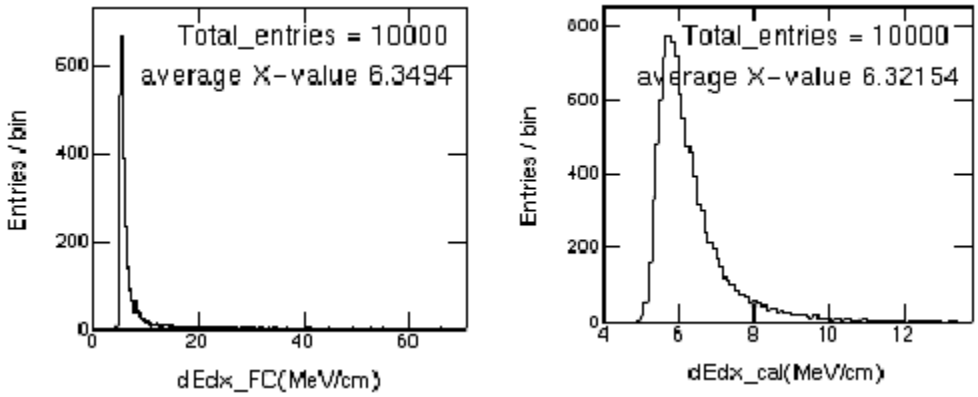

Figure G.5 Rate of energy loss of 1021 MeV muons in the first crystal (left panel) and in the whole CAL (right panel) simulated by GEANT4.

G.1.3 GLEAM Simulation of Muons, Protons and Carbons

The energy losses of the 1GeV muons, 6 GeV proton sand 18 GeV carbons in a full CAL were calculated using GLEAM. GLEAM [88] is a LAT Collaboration C++ package based on the GEANT 4 toolkit. GLEAM provides a detailed simulation of the physics processes and digitization within the LAT using a highly detailed simulation of the physics of the detector. We used GlastRelease v11r17, which assembled GEANT4 8.0.p01.

G.1.3.1 Muons

Muons with the kinetic energy 1021 MeV were vertically incident into the center of the central crystal. The launch point of muons was (x, y, z) = (201.17, 201.17, -48.12) *mm* which was just above the top crystal. Therefore, all the muons directly went into the CAL, and no other materials or physical processes can change the initial energy or direction of muons.

Figure G.6 shows the GLEAM result from simulating 10000 muon events. The mean rate of energy loss in the first crystal, 6.381 MeV/cm, and that in the whole CAL,

6.404 MeV/cm, is reasonably the same. This rate agrees with that from the WW dEdx code within a 2.0% error.

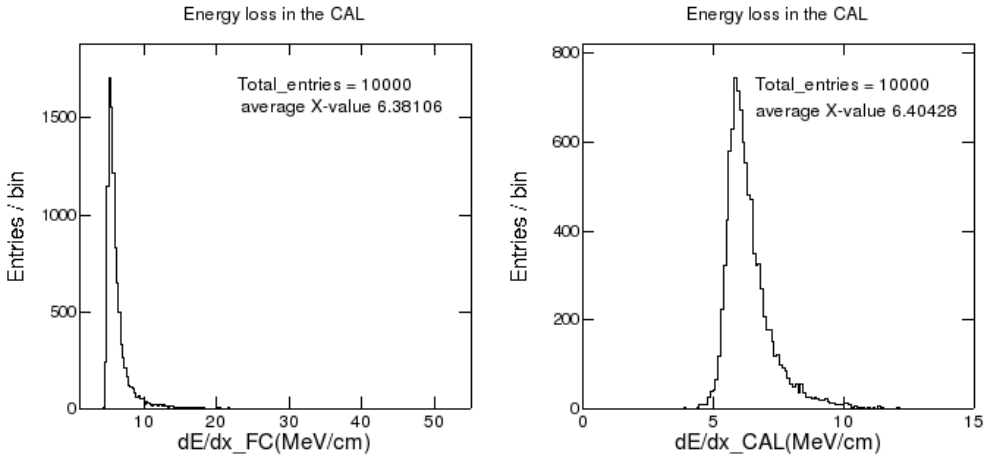

Figure G.6 Rate of energy loss of 1021 MeV muons in the first crystal (left panel) and in the whole CAL (right panel) simulated by GLEAM.

In order to prove that simulating 10000 muon events was enough to derive a stable mean rate of energy loss of muons, 20000, 40000 and 80000 muon events were also simulated respectively. The mean rate of energy loss for those simulations is shown in Figure G.7. The energy loss rate is kept stable both in the first crystal (black curve) and in the whole CAL (red curve) within less than 1% error.

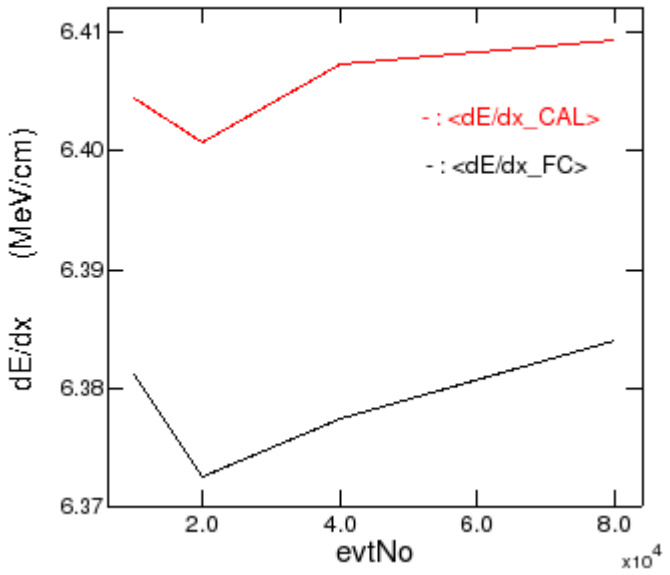

Figure G.7 Mean rate of energy loss of 1021 MeV muons in the first crystal (black curve) and in the whole CAL (red curve) versus the number of simulated events. Simulations were done by GLEAM.

G.1.3.2 Protons

Similar to the above muon simulation, protons with the kinetic energy 6 GeV were vertically incident from the same launch point (x, y, z) = (201.17, 201.17, -48.12) mm. Figure G.8 shows the GLEAM result by simulating 10000 proton events. The mean rate of energy loss in the first crystal is 6.102 MeV/cm, which agrees with that from the WW dEdx code within a 2.1% error.

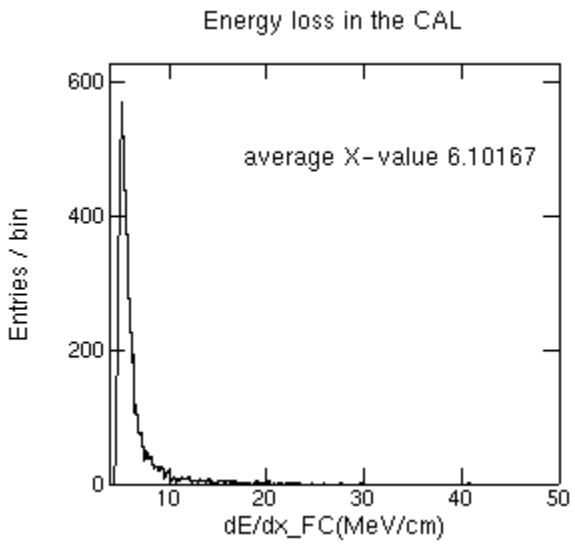

Figure G.8 Rate of energy loss of 10000 6 GeV protons in the first crystal simulated by GLEAM.

G.1.3.3 Carbons

Similar to the above muon and proton simulation, carbons with kinetic energy 18 GeV were vertically incident from the same launch point (x, y, z) = (201.17, 201.17, -48.12) mm. Figure G.9 shows the GLEAM result by simulating 10000 carbon events. The mean rate of energy loss in the first crystal is 210.69 MeV/cm, which agrees with that from the WW dEdx code within a 3.5% error.

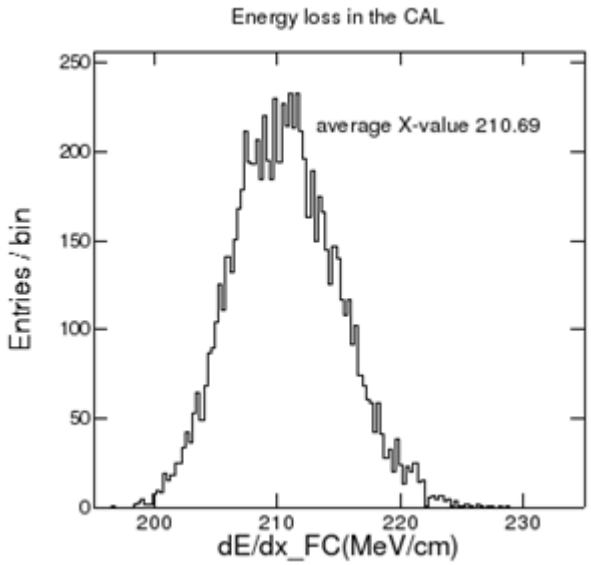

Figure G.9 The rate of energy loss of 18 GeV carbons in the first crystal simulated by GLEAM.

In summary, the energy losses of the 1 GeV muons, 6 GeV protons and 18 GeV carbons calculated by the WW dEdx code, GEANT4 and GLEAM were very consistent within < 4% error. Therefore, the energy loss in GEANT4 and GLEAM were correctly calculated.

G.2 CAL Calibration on the Ground

The energy calibration is used to convert measurements in "instrument units" such as ADC value into "physical units" such as MeV. The primary pre-flight CAL calibrations were performed using two sources: charge injection using a precision DAC and cosmic ray muons [83]. The charge injection calibration produced a DAC versus ADC table for each crystal in each range; by fitting this table using a cubic spline function, each ADC value could be converted to a DAC value. Then the gain ratio (or DAC ratio for the same ADC) between two ranges of the same diode could be derived. Using ground-level cosmic ray muons, we could measure the light asymmetry

for each crystal, and the pedestal position and noise distribution width for each crystal in each energy range. We could also calculate the gains (the coefficient converting ADC to MeV) for each crystal in the lowest energy range (LEX8) by dividing the geometric mean of the most probable energy deposition of vertical muons in a crystal by the peak value of the Landau fit. Then using the special setting "muon gain", we could derive the gain ratio between small and big diodes. Finally, the gain calibration of other energy ranges was done by using the gain ratios between ranges.

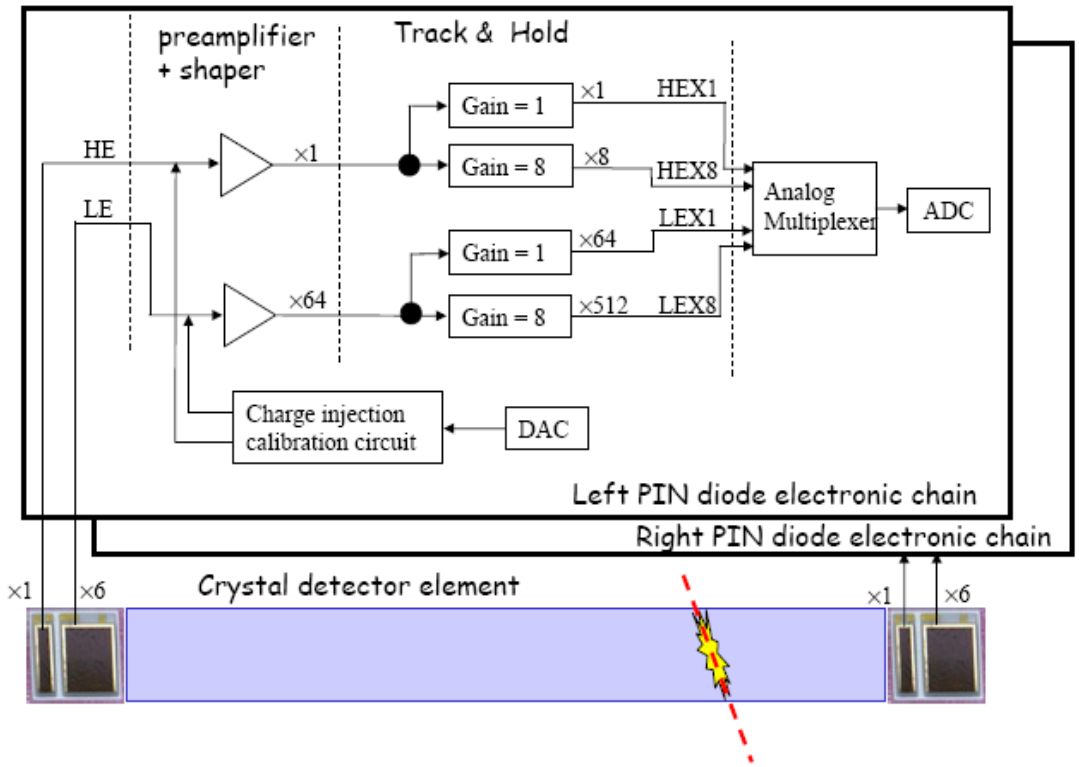

Figure G.10 Front-end electronics of one crystal of the CAL. The diodes on the end of each crystal are shown in black in the figure. See [83] for more details.

G.3 Cross-check of the CAL Calibration

G.3.1 Beam Test

A massive campaign of Beam Tests (BT) [89] was performed between July and November 2006 on the LAT Calibration Unit (CU) to validate the LAT functionality and the GLEAM simulation. This extensive test was used to validate the GLEAM simulation as GLEAM is used to reproduce the entire LAT response to particle radiation, the event reconstruction, and the background rejection strategy, both before launch and during on-orbit operation.

CU is a detector built with spare flight modules and flight-like readout electronics. It is composed of two complete LAT tower modules (TKR and CAL) and one additional CAL module, integrated in a 1x4 aluminum grid, and also an assembly of five flight-like ACD tiles. Figure G.11 shows a picture of the CU.

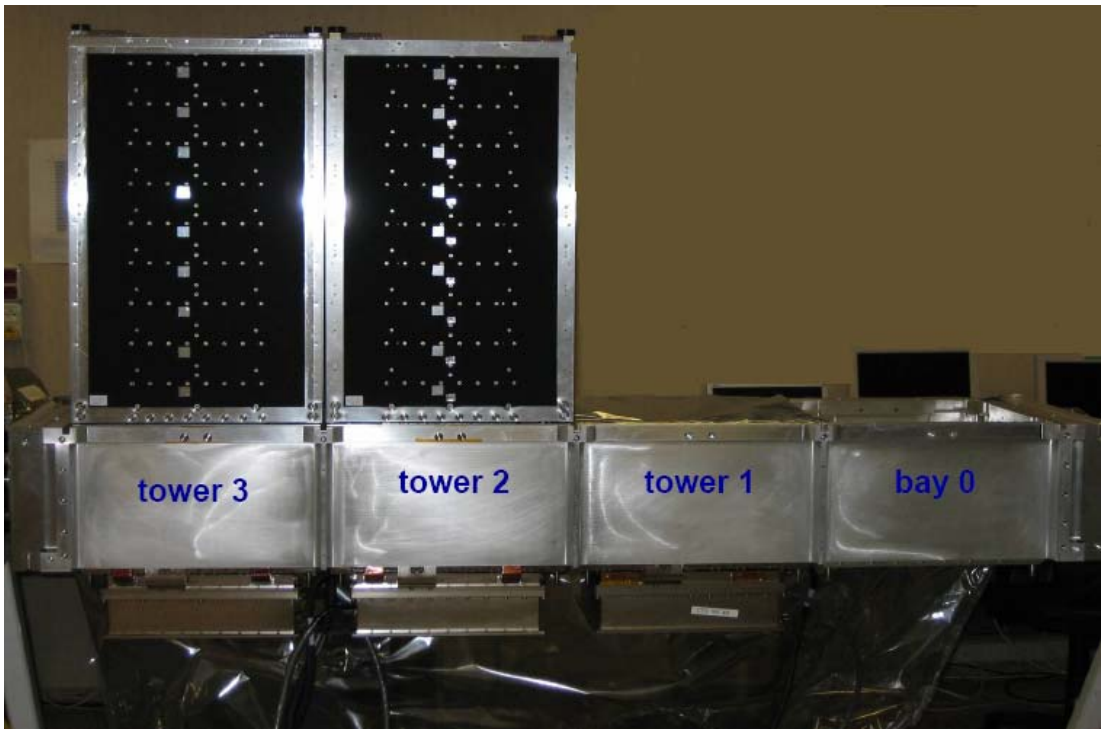

Figure G.11 A picture of part of the CU, including two complete LAT tower modules and one additional CAL module.

In order to test the CU with a whole spectrum of signals that would be detected by the LAT, three different experimental setups were used. At the CERN-PS, electrons, positrons, pions and protons were available in “cocktail” beams, covering the momentum range between 500 MeV/c and 10 GeV/c. At the CERN-SPS, where secondary beams electrons, positrons, pions and protons with momenta from 10 to 300 GeV/c were available, the performance of the CU at very high energy was studied. At GSI, the CU was exposed to heavy ion beams of carbon and xenon with energies of 1 and 1.5 GeV/nuleon, and impacting the detector at 0, 30 and 60 degrees.

G.3.2 Configuration of BT Electron Data 700001796

More than 300 different configurations were tested in the BT, changing the beam particle, energy and rate, the incoming angle and the interaction point of the beam, and several register settings of the instrument. Run 700001796 used the CERN-SPS electron beam with the momentum 99.0 GeV/c. The beam impact position was at (187.25, 13.92, 0.0) *mm*, and the beam angle was 0 degree, so the beam was normally incident into the middle of the center CsI log of Tower 2. Figure G.12 shows cartoons of the geometry viewing the CU from the side (left top) and from the top (left bottom and right). The trigger configuration of this run was set to 16, which meant the instrument had nominal flight settings, 4- range readout and zero suppression.

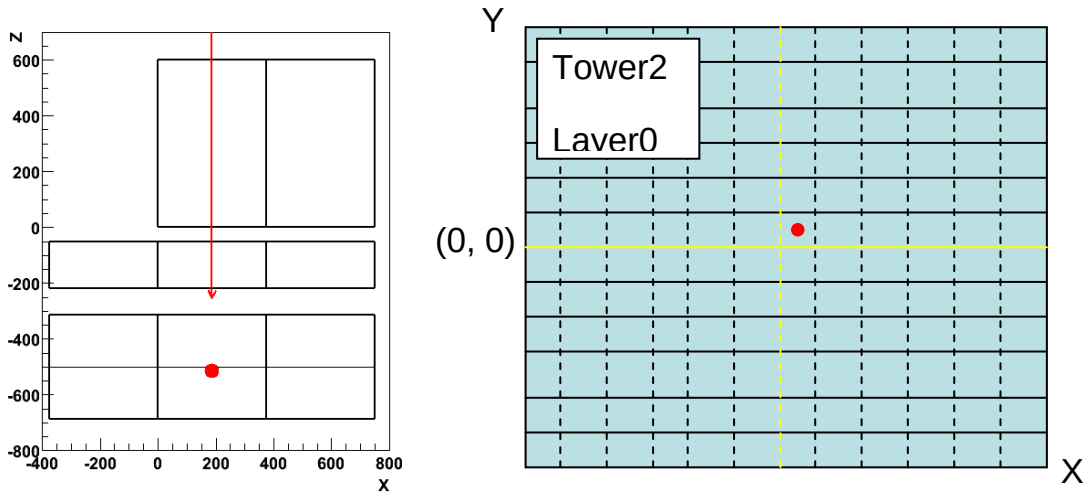

Figure G.12 Cartoon diagrams demonstrating the geometry viewing from the side (left top panel) and from the top (left bottom and right panel). The right panel is a zoom-in of the CAL top of Tower 2. The red line and points indicate the beam impact direction and position.

G.3.3 Electron Selection

In order to select clean electron events from BT data, we applied a set of analysis cuts developed by A. Moiseev, J. F. Ormes and S. Funk [90]. The basic approach was to utilize the difference between electron-initiated and hadron-initiated event patterns in LAT by the following selections:

- 10 GeV < CTBBestEnergy < 500 GeV

Remove events which passed the LAT without interaction or interacted too deep in the LAT CAL.

- CalTransRms*CalLongRms < 1300+0.00142*CTBBestEnergy

Remove events which have scattered hit CAL crystals at some distance from the shower axis, using the fact that a lepton-initiated shower in the CAL is much more compact (dense) than for most hadron-initiated events.

- AcdTotalEnergy < 30

Remove events with large energy deposition in ACD tiles, using the fact that hadron-initiated events have (on average) larger number of backward moving charged particles which create excessive hits in the ACD.

- CalRmsAsym < 0.05

Remove events with larger asymmetry of the shower shape in the CAL, since electron-initiated showers have much smaller shape fluctuation.

- Tkr1ToTTrAve > 2, Tkr1CoreHC > 10

Select events which interact in the TKR.

- CalTotRLn > 8

Select events with the path in the CAL to be longer than 8 radiation length to improve energy resolution.

G.3.4 Cross-check of the CAL Calibration

First, we verified the deviation from linearity in DAC versus ADC using charge injection data. For LEX8, the relative deviation was about 0.2% at 1000 ADC units, while for LEX1, it was about 3%. The relative deviation increased as ADC value became even smaller. This non-linearity was shown in Figure G.13, and was consistent with the previous work.

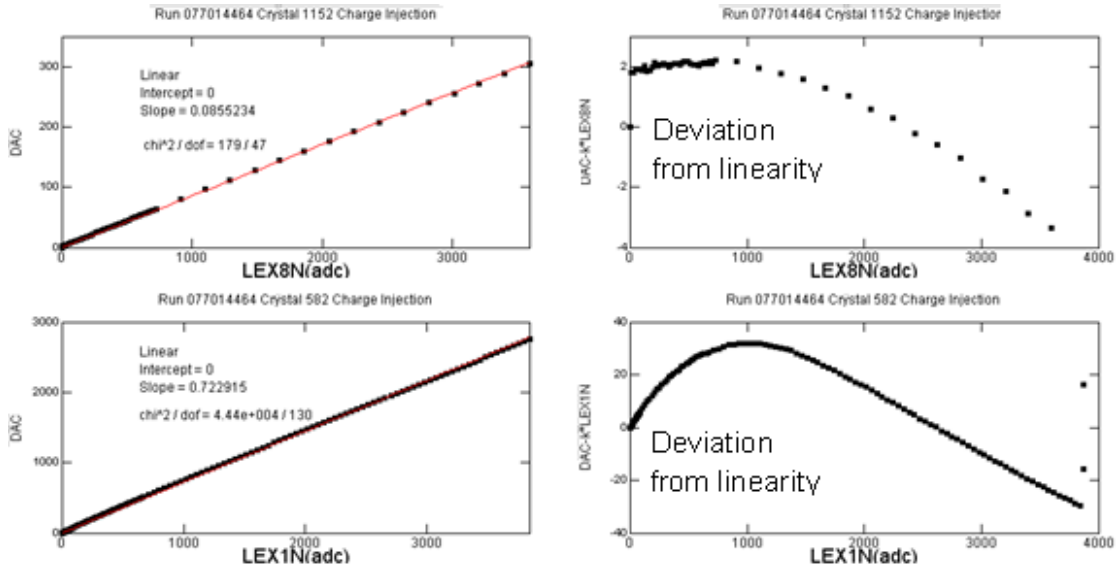

Figure G.13 Non-linearity between DAC and ADC for one typical crystal in LEX8 (top panel) and LEX1 (bottom panel) negative face for the charge injection run 077014464. The left panels are the linear fit (red line) to DAC versus ADC. The right panels are the absolute deviations from linearity in DAC versus ADC.

Second, we checked whether the cubic spline fitting function correctly converted ADC values to DAC values, since the non-linearity should be taken into consideration

by the fit. The DAC had a linear charge scale to high accuracy according to its requirements; therefore, DAC values should be the same for different ranges for one energy input, which was verified in Figure G.14 using beam test electron data. In Figure G.14, DAC values were perfectly linear for ranges of the same diode as shown in the left two panels; in contrast, by comparing the DAC values in big and small diodes as shown in the right panel, the majority had the correct linear relation, but a small fraction had huge deviations. Those huge deviations were not considered to be a result of an incorrect energy calibration because they only occurred for a small fraction of the total number of channels. However, this still needed to be investigated further; SLAC physics staff member Gary Godfrey gave the following explanation for the reason for this small number of large deviations. It was possible that at first the voltage held by the big diode saturated and then it attenuated; and based on the readout rule, that the readout algorithm read out the lowest energy range which was not saturated, the big diode was read out by mistake..

Third, we checked the absolute gain in LEX8, which was the most probable energy of vertical muons divided by the Landau peak. We defined the absolute gain using beam test proton data instead of ground muon data. However, the “antiquenching” effect for carbon still existed. Therefore, the “antiquenching” effect was not due to the definition of the absolute gain.

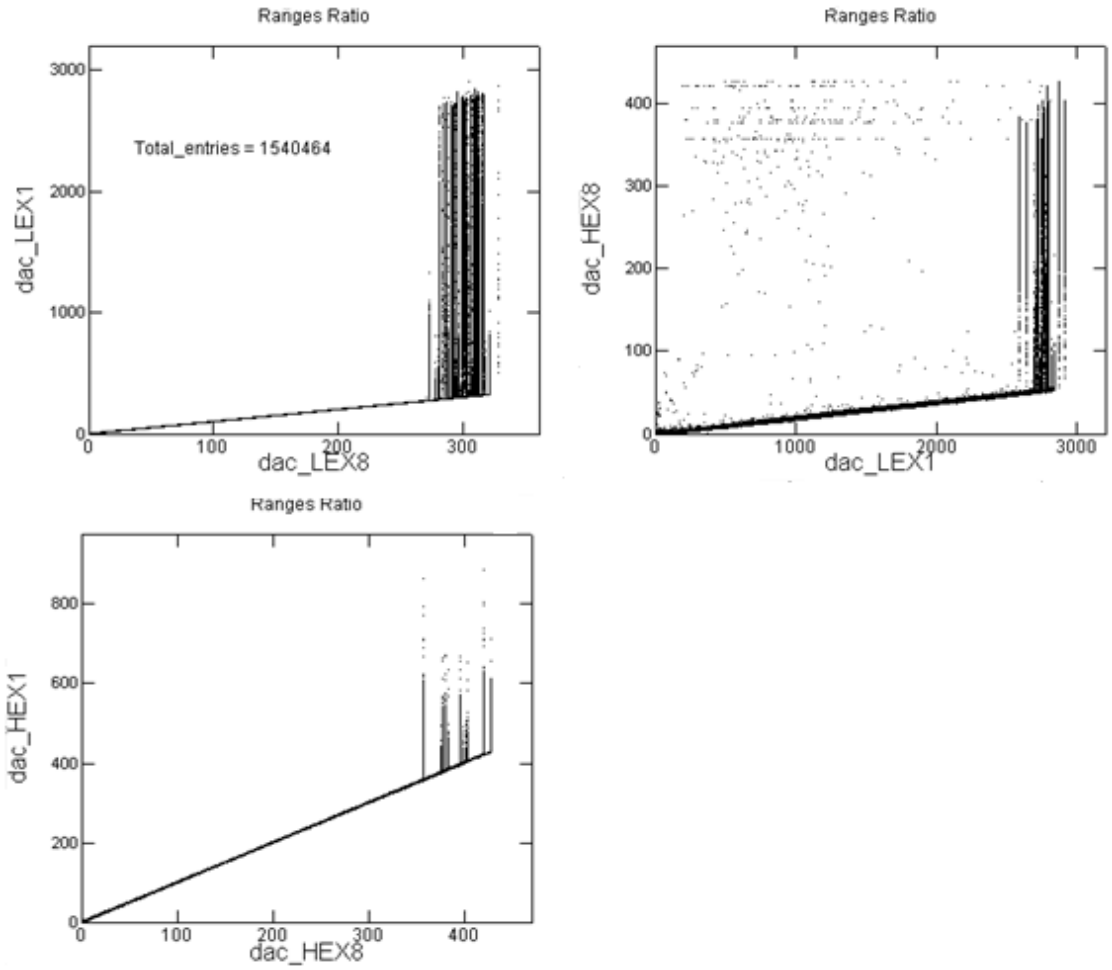

Figure G.14 DAC values are the same for different ranges for one energy input using the beam test 99 GeV/c electron Run 700001796. The vertical line patterns in each panel are due to the energy range saturation.

G.4 Conclusion

No miss-calibration was found in our many cross-checks, but we still don't understand the origin and mechanism of the "anti-quenching" effect for heavier nucleii. Originally, we intended to use cosmic ray heavy ions to calibrate the higher energy scales. However, due to the lack of a physical model or understanding for this "anti-quenching" behavior, we felt that the systematic uncertainties introduced in using the heavy ions were unacceptable for the on-orbit calibration and decided to use a

technique we refer to as “proton inter-range calibration” instead [91]. The heavy ions are only used on-orbit for checking the stability of the CAL gain with time, and do not provide the absolute energy calibration at higher energy that we hoped for.

BIBLIOGRAPHY

[1] F. Zwicky, Helv. Phys. Acta **6**, 124 (1933)

[2] F. Zwicky, ApJ **86**, 217 (1937)

[3] V. Rubin and K. Ford, ApJ **159**, 379 (1970)

[4] L. Strigari et al., ApJ **669**, 676 (2007)

[5] L. Strigari et al., Nature **454**, 1096 (2008)

[6] D. Clowe et al., ApJ **648**, 109 (2006)

[7] C. Bennett et al., ApJS **148**, 1 (2003)

[8] D. Spergel et al., ApJS **170**, 377 (2007)

[9] G. Hinshaw et al., ApJ **180**, 225 (2009)

[10] J. F. Navarro, C. S. Frenk and S. D. M. White, ApJ **490**, 493 (1997)

[11] B. Moore et al., Mon. Not. Roy. Astron. Soc. **310**, 1147 (1999)

[12] J. Taylor, A. Babul, Mon. Not. Roy. Astron. Soc. **348**, 811 (2004)

[13] J. Taylor, A. Babul, Mon. Not. Roy. Astron. Soc. **364**, 515 (2005)

[14] J. Taylor, A. Babul, Mon. Not. Roy. Astron. Soc. **364**, 535 (2005)

[15] J. Diemand et al., Nature **454**, 735 (2008)

[16] V. Springel et al., Mon. Not. Roy. Astron. Soc. **391**, 1685 (2008)

[17] B. Moore, S. Ghigna, F. Governato, ApJ **524**, 19 (1999)

[18] R. Peccei and H. R. Quinn, Phys. Rev. Lett. **40**, 223 (1978)

[19] L. J. Rosenberg, K. A. van Bibber, Phys. Rep. **325**, 1 (2000)

[20] L. D. Duffy et al., Phys. Rev. D **74**, 012006 (2006)

[21] The ADMX Collaborations, Phys. Rev. Lett. **104**, 041301 (2010)

[22] M. A.Sanchez-Conde et. al., Phys. Rev. D **79**, 123511 (2009)

[23] G. Bertone, D. Hooper and J. Silk, Phys. Rep. **405**, 279, (2005)

[24] E. A. Baltz et al., JCAP **07**, 013, 2008

[25] A. Cesarini et al., Astroparticle Phys. **21**, 267, 2004

[26] A. Birkedal et al., arXiv:hep-ph/0507194

[27] T. Bringmann, L. Bergstrom and J. Edsjo, JHEP **0801**, 049 (2008)

[28] A. Pullen, R. Chary and M. Kamionkowski, Phys. Rev. D **76**, 063006 (2007)

[29] The Fermi LAT Collaboration, Phys. Rev. Lett. **104**, 091302 (2010)

[30] G. Bertone, D. Hooper and J. Silk, Phys. Rept. **405**, 279 (2005)

[31] H. C. Cheng, J. L. Feng, K. T. Matchev, Phys. Rev. Lett. **89**, 211 (2002)

[32] G. Servant, T. M. Tait, Nucl. Phys. **B650**, 391 (2003)

[33] N. Arkani-Hamed, A. G. Cohen, H. Georgi, Phys. Lett. **B513**, 232 (2001)

[34] N. Arkani-Hamed et al., JHEP **0208**, 020 (2002)

[35] N. Arkani-Hamed et al., JHEP **0207**, 034 (2002)

[36] N. Arkani-Hamed et al., JHEP **0208**, 021 (2002)

[37] A. Birkedal-Hansen, J. G. Wacker, Phys. Rev. D **69**, 065022 (2004)

[38] H. C. Cheng, I. Low, JHEP **0309**, 51 (2003)

[39] J. N. Bahcall and R. M. Soneira, Astrophys. J. Suppl. **44**, 73 (1980)

[40] S. Profumo, K. Siguidson, M. Kamionkowski, Phys. Rev. Lett. **97**, 031301 (2006)

[41] B. S. Acharya et al., Phys. Rev. D **80**, 083529 (2009)

[42] T. Moroi, L. Randall, Nucl. Phys. B **570**, 455 (2000)

[43] M. Bradac et al., ApJ **687**, 959 (2008)

[44] C. Rodriguez-Gonzalvez et al., arXiv:1011.03254 (2010)

[45] M. Owers et al., ApJ **728**, 27 (2011)

[46] E. D. Bloom, C. W. Peck, Ann. Rev. Nucl. Part. Sci. **33**, 143 (1983)

[47] M. Dine, W. Fischler, M. Srednicki, Phys. Lett. B **104**, 199 (1981)

[48] J. Chang et al., Nature **456**, 362 (2008)

[49] O. Adriani et al., Nature **458**, 607 (2009)

[50] A. A. Abdo et al., Phys. Rev. Lett. **102**, 181101 (2009)

[51] J. L. Feng, A. Rajaraman, F. Takayama, Phys. Rev. D **68**, 63 (2003)

[52] G. Bertone et al., JCAP **0903**, 009 (2009)

[53] S. M. Faber, J. S. Gallagher, Annu. Rev. Astron. Astrophys. **17**, 135 (1979)

[54] W. B. Atwood et al., ApJ **697**, 1071 (2009)

[55] http://www-glast.slac.stanford.edu/software/IS/glast_lat_performance.htm

[56] R. Riccardo, arXiv:0907.0626 (2009)

[57] P. Gondolo et al., JCAP **0407**, 008 (2004)

[58] G. Kane, R. Lu, Phys. Lett. B 681, 151 (2009)

[59] D. Hooper, L. Goodenough, arXiv:1010.2752v3 (2010)

[60] http://fermi.gsfc.nasa.gov/ssc/data/access/lat/BackgroundModels.html

[61] A. W. Strong, I.V. Moskalenko, O. Reimer, ApJ **613**, 962 (2004)

[62] A. Abdo et al., ApJS **188**, 405, 2010

[63] M. Kuhlen, J. Diemand, P. Madau, ApJ, **686**, 262, 2008

[64] M. Kuhlen, P. Madau, J. Silk, Science, **325**, 970, 2009

[65] L. Pieri, J. Lavalle, G. Bertone and E. Branchini, arXiv:0908.0195

[66] H. Chernoff, Ann. Math. Statist. **25**, 573 (1954)

[67] http://fermi.gsfc.nasa.gov/ssc/data/analysis/documentation/

[68] P. Sreekumar et al., ApJ **494**, 523 (1998)

[69] http://fermi.gsfc.nasa.gov/ssc/data/analysis/LAT_caveats.html

[70] A. Abdo et al., ApJS **183**, 46 (2009)

[71] J. R. Mattox et al., ApJ **461**, 396 (1996)

[72] A. A. Abdo et al., ApJ **715**, 429 (2010)

[73] A. A. Abdo et al., ApJS **187**, 460 (2010)

[74] N. Fornengo, L. Pieri, S. Scopel, Phys. Rev. D **70**, 103529 (2004)

[75] P. Madau, J. Diemand, M. Kuhlen, ApJ **679**, 1260 (2008)

[76] V. Springel et al., Mon. Not. Roy. Astron. Soc. **391**, 1685 (2008)

[77] M. Kuhlen, J. Diemand, P. Madau, ApJ **686**, 262 (2008)

[78] T. Jeltema, S. Profumo, JCAP **11**, 003 (2008)

[79] Ph. Bruel, "Energy reconstruction at high energy with the LAT" (2005)

[80] Pol d'Avezac, "A Maximum-Likelihood Energy Reconstruction Method" (2006)

[81] http://sirad.pd.infn.it/glast/ground_sw/rForest/rforest.html

[82] http://www.stat.berkeley.edu/users/breiman/RandomForests/

[83] J. Ampe et al., IEEE Trans. Nucl. Sci. **51**, 5 (2004)

[84] B. Lott et al., Nucl. Instrum. Meth. Phys. Res. A **560**, 395 (2006)

[85] B. A. Weaver, A. J. Westphal, Nucl. Instrum. Meth. Phys. Res. B **187**, 285 (2002)

[86] N. V. Mokhov et al., Radiation Protection Dosimetry **116**, 104 (2005)

[87] http://www.geant4.org/geant4/

[88] P. Boinee et al., arXiv:astro-ph/0308120v4 (2003)

[89] L. Baldini et al., The First GLAST Symposium, AIP Conf. Proceedings **921**, 190 (2007)

[90] A. Moiseev, J. F. Ormes, S. Funk, The First GLAST Symposium, AIP Conf. Proceedings **921**, 500 (2007)

[91] A. A. Abdo et al., Astropart. Phys. **32**, 193 (2009)

[92] A. Kravtsov, Advances in Astronomy **2010**, 281913 (2010)